HgTe based topological insulators

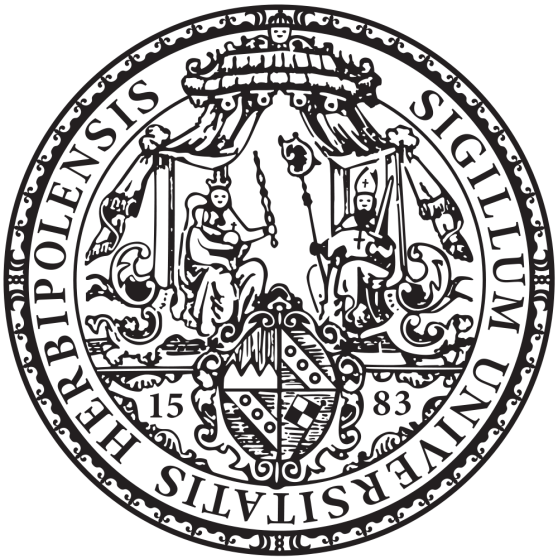

Dissertation zur Erlangung des naturwissenschaftlichen Doktorgrades der Julius-Maximilians-Universität Würzburg

vorgelegt von Christoph Brüne

geboren in Arolsen

Würzburg, 2014

Eingereicht am: .....
bei der Fakultät für Physik und Astronomie

1. Gutachter: .....
2. Gutachter: .....
3. Gutachter: .....
der Dissertation

Vorsitzende(r): .....

1. Prüfer: .....
2. Prüfer: .....
3. Prüfer: .....
im Promotionskolloqium

Tag des Promotionskolloqiums: .....

Promotionsurkunde ausgehändigt am: .....

Abstract

Recently a new state of matter was discovered in which the bulk insulating state in a material is accompanied by conducting surface or edge states. This new state of matter can be distinguished from a conventional insulator phase by the topological properties of its band structure which led to the name "topological insulators". Experimentally, topological insulator states are mostly found in systems characterized by a band inversion compared to conventional systems. In most topological insulator systems, this is caused by a combination of energetically close bands and spin orbit coupling. Such properties are found in systems with heavy elements like Hg and Bi. And indeed, the first experimental discovery of a topological insulator succeeded in HgTe quantum wells and later also in BiSb bulk systems.

Topological insulators are of large interest due to their unique properties: In 2-dimensional topological insulators one dimensional edge states form without the need of an external magnetic field (in contrast to the quantum Hall effect). These edge states feature a linear band dispersion, a so called Dirac dispersion. The quantum spin Hall states are helical edge states, which means they consist of counterpropagating oppositely spin polarized edge channels. They are therefore of great potential for spintronic applications as well as building blocks for new more exotic states like Majorana Fermions. 3-dimensional topological insulators feature 2-dimensional surface states with only one Dirac band (also called Dirac cone) on each surface and an interesting spin texture where spin and momentum are locked perpendicular to each other in the surface plane. This unique surface band structure is predicted to be able to host several exotic states like e.g. Majorana Fermions (in combination with superconductors) and magnetic monopole like excitations.

This PhD thesis will summarize the discovery of topological insulators and highlights the developments on their experimental observations. The work focuses on HgTe which is up to now the only topological insulator material where the expected properties are un-

ambiguously demonstrated in transport experiments. In HgTe, the topological insulator properties arise from the inversion of the Γ_6 and Γ_8 bands. The band inversion in HgTe is due to a combination of a high spin orbit splitting in Te and large energy corrections (due to the mass-velocity term) to the energy levels in Hg. Bulk HgTe, however, is a semimetal, which means for the conversion into a topological insulator a band gap has to be opened. In two dimensions (HgTe quantum well structures) this is achieved via quantum confinement, which opens a band gap between the quantum well subbands. In three dimensions, strain is used to lift the degeneracy of the semimetallic Γ_8 bands opening up a band gap.
The thesis is structured as follows:

- The first chapter of this thesis will give a brief overview on discoveries in the field of topological insulators. It focuses on works relevant to experimental results presented in the following chapters. This includes a short outline of the early predictions and a summary of important results concerning 2-dimensional topological insulators while the final section discusses observations concerning 3-dimensional topological insulators.

- The discovery of the quantum spin Hall effect in HgTe marked the first experimental observation of a topological insulator. Chapter 2 will focus on HgTe quantum wells and the quantum spin Hall effect.
  Above a critical thickness, HgTe quantum wells are predicted to host the quantum spin Hall state, the signature of a 2-dimensional topological insulator. HgTe quantum wells exhibiting low carrier concentrations and at the same time high carrier mobilities are required to be able to measure the quantum spin Hall effect. The growth of such high quality HgTe quantum wells was one of the major goals for this work. Continuous optimization of the substrate preparation and growth conditions resulted in controlled carrier densities down to a few $10^{10}\,\mathrm{cm}^{-2}$. At the same time, carrier mobilities exceeding $1 \times 10^6\,\mathrm{cm}^2\,\mathrm{V}^{-1}\,\mathrm{s}^{-1}$ have been achieved, which provides mean free paths of several micrometers in the material. Thus the first experimental evidence for the existence of the quantum spin Hall edge states succeeded in transport experiments on microstructures: When the Fermi energy was located in the bulk band gap a residual quantized resistance of $2e^2/h$ was found. Further experiments focused on investigating the nature of transport in this regime. By non-local measurements the edge state character could be established. The measured non-local resistances corresponded well with predictions from the Landauer-

Büttiker theory applied to transport in helical edge channels.
In a final set of experiments the spin polarization of the edge channels was investigated. Here, we could make use of the advantage that HgTe quantum well structures exhibit a large Rashba spin orbit splitting. In systems with a large Rashba spin orbit splitting a spin accumulation is expected to occur at the edge of the sample perpendicular to a current flow. This so-called spin Hall effect was then used as a spin injector and detector. Using split gate devices it was possible to bring spin Hall and quantum spin Hall state into direct contact, which enabled an all electrical detection of the spin polarization of the quantum spin Hall edge channels.

- HgTe as a 3-dimensional topological insulator will be presented in chapter 3. Straining the HgTe layer enables the observation of topological insulator behavior. It was found that strain can be easily implemented during growth by using CdTe substrates. CdTe has a slightly larger lattice constant than HgTe and therefore leads to tensile strain in the HgTe layer as long as the growth is pseudomorphic. Magnetotransport studies showed the emergence of quantum Hall transport with characteristic signatures of a Dirac type bandstructure. Thus, this result marks the first observation of the quantum Hall effect in the surface states of a 3-dimensional topological insulator.
  Transport experiments on samples fitted with a top gate enabled the identification of contributions from individual surfaces. Furthermore, the surface state quantum Hall effect was found to be surprisingly stable, perturbations due to additional bulk transport could not be found, even at high carrier densities of the system.

- Chapters 4 - 6 serve as in depth overviews of selected works: Chapter 4 presents a detailed overview on the all electrical detection of the spin Hall effect in HgTe quantum wells. The detection of the spin polarization of the quantum spin Hall effect is shown in chapter 5 and chapter 6 gives a detailed overview on the quantum Hall effect originating from the topological surface state in strained bulk HgTe.

The investigations discussed in this thesis pioneered the experimental work on the transport properties of topological insulator systems. The understanding of the fundamental properties of topological insulators enables new experiments in which e.g. the inclusion of magnetic dopants or the interplay between topological insulator and superconductors can be investigated in detail.

Zusammenfassung

Vor kurzem wurde entdeckt, dass Festkörper einen bisher unbekannten Zustand einnehmen können in welchem das Innere des Körpers isolierend ist während Oberflächen bzw. Ränder leitend bleiben. Materialien, die diese Eigenschaften aufweisen, werden "topologische Isolatoren" genannt, da ihre besonderen Eigenschaften auf eine gegenüber von konventionellen Materialien veränderten Topologie zurückgeführt werden kann. Die große Mehrheit an Materialien, in denen topologische Isolatorzustände gefunden wurden, zeichnen sich durch eine veränderte Abfolge der Energiebänder, im Vergleich mit gewöhnlichen Isolatoren, aus. Diese veränderte Anordnung der Bänder resultiert in den meisten Fällen aus einem Zusammenwirken von energetisch nahe zusammenliegenden Bändern und Spin-Bahn Wechselwirkung. Aus diesem Grund wurden Topologische Isolatoren bisher vor allem in Materialien gefunden, die schwere Elementen wie Hg und Bi enthalten: Erstmals experimentell nachgewiesen wurde die Existenz von topologischen Isolatoren an HgTe Quantentrögen und später auch in BiSb Volumensystemen.

Topologische Isolatoren sind aufgrund ihrer besonderen Eigenschaften von großem Interesse: 2-dimensionale topologische Isolatoren sind durch das Auftreten eindimensionaler Randzustände gekennzeichnet, ohne dass hierfür ein Magnetfeld nötig wäre (im Gegensatz zum Quanten-Hall-Effekt). Diese sogenannten helikalen Randzustände sind gegenläufige und entgegengesetzt spin-polarisierte Randzustände, wodurch sie besonders für spintronische Anwendungen interessant sind. Des Weiteren sind sie auch potenzielle Bausteine zur Verwirklichung weiterer exotischer Zustände wie zum Beispiel Majorana Fermionen. 3-dimensionale topologische Isolatoren zeichnen sich durch das Auftreten von 2-dimensionalen Oberflächenzuständen aus. Diese Oberflächenzustände haben eine Dirac-Bandstruktur mit einer besonderen Spin-Textur in der Spin und Impuls rechtwinklig zueinander stehen (beide in der Oberfächenebene). Diese besondere Bandstruktur sollte es ermöglichen in diesen Materialen exotische Zustände zu entdecken wie zum Beispiel Majorana Fermionen (im Zusammenspiel mit Supraleitern) oder Anregungen,

die magnetischen Monopolen gleichen.

Diese Doktorarbeit wird die Entdeckung topologischer Isolatoren sowie Entwicklungen die im Bereich der experimentellen Untersuchung stattfanden vorstellen. Im Besonderen wird sich diese Arbeit auf das Materialsystem HgTe konzentrieren, dem einzigen Materialsystem in dem es bisher gelungen ist topologische Isolatoreigenschaften eindeutig in Transportstudien nachzuweisen. Die topologischen Isolatoreigenschaften von HgTe entstehen durch die Inversion der Γ_6 und Γ_8 Bänder. Diese Inversion wird durch die starke Spin-Bahn-Wechselwirkung in Te und durch die großen relativistischen Korrekturen der Energiepositionen der Bänder in Hg erzeugt. Da HgTe im Volumenmaterial allerdings semimetallisch ist, muss zur Beobachtung von topologischen Isolatoreigenschaften eine Bandlücke geöffnet werden. Im 2-dimensionalen Zustand (HgTe Quantentröge) geschieht dies durch das quantenmechanische Confinement, wodurch eine Bandlücke zwischen den Subbändern des Quantentrogs geöffnet wird. In 3-dimensionalen topologischen Isolatoren kann eine Bandlücke durch das Verspannen der HgTe Schicht gebildet werden, da in diesem Fall die Entartung der Γ_8 Bänder aufgehoben wird.
Diese Doktorarbeit ist wie folgt gegliedert:

- Im ersten Kapitel wird eine kurze Übersicht über Entdeckungen und Entwicklungen im Bereich topologischer Isolatoren gegeben mit besonderem Fokus auf Arbeiten mit Relevanz zu den in den weiteren Kapiteln vorgestellten Ergebnissen. Die Übersicht beginnt mit einem kurzen Überblick über die ersten Voraussagen, die zur Entdeckung von topologischen Isolatoren und zum Verständnis dieses neuen Zustandes geführt haben. Im Weiteren wird eine kurze Übersicht über wichtige Ergebnisse im Bereich der 2- und 3-dimensionalen topologischen Isolatoren gegeben.

- Die Entdeckung des Quanten-Spin-Hall-Effekts in HgTe markiert auch gleichzeitig den ersten experimentellen Nachweis der Existenz topologischer Isolatoren. Kapitel 2 wird daher Eigenschaften von HgTe Quantentrögen und den Quanten-Spin-Hall-Effekt behandeln.

  Die Existenz des Quanten-Spin-Hall-Effekts, das charakteristische Merkmal 2-dimensionaler topologischer Isolatoren, wurde für HgTe Quantentröge oberhalb einer kritischen Dicke vorausgesagt. Der experimentelle Nachweis dieses Effekts setzt voraus, dass die zu vermessenden Quantentröge über eine möglichst geringe Ladungsträgerdichte und gleichzeitig hohe Ladungsträgerbeweglichkeit verfügen. Das Wachstum von Quantentrögen mit diesen Eigenschaften war eine der Hauptaufgaben, die im Rahmen dieser Arbeit durchgeführt wurden. Durch diese Anstren-

gungen ist es mittlerweile möglich Quantentröge mit intrinsischen Ladungsträgerdichten weit unterhalb von $1 \times 10^{11}\,\mathrm{cm}^{-2}$ bis in den mittleren $10^{12}\,\mathrm{cm}^{-2}$ Bereich herzustellen, während die Ladungsträgerbeweglichkeiten $1 \times 10^{6}\,\mathrm{cm}^{2}\,\mathrm{V}^{-1}\,\mathrm{s}^{-1}$ überschreiten können. Dies ermöglicht ballistischen Transport über mehrere Mikrometer in solchen Proben.
Es wurden Transportexperimente an solch hoch qualitativen Quantentrögen durchgeführt um den Quanten-Spin-Hall-Effekt experimentell nachweisen zu können. Dies führte zur Entdeckung erster experimenteller Beweise für die Existenz des Effekts bei Transportuntersuchungen an Mikrostrukturen. Befand sich das Fermi-Level in diesen Strukturen innerhalb der Energielücke zwischen Leitungs- und Valenzband wurde eine endliche Leitfähigkeit von circa $2e^2/h$ gemessen. Dies entspricht dem erwarteten Wert für elektrischen Transport in einem System mit zwei Randkanälen. In einer nachfolgenden Serie von Experimenten wurde nachgewiesen, dass der elektrische Transport in der Tat durch Randkanäle stattfindet. Zu diesem Zweck wurden nicht-lokale Transportmessungen durchgeführt, in denen erfolgreich untersucht wurde, ob die Resultate für Transport in verschiedenen nicht-lokalen Probengeometrien mit den Ergebnissen übereinstimmen, die im Rahmen des Landauer-Büttiker Formalismus, angewandt auf helikale Randzustände, erwartet werden. Im Weiteren wurde auch die Spinpolarisierung der Randzustände untersucht. Ermöglicht wurde dies durch die Nutzung des Spin-Hall-Effekts, mit dessen Hilfe Spininjektion und Spindetektion in die Randkanäle möglich ist. Der Spin-Hall-Effekt beschreibt das Auftreten von Spinströmen in Systemen mit starker Spin-Bahn-Kopplung, die sich senkrecht zum elektrischen Strom ausbreiten. In HgTe Quantentrögen konnte dieser Effekt durch ein rein elektrisches Experiment für Transport im metallischen Bereich nachgewiesen werden. Im Weiteren wurde dieser Effekt dann in weiteren nicht-lokalen Experimenten genutzt um die Spinpolarisierung der Randkanäle nachzuweisen.

- Kapitel 3 stellt die 3-dimensionalen topologischen Isolatoreigenschaften von HgTe vor. Wie bereits erwähnt ermöglicht die Nutzung von verspannten HgTe Schichten die Beobachtung von 3-dimensionalen topologischen Isolatorverhalten in HgTe Volumenmaterial. Wie sich im Rahmen dieser Arbeit herausstellte, kann Verspannung in diesen Schichten sehr einfach durch das pseudomorphe Wachstum auf gitter-fehlangepassten CdTe Substraten realisiert werden. CdTe hat eine größere Gitterkonstante als HgTe und erzeugt daher tensile Verspannung in den gewachsenen HgTe Schichten. In den so erhaltenen Schichten wurde bei Magnetotrans-

portmessungen der Quanten-Hall-Effekt beobachtet. Des Weiteren zeigte sich, dass der Quanten-Hall-Effekt in diesen Schichten charakteristische Merkmale für Dirac-Bandstrukturen aufweist. Dies bedeutet, dass auf diese Weise zum ersten Mal der Quanten-Hall-Effekt in den Oberflächenzuständen eines 3-dimensionalen topologischen Isolators detektiert werden konnte.
In weiteren Transportexperimenten wurde der Einfluss einer über der Struktur angebrachten Gateelektrode untersucht. Hierdurch wurde die Identifizierung von Beiträgen der einzelnen Oberflächen zum Transport möglich. Zudem stellte sich heraus, dass der Oberflächen-Quanten-Hall-Effekt sehr stabil ist und keine Anzeichen von einsetzendem Volumentransport sichtbar sind, selbst bei sehr hohen Gesamtladungsträgerdichten der Proben.

- In den Kapiteln 4 - 6 werden einige ausgewählte Arbeiten detailiert dargestellt: Kapitel 4 behandelt die rein-elektronische Detektion des Spin-Hall-Effekts in HgTe Quantentrögen genauer, während Kapitel 5 die Messung der Spinpolarization der Quanten-Spin-Hall-Kanäle detailiert vorstellt. In Kapitel 6 wird der Quanten-Hall-Effekt in den topologischen Oberflächenzuständen von verspanntem bulk HgTe beleuchtet.

Die in dieser Arbeit vorgestellten Untersuchungen waren Wegbereiter im Bereich der experimentellen Arbeiten, die sich mit den Transporteigenschaften topologischer Isolatoren beschäftigen. Das hierdurch gewonnene Verständnis für die fundamentalen Eigenschaften von topologischen Isolatoren ermöglicht viele weiterführende Experimente, zum Beispiel durch die Untersuchung des Einflusses von magnetischer Dotierung in topologischen Isolatoren oder deren Zusammenspiel mit Supraleitern.

Contents

Chapter 1

Introduction to the field of topological insulators

This chapter is an overview and introduction to the field of topological insulators and summarizes the basic findings concerning 2- and 3-dimensional topological insulators.

With the discovery of the quantum Hall effect in 1980 [1] and the subsequent efforts to explain the occurrence of the quantized Hall plateaus in 2-dimensional systems, the concept of topological order was first used to describe a physical system. It was found that the quantized Hall conductivity in units of e^2/h can be explained in terms of a topological invariant [2, 3]. After the discovery of the fractional quantum Hall effect [4] topology also became important in its theoretical description [5].

In 2005 Kane and Mele proposed a new topological insulator state in two dimensional systems, the so called Quantum Spin Hall system [6]. This proposal was based on calculations of the graphene bandstructure. The quantum spin Hall state was proposed to consist of two counterpropagating edge states with opposite spin polarization and in contrast to the quantum Hall state no magnetic field is needed to create these edge states. Unfortunately, the energy scales on which this effect should be observable in graphene are so small, that an experimental observation is impossible with today's experimental capabilities. However, shortly after that the group of Shoucheng Zhang proposed that the quantum spin Hall effect should also exist in inverted HgTe quantum wells [7]. During the early stages of this PhD work in 2007, the first observations of quantum spin Hall properties in HgTe quantum wells were made and reported in König *et al.*. [8].

The generalization and extension of the topological insulator concept to 3-dimensional systems was first given in proposals by Fu *et al.* [9], Moore and Balents [10] and as well by Roy [11]. The first experimental observations followed in 2008 by Dsieh *et al.*. [12] in the $Bi_{1-x}Sb_x$ system. This finding was followed by the prediction [13] and discovery of the Bi_2Se_3 [14] and Bi_2Te_3 [15] based materials as 3-dimensional topological insulators with relatively large band gaps and single Dirac cones on their surface.

1.1 2-dimensional topological insulators

In 2005 Kane and Mele predicted the existence of a new state of matter which is protected by topology, the Quantum-Spin-Hall insulator state [6]. In this publication they analyzed the impact of spin orbit coupling on the band structure of graphene in the vicinity of the Dirac point (graphene is a 2-dimensional system consisting of a single sheet of carbon atoms in a hexagonal lattice - for reviews on graphene and its band structure see e.g. [16] and [17]). The introduction of a specific spin orbit interaction term leads to a gap opening in the otherwise gapless Dirac band structure of graphene. This gaped state is however quite different from ordinary insulating band gaps in semiconductors. The introduced spin orbit parameter "produces gaps with opposite signs at [the] K and K'" [6] symmetry points in the Brillouin zone of graphene. In other words, the band ordering is inverted at the K point with respect to the K' point, furthermore the inversion is different for opposite spins. This inversion gives rise to the emergence of edge states with opposite directions of movement for opposite spins, the so called quantum spin Hall edge states. Even though these states are not chiral (one-directional) like in the quantum Hall effect, the spin polarization protects these states against elastic backscattering. In a more theoretical language the counterpropagating spin-polarized edge channels form a so called Kramers doublet that is protected by time reversal symmetry. This means that the edge states remain protected against backscattering as long as time-reversal symmetry is preserved. If however this symmetry is broken e.g. by a magnetic field, backscattering becomes possible and a gap opens in the quantum spin Hall states. Figure 1.1 shows the quantum spin Hall states emerging in the gap of the graphene band structure calculated for a strip geometry by Kane and Mele [6]. As Kane and Mele also realized, this quantum spin Hall-phase is distinct from ordinary insulating phases by its different topological order. In a similar way as the quantum Hall and fractional quantum Hall states have a different topology from usual insulators [18]. In a follow up work, Kane and Mele [19]

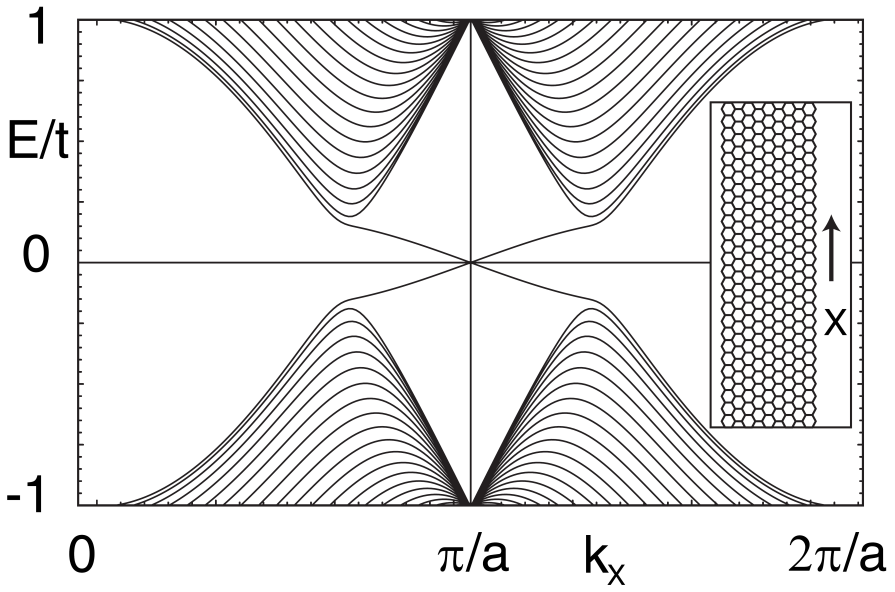

Figure 1.1: Low energy band structure of graphene with the spin orbit term introduced by Kane and Mele. [6]

also introduced a new topological invariant $\mathbf{Z}_2$ similar to the TKNN invariant [3] used for the description of the quantum Hall effect. The explanation of the quantum spin Hall effect through topological properties later on gave rise to the use of the name topological insulator for materials with those properties.

The quantum spin Hall state is of great interest due to its unique properties. The quantum spin Hall edge states are 1-dimensional channels and following from this their conductance is quantized. Therefore, the quantum spin Hall effect enables the realization of edge channel transport without a magnetic field and since these edge channels are additionally spin-polarized, they could be utilized for spintronic applications, like spin-injection and -detection.

It turned out however, that an experimental observation of pure edge channel transport in graphene would be very difficult due to the small size of the predicted bulk band gap. The band gap was estimated to be in the order of 10^{-3} meV [20, 21] and therefore the effect would only be observable at extremely low temperatures (mK temperatures or lower) and near perfect samples (potential fluctuations in the low μeV region). These prerequisites are not met neither in today's experiments nor samples, which prevents the experimental observation of the quantum spin Hall effect in graphene.

Shortly after Kane and Mele's work [6, 19] the group of Shou-Cheng Zhang (Stanford

University) predicted the quantum spin Hall state for other systems [22, 23], including HgTe quantum wells as a possible candidate [7]. It was found that HgTe quantum wells above a critical thickness host a topologically non-trivial state, which should give rise to the quantum spin Hall effect. Figure 1.2 A) shows the calculated energy of the E1 (blue) and H1 (red) states in HgTe quantum wells depending on quantum well thickness. For thicknesses below 6.5 nm the E1 band is the conduction band and the H1 band the valence band while the positions are reversed above this thickness. This inversion of the energy bands also implies a change of the band topology in the system. Figure 1.2 B) shows the band dispersion and the predominant band character at selected quantum well thicknesses. From the left to the right, dispersions for a quantum well thickness of 4.0 nm, 6.5 nm and 7.0 nm are shown, respectively. A dominant E1 character is indicated by blue regions while the H1 character is shown in red. In thin quantum wells below the critical thickness one can observe a homogenously E1 dominated conduction band and a H1 dominated valence band. At the critical thickness of 6.5 nm the band gap vanishes, resulting in a Dirac dispersion where the bands are equally mixed at the Dirac point. However, quantum wells above the critical thickness exhibit a predominantly E1-like character for the valence band states and H1 like character for the conduction band states close to the gap while the character changes back to a dominantly E1 character for higher k. This is a direct result from the non-trivial topology in the system [7]. These unusual band disperisons originate from

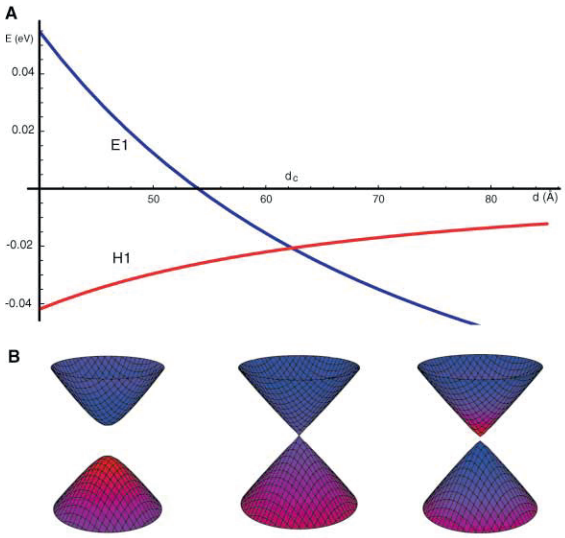

Figure 1.2: A) E1 (blue) and H1 (red) energy depending on the HgTe quantum well thickness. B) Schematic energy dispersion for quantum well thicknesses of 4.0 nm, 6.5 nm and 7.0 nm (from left to right). The colors indicate the predominant state of the system, blue sections have a dominant E1 character while red sections stand for a predominantly H1 character. [7]

the unusual bandstructure of HgTe which will be described in more detail in chapter 2. The size of the band gap in the topologically non-trivial quantum well structures can be up to 40 meV [24], thus enabling an experimental observation. The first experimental observation concerning the quantum spin Hall effect in HgTe quantum wells was made in the early stage of this PhD thesis [8]. This was followed by the experimental verification of 1-dimensional and non-local transport [25] in the quantum spin Hall regime and recently the discovery of experimental evidence for the spin polarization of the quantum spin Hall edge states [26]. A more detailed overview on these experimental findings will be reported in chapter 2.

1.2 3-dimensional topological insulators

The prediction of a new topologically protected state in 2-dimensional systems was followed by a generalization of this concept to 3-dimensions. Publications by Fu, Kane and Mele [9], Moore and Balents [10] and Roy [11] established the concept of 3-dimensional topological insulators. Fu *et al.* focused mainly on the bandstructure properties in these 3D TIs including the unique properties of the resulting surface states. Moore and Balents as well as Roy on the other hand explored the role of the $\mathbf{Z}_2$ topological invariants in 3-dimensional systems in general.

Moore and Balents found that in 3-dimensional systems 4 different topological $\mathbf{Z}_2$ invariants can be defined. Fu *et al.* investigated possible topological phases which are connected to these invariants. They categorized the different non-trivial topological insulator phases as weak or strong topological insulators, depending on their robustness against disorder. The strong TIs were found to host surface states that Fu *et al.* characterized as "a two-dimensional topological metal"[9]. These surface states are proposed to have very unique physical properties related to their topological origin. The surface state in a strong TI consists of an odd number of Dirac cones. In the simplest case this means the band structure of the surface state can be characterized as a 2-dimensional state with the band dispersion of a single Dirac cone. This implies, that these surface states are not spin degenerate, in contrast to for example graphene with 4 degenerate Dirac cones (2 spin degenerate and 2 valley degenerate cones [27, 28]) or a zero gap HgTe quantum well, which exhibits 2 Dirac cones [29]. However, since the surface state extends along the entire surface of the 3-dimensional topological insulator, surfaces with an opposite surface vector host Dirac cones with opposite spin polarization. In a single Dirac cone the quantum Hall effect

would be quantized in half integers of e^2/h [27, 9]:

$$\sigma_{xy} = \left(n + \frac{1}{2}\right)\frac{e^2}{h}. \tag{1.1}$$

Experimentally, a direct observation of this half integer Hall quantization is however unlikely to be realized since a measurement will probe all surfaces at once, due to the fact that they are metallically connected. Another property of the 3D TI surface states is their distinct spin texture. Spin and momentum **k** both lie in the surface plane but are always perpendicular to each other and states at momentum **k** and -**k** must have opposite spins, which means, that the spin rotates with **k** around the Fermi surface. A schematic sketch of the band dispersion of a 3D TI surface state is shown in picture 1.3, also indicated is the typical spin texture of a 3D TI surface state (yellow arrows). This spin texture also

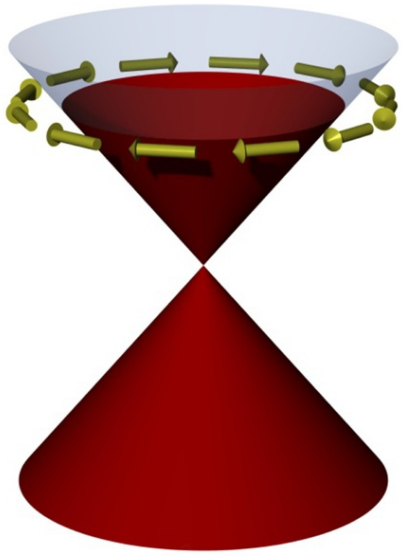

Figure 1.3: Schematic sketch of the single Dirac cone surface state of a 3-dimensional topological insulator. [30]

has implications for the robustness of the surface states against disorder. It was shown by Nomura *et al.* [31] that electrons in the surface state cannot be localized as long as time reversal symmetry is not broken. This can be understood by the fact that backscattering by 180° degrees is not possible as long as time reversal symmetry is preserved, otherwise a spin flip would be required. Shortly after the first general proposal by Fu *et al.* [32] a more detailed publication appeared, introducing the first proposals for material systems hosting 3D TI surface states [32], which included $Bi_{1-x}Sb_x$, α-Sn and strained HgTe as

examples of strong 3D TIs.

The first experiment, which showed evidence for a 3D topological insulator state was reported by Hsieh *et al.* in 2008 [12]. In this publication the bandstructure on the surface of $Bi_{1-x}Sb_x$ was investigated by angle-resolved photoemission spectroscopy (ARPES). Pure Bi and pure Sb are both semimetallic materials with a finite direct band gap, i.e. electron and hole pockets are occupied simultaneously. The big difference between these two materials is the bandordering at the L-point. In Sb the conduction band symmetry is L_a and the valence band has a L_s symmetry while in Bi this band ordering is inverted. Therefore, combining these materials allows for the engineering of the topology in this system. Band structure calculations predict a semiconducting state with a non-trivial topology for $Bi_{1-x}Sb_x$ alloys with Sb contents between $0.07 < x < 0.22$ [32, 18]. In the ARPES scans of $Bi_{0.9}Sb_{0.1}$ Hsieh *et al.* found a set of surface states in this material that cross the Fermi energy 5 times. This odd number of crossings indicates that these states are indeed topologically protected states.

Another group of topological insulators was proposed by the Zhang group in 2008 [13]. They proposed that the materials Bi_2Se_3, Bi_2Te_3 and Bi_2Sb_3 are 3-dimensional topological insulators with comparably large band gaps and single Dirac cone surface states. Figure 1.4 shows the calculated bandstructures of these materials [13]. The calculations are done by *ab initio* density functional theory. The non-trivial topological surface states are clearly visible for Sb_2Te_3, Bi_2Se_3 and Bi_2Te_3 in panel b to d. The calculated bulk band gaps range from $\approx$ 100 meV in the case of Bi_2Te_3 to $\approx$ 300 meV for Bi_2Se_3.

ARPES experiments on Bi_2Se_3 by Xia *et al.* [14] and on Bi_2Te_3 by Chen *et al.* [15] confirmed these predictions. Figure 1.5 shows the ARPES results on Bi_2Se_3. The linear dispersing surface state can be seen from the Fermi energy downwards to approximately -0.3 eV. Close to the Fermi energy quadratically dispersing bulk states are visible inside the surface state down to $\approx$ -0.1 eV. The extended states from -0.3 eV downwards are attributed to the onset of the valence bands. Surface and bulk states were identified in the experiment by using energy dependent scans in which bulk states disperse while the surface state remains unchanged.

Results from the ARPES experiments of Chen *et al.* are shown in figure 1.6. Chen *et al.* analyzed Bi_2Te_3 samples with a varying amount of Sn doping. All sample spectra show a topological surface state connecting the bulk bands through the bulk bandgap (row ii). Furthermore, the constant energy cuts (in row i) reveal that the surface states have a strong

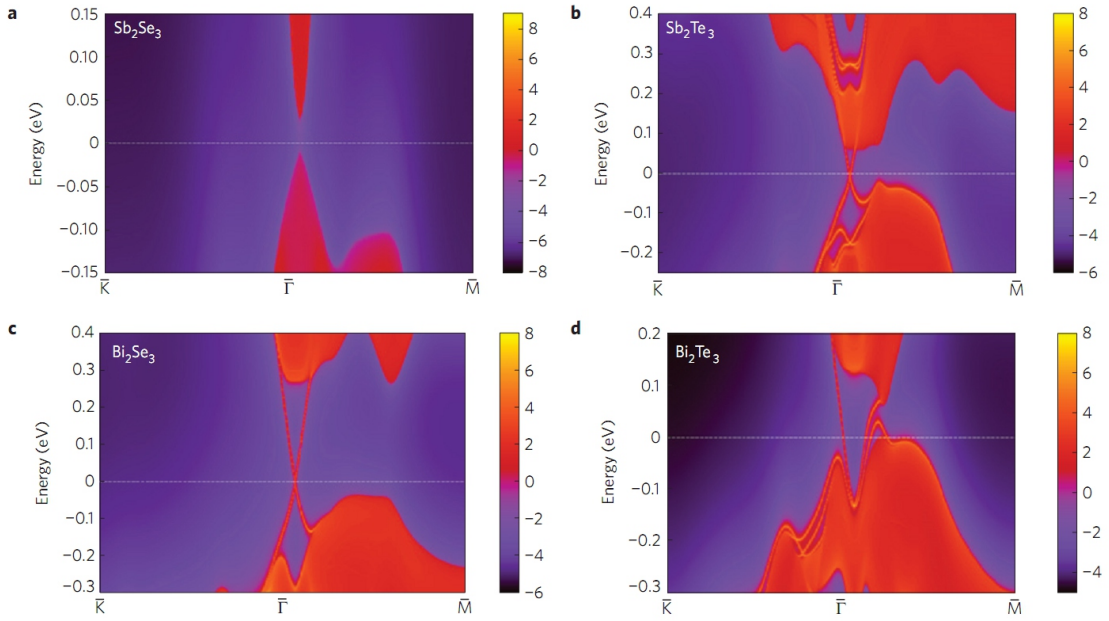

Figure 1.4: Bandstructure of Sb_2Se_3 (a), Sb_2Te_3 (b), Bi_2Se_3 (c) and Bi_2Te_3 calculated in the framework of *ab initio* density functional theory. Red denotes occupied bulk and surface states and blue the bulk band gap. Non-trivial surface states can be seen in Sb_2Te_3, Bi_2Se_3 and Bi_2Te_3. [13]

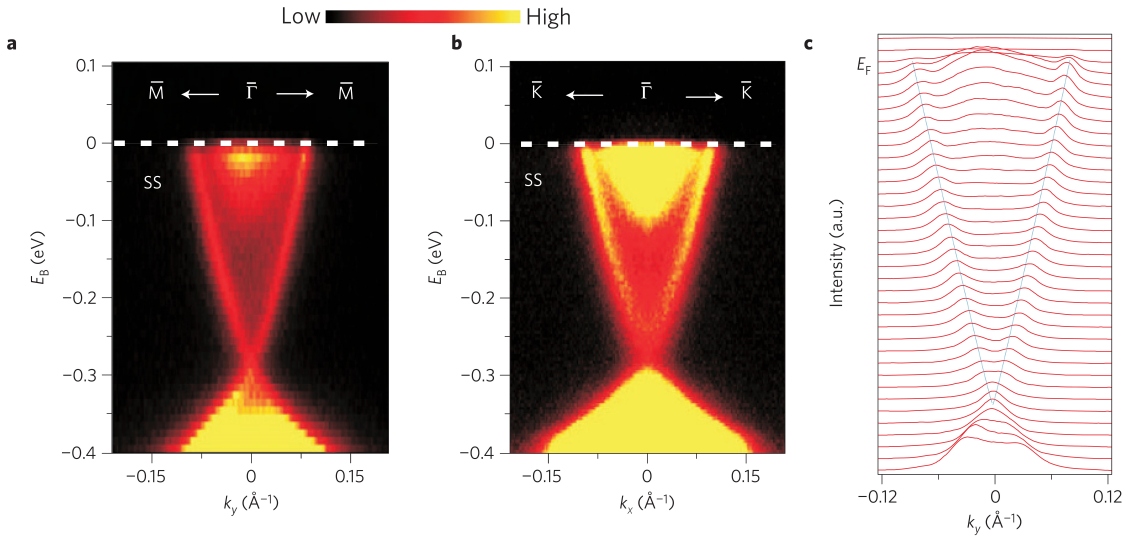

Figure 1.5: ARPES measurements on Bi_2Se_3. Panel a and b show cuts along the M-Γ-M and K-Γ-K directions. Panel c shows the momentum distribution curves corresponding to the measurement in panel a. [14]

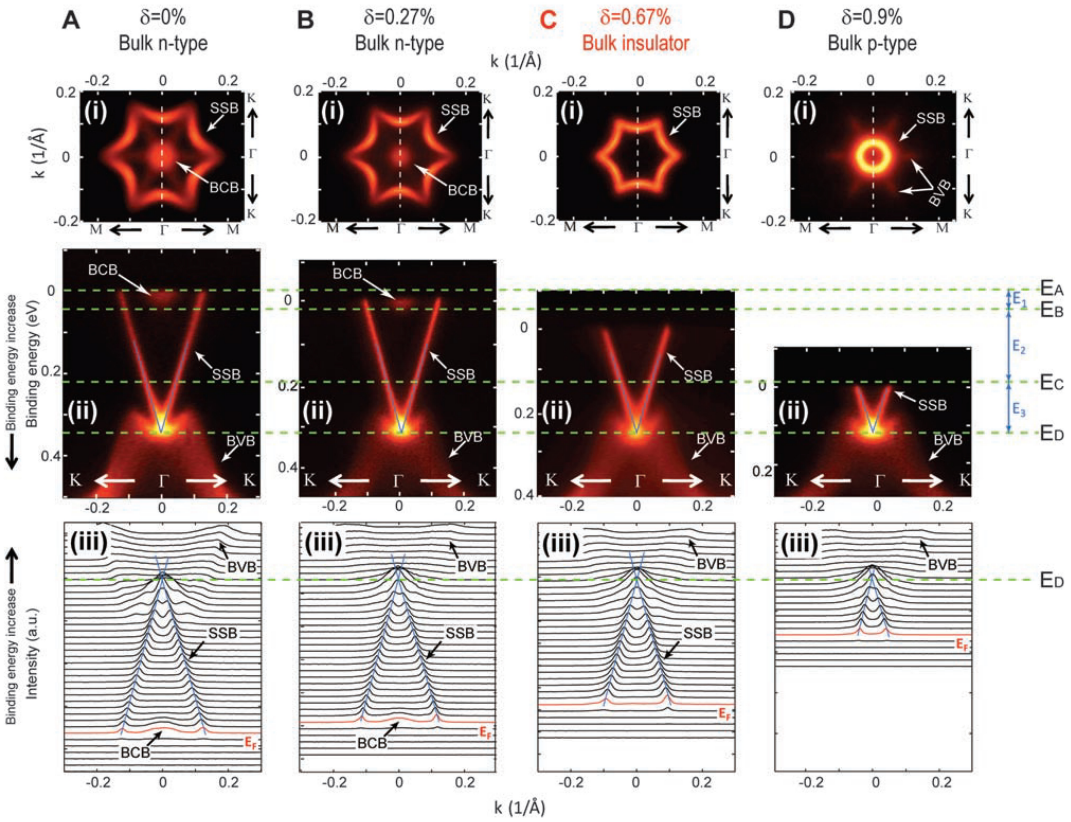

Figure 1.6: ARPES measurements on Bi_2Te_3. A to D shows the results for doping concentrations δ of 0%, 0,27%, 0.77% and 0.9%. Each section shows from top to bottom a constant energy cut at the Fermi energy, the band dispersion along the K-Γ-K direction and the corresponding momentum distribution curves. The abbreviations stand for SSB - surface state band, BCB - bulk conduction band, BVB - bulk valence band. [15]

hexagonal distortion in k, especially for energies far away from the Dirac point. This type of deviation from a fully linear Dirac state is called hexagonal warping and is caused by the interaction between bulk and surface states. The Sn-doping was used to compensate the intrinsic defect-doping which is common for this kind of materials (resulting in a Fermi energy high in the conduction band). Using different doping concentrations, Chen *et al.* were able to shift the Fermi energy in the bulk band gap (figure 1.6 C), showing that it is possible to reach a surface state dominated regime.

Due to the large band gap, the single Dirac cone surface states and also due to being easily available, Bi_2Se_3 and Bi_2Te_3 based materials are up to today the most researched 3-dimensional topological insulator materials. Unfortunately, as can also be seen from the results presented above, these materials suffer from a large amount of defect doping and additionally low carrier mobilities. This prevents unambiguous access to the surface states for example in transport experiments. An alternative is found in strained bulk HgTe layers. Even though the bulk band gap is much smaller than that of Bi_2Se_3 and Bi_2Te_3 based materials, this material has very few unwanted bulk carriers and high carrier mobilities. Furthermore, the rapid degradation of the surface states even under ultra high vacuum conditions that have been observed in Bi based compounds [33, 34] is not present in HgTe, thus allowing for easier access to the surface states in transport experiments. These advantages allowed for the first observation of the quantum Hall effect originating from the surface states of a 3-dimensional topological insulator in strained bulk HgTe [35]. An overview on our results concerning transport in these strained bulk HgTe layers will be given in chapter 3.

Chapter 2

Quantum spin Hall state in HgTe

This chapter has recently been published in a slightly shortened version in the book Topological Insulators [36].

The chapter will focus on the experimental properties of the quantum spin Hall effect in HgTe quantum well structures. HgTe quantum wells above a critical thickness are 2-dimensional topological insulators. The most prominent signature of the non-trivial topology in these systems is the occurrence of the quantum spin Hall effect when the Fermi energy is located inside the bulk band gap. We will present the main experimental results we obtained for transport in the quantum spin Hall regime and discuss how they confirm the prediction of the quantum spin Hall effect as a helical edge state system consisting of two counterpropagating oppositely spin polarized edge states.

2.1 HgTe quantum wells

First we focus on the bandstructure of HgTe and HgTe quantum wells, which distinguishes these systems from most other semiconductors. HgTe is a zincblende II-VI material. The bonds in the material are formed between the 6s electrons from the Hg atoms and 5p electrons from Te. Consequently the bands in the crystal which are close to the Fermi energy will evolve from these energy levels. This combination of s and p states is common for most conventional zincblende semiconductors. HgTe however is special in terms of the energetic position of the resulting energy bands. This is because both Hg and Te are relatively heavy atoms, so that relativistic corrections to the positions of the energy

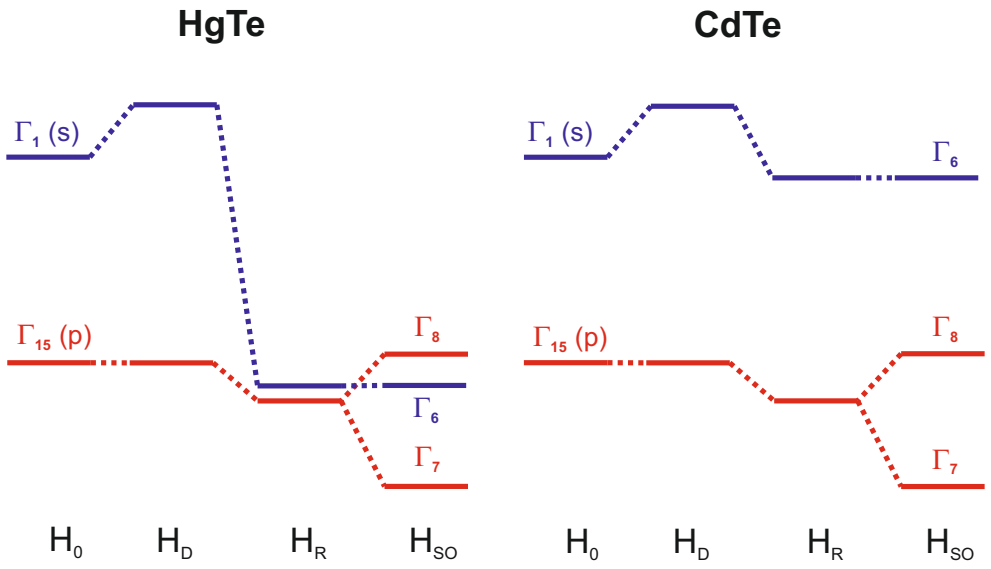

Figure 2.1: The evolution of the main energy bands in HgTe and CdTe. The impact of relativistic corrections onto the band positions is visualized. From left to right the influence of the Darwin term (H_D), the mass velocity correction (H_R) and finally the spin-orbit interaction (H_{SO}) is shown. The very strong mass velocity correction for the Hg s-states leads to a band inversion in HgTe. Adapted from [37].

levels become very important. Figure 2.1 schematically shows how the positions of the energy bands develop in HgTe (on the left) compared to those in CdTe (on the right) when applying these relativistic corrections [37]. The corrections to the unperturbed term H_0 are visualized in the following order from left to right: Darwin term H_D, the relativistic mass velocity correction H_R and finally the spin orbit coupling correction H_{SO}. While the Darwin correction is qualitatively similar for both compounds, the relativistic mass velocity correction is quite different. This is caused by the difference in atomic masses and core charges in Hg and Cd. The mass velocity correction for HgTe is so strong that the energy position of the Γ_6 state (originating from the Hg s-states) is lowered to nearly the same level as those of the Te p-states. Finally, the spin orbit interaction will split the p-states into the Γ_8 and Γ_7 states. As a result, the Γ_8 band is lifted above the Γ_6 state and we end up with the inverted band structure that distinguishes HgTe from most other materials. The spin orbit splitting in CdTe is similar to that in HgTe, since it occurs in the Te p-states, which are the same for both materials. But since H_R in CdTe is much

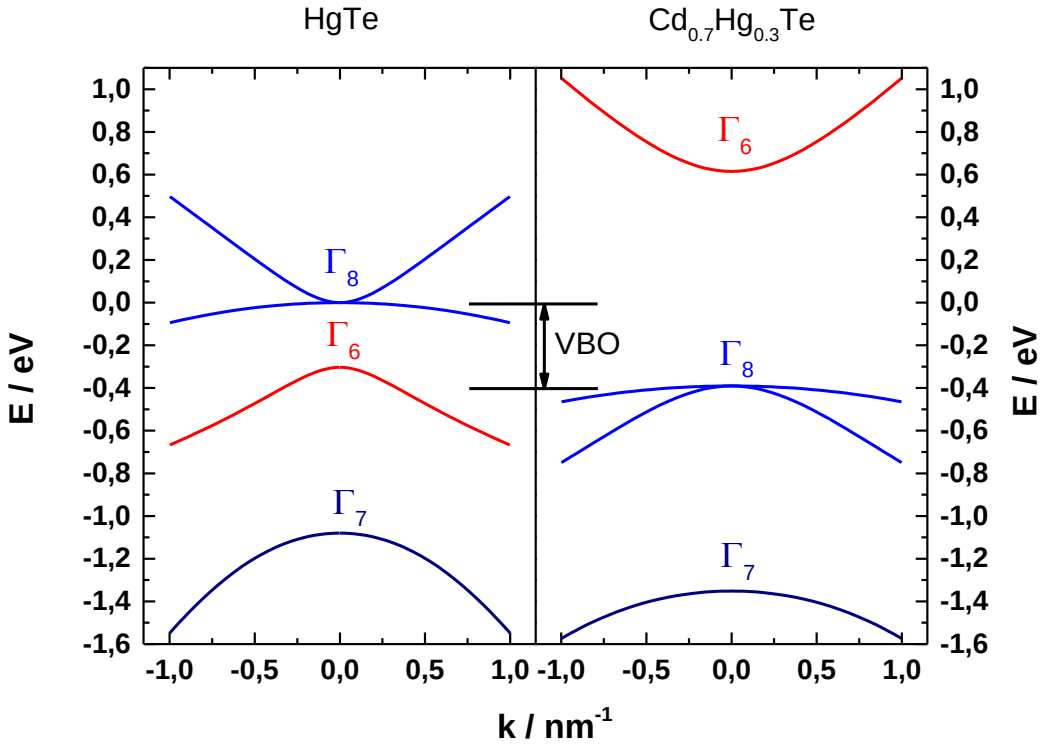

Figure 2.2: Band structure around the Γ-point for HgTe (left) and $Cd_{0.7}Hg_{0.3}Te$ on the right.

smaller than in HgTe, CdTe exhibits a normal band ordering with the Γ_6 state being the first conduction band state and the Γ_8 marking the first valence band state. The inversion is therefore a result of the interplay between H_R and H_{SO} in HgTe.

While the band inversion makes HgTe a topological material, it also has another consequence: Since the Γ_8 state consists of the degenerate light- and heavy-hole bands while the Γ_6 state only forms a single band, bulk HgTe has a semimetallic bandstructure, see fig 2.2 on the left [22, 38]. The Γ_6 band now is a valence band at an energy $\approx 300\ meV$ below the Γ_8 light and heavy-hole bands. Since the filling of the Γ_6 states only compensates one of the Γ_8 bands, the heavy-hole band remains occupied and thereby a valence band, while the light-hole band now becomes the conduction band.

Bulk HgTe thus is a topological semimetal. To turn it into a topological insulator it is therefore necessary to lift the Γ_8 degeneracy and open up a band gap. In general this can be achieved by lowering the point group symmetry. For thin, 2-dimensional layers, this is easily realized by growing quantum well structures. In three dimensions, the degeneracy

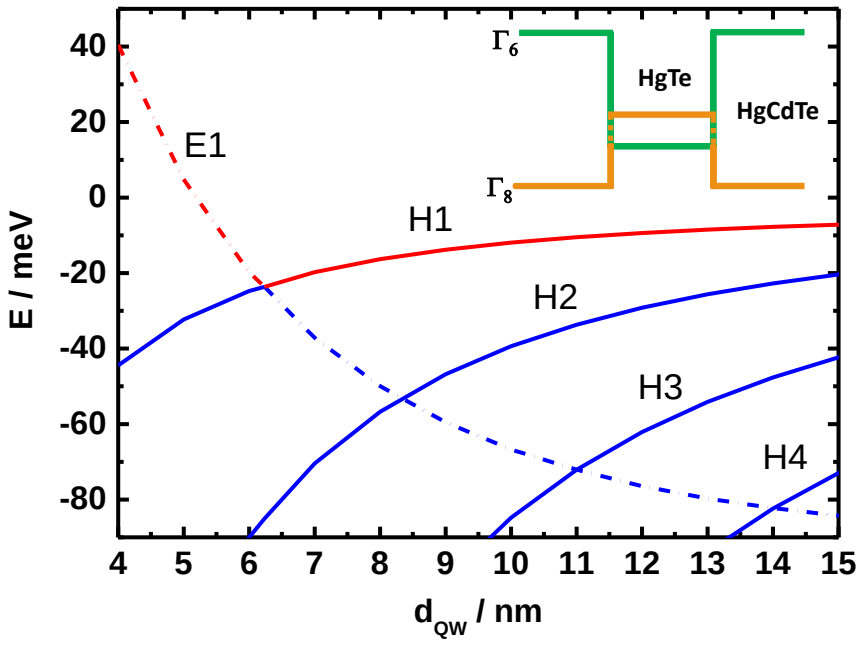

Figure 2.3: Subband energy against quantum well thickness for HgTe quantum wells. Subbands originating from Γ_6 states are labeled as E_i (dashed) and those evolving from the Γ_8 bands with H_i (straight lines). The colors indicate regions in which the subbands act as conduction band (red) and valence band (blue). HgTe quantum wells are so called type III quantum wells. The inset shows the schematic band edge profile for such a system.

can be lifted by utilizing growth induced strain [32].

For experiments on 2-dimensional topological insulators we use $Cd_{0.7}Hg_{0.3}Te$/HgTe/-$Cd_{0.7}Hg_{0.3}Te$ quantum well heterostructures. The band structure for $Cd_{0.7}Hg_{0.3}Te$ and HgTe at the Γ-point is shown in Figure 2.2. $Cd_{0.7}Hg_{0.3}Te$ exhibits a conventional band structure with Γ_6 above Γ_8 and a band gap of ≈ 1 eV. The resulting quantum wells are so called type III quantum wells with a characteristic band edge profile as shown in the inset of figure 2.3 [39]. In these quantum wells the band structure can be tuned over a wide range by changing the confinement strength through the well thickness. In figure 2.3 the evolution of the subband energy versus the well thickness is shown. Subbands depicted in red act as conduction bands in the corresponding region while those in blue are valence bands. For wide quantum wells, the confinement energy is small and the subband ordering retains the band inversion of bulk HgTe with the H_1 subband (originating from the Γ_8

states) being the first conduction band and the E_1 subband (originating from the Γ_6 band) being one of the valence bands. For thin quantum wells however E_1 becomes the first conduction band and H_1 the first valence band [24, 7]. These two regimes correspond to the topologically trivial case (thin quantum wells) and the topological insulator case (thick quantum wells). Since the topology changes between these regimes, they have to be connected by a state with a vanishing band gap. For a critical thickness of 6.3 nm the band gap collapses and a zero-gap state is formed [7, 40, 29]. These characteristics will enable us to test the 2-dimensional topological insulator regime by comparing its characteristics with those of the normal regime. This will be the content of the next section.

2.2 The quantum spin Hall effect

The HgTe quantum wells used in the experiments are grown by molecular beam epitaxy [41]. This enables the fabrication of layers with high crystalline quality while at the same time granting high control over quantum well thickness, carrier density and structure inversion asymmetry. To enable experiments in the quantum spin Hall regime, the quantum wells have to have low carrier densities (to reach the insulating regime) and simultaneously high carrier mobilities (to provide large inelastic mean free paths for the transport experiments). The development and constant improvement of the MBE growth regarding these properties was a major contribution in making the following experiments possible. Today carrier densities can be freely tuned from well below $1 \times 10^{11}\,\mathrm{cm}^{-2}$ up to the mid $10^{12}\,\mathrm{cm}^{-2}$ regime while carrier mobilities can reach well above $1 \times 10^{6}\,\mathrm{cm}^2\,\mathrm{V}^{-1}\,\mathrm{s}^{-1}$ implying a mean free path of several micrometers. Figure 2.4 shows a standard magnetotransport characterization measurement of the quantum well sample Q2369. Here, the mobility reaches already $1.1 \times 10^{6}\,\mathrm{cm}^2\,\mathrm{V}^{-1}\,\mathrm{s}^{-1}$ without any applied gate voltage. The carrier density is relatively low ($4.3 \times 10^{11}\,\mathrm{cm}^{-2}$) which enables shifting the Fermi level across the bulk band gap to explore the insulating regime.

The quantum spin Hall effect is the signature state of a 2-dimensional topological insulator and it describes the existence of edge states on the sides of a 2-dimensional topological insulator system. These edge states are supposed to consist of two counterpropagating oppositely spin polarized edge channels in the band gap of the material [6, 19, 22]. Figure 2.5 shows a cartoon picture of the quantum spin Hall effect in a HgTe quantum well system.

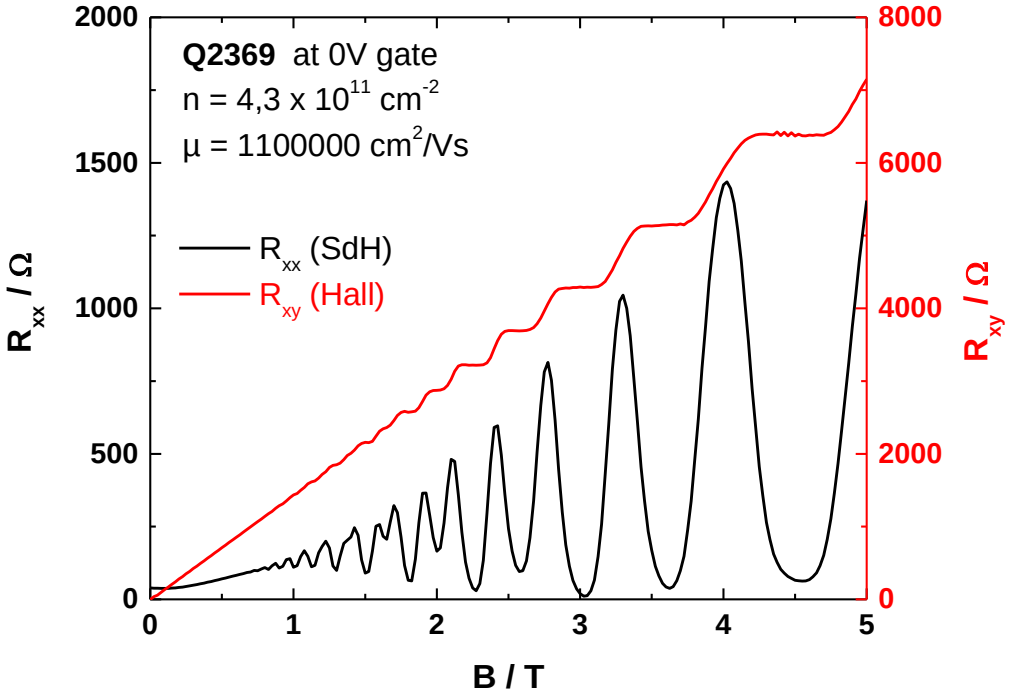

Figure 2.4: Magnetotransport characterization of sample Q2369.

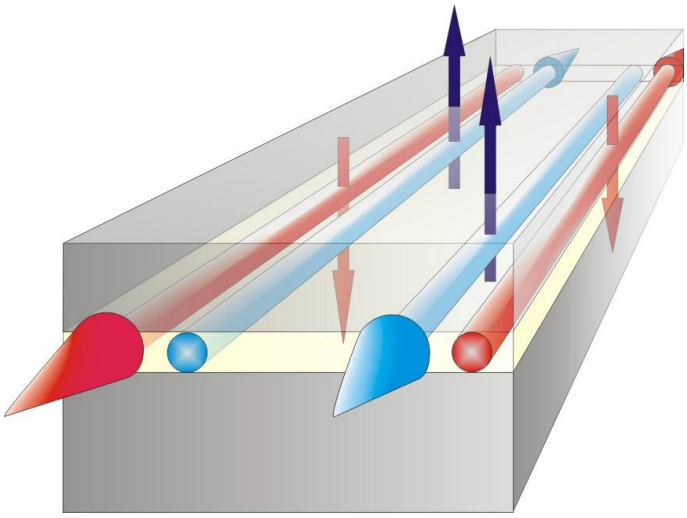

Figure 2.5: Cartoon picture of the quantum spin Hall effect in HgTe quantum wells.

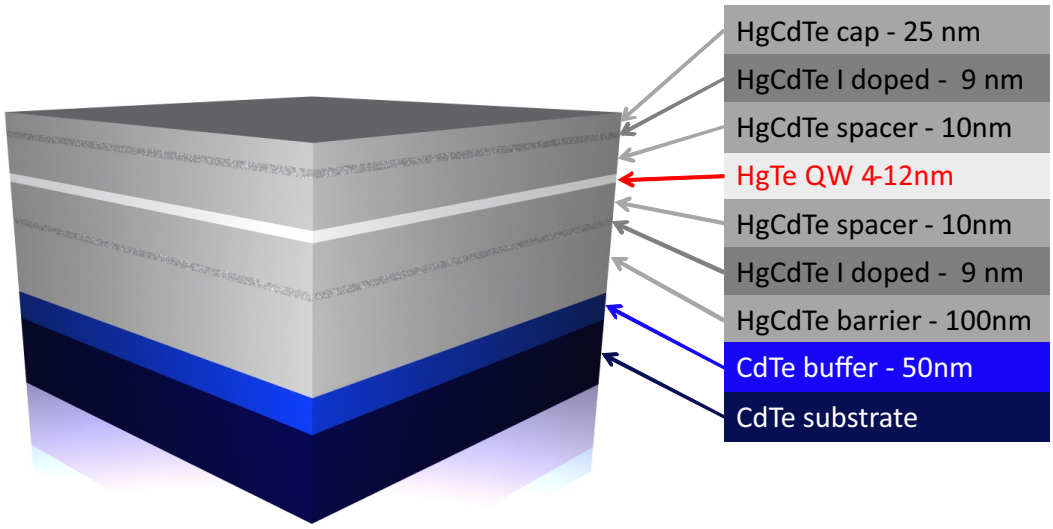

Figure 2.6: Schematic layer sequence of a $Cd_{0.7}Hg_{0.3}Te$/HgTe/$Cd_{0.7}Hg_{0.3}Te$ quantum well structure used in the experiments

To find evidence for these edge states we perform transport measurements on HgTe quantum well devices [8, 42]. The $Cd_{0.7}Hg_{0.3}Te$/HgTe quantum well structures are fabricated by molecular beam epitaxy on $Cd_{0.96}Zn_{0.04}Te$ substrates [41]. The quantum well structures are modulation doped (by Iodine doping of the barriers) such that the initial carrier densities are in the low 10^{11} cm^{-2} regime. Fig 2.6 shows a schematic drawing of the layer sequence of a symmetric quantum well structure with typical layer thicknesses. The electron mobilities are typically in the order of 3×10^5 $cm^2V^{-1}s^{-1}$ or higher. The measurements were carried out on 6-terminal Hallbar devices, a device schematic is shown as inset in figure 2.7. These were patterned with low temperature optical and e-beam lithography processes onto the heterostructures. The samples are fitted with top gate structures consisting of a Ti/Au layer. Since HgTe, like all II-VI semiconductors, exhibits a leaky Schottky barrier when connected to a metal, the gates are insulated from the quantum well structure by a SiO_2/Si_3N_4 multilayer insulator film. The gate electrodes can be used to tune the carrier density continuously from n-conductance through the band gap to p-conductance and to modify the electric field across the well. Transport measurements are done at temperatures of 30 mK in a ^{3}He/^{4}He-dilution refrigerator fitted with a 18 T magnet and at 1.8 K in a ^{4}He cryostat fitted with a 10 T magnet.

To find evidence for the existence of the quantum spin Hall effect we measure the longitudinal resistance of the Hallbar while shifting the Fermi level through the band gap by using the top gate. In a two-dimensional topological insulator system one expects to detect

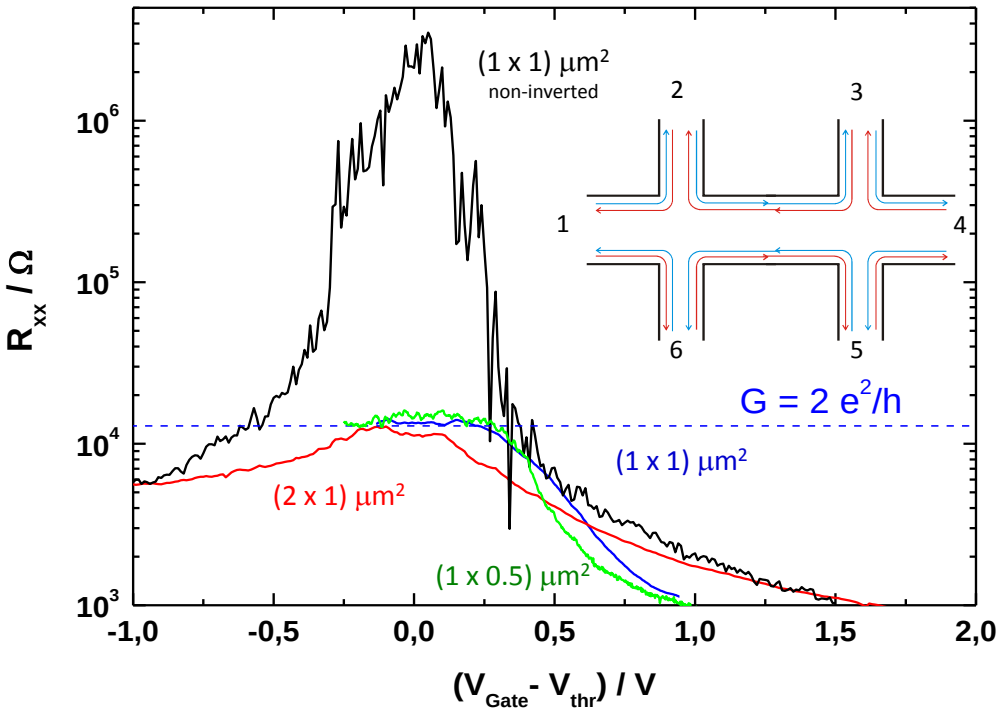

Figure 2.7: Four terminal longitudinal resistance of HgTe quantum well structures in the inverted and normal regime. The black trace was taken on a sample in the normal regime while the red blue and green curves correspond to samples in the inverted state. The dimensions of the Hallbar devices are given by the labels in their corresponding colors. The inset shows a schematic drawing of a Hallbar structure with the quantum spin Hall edge states.

a quantized conductance/resistance when the Fermi energy is located inside the band gap. In a conventional system the conductance should drop to zero/ the resistance should rise to very large values in this situation. The measurements have been performed on small sized Hallbars with dimensions of some few μm. This size is chosen to ensure that the system dimensions are below the inelastic mean free path since inelastic scattering events could introduce backscattering in the helical edge states [8, 25]. The measurements are performed in a typical 4-terminal geometry with the current being applied between contacts 1 and 4 and the longitudinal voltage detected between the contacts 2 and 3 or 5 and 6 respectively.

The resulting data is shown in figure 2.7. Curves for the following samples are displayed: The black curve has been obtained from a Hallbar sample with dimensions of L $\times$ W =

$(1 \times 1)\ \mu m^2$ patterned from a 5.5 nm thick quantum well. The results for a 7.3 nm thick quantum well are shown in green, using a Hallbar with L $\times$ W = $(1 \times 0.5)\ \mu m^2$, and in red and orange for L $\times$ W = $(1 \times 1)\ \mu m^2$. Finally, the blue curve represents the results obtained on a sample with a length to width ratio of $(2 \times 1)\ \mu m^2$ fabricated from a 7.5 nm thick quantum well. In a control experiment, we observe a high resistance for the sample with conventional band ordering (black). In this sample, the resistance rises above $10^6\ \Omega$ when the Fermi energy crosses the band gap indicating a conventional insulator behavior. For samples with an inverted band structure, however, the resistance stays finite in the band gap with values close to $h/2e^2$. This is the expected value for transport through a helical edge state system in the measured configuration (a detailed explanation will follow in the next section). These results thus provide first evidence for the existence of the quantum spin Hall effect in inverted HgTe quantum wells.

Apart from the observation of a quantized resistance the experiment additionally provides an indication that the observed effect is caused by edge channel transport. As one can see from the measurements in figure 2.7, the value of $h/2e^2$ is reached independent of the sample geometry of the Hallbars. This is typical for edge transport and cannot be explained by normal diffusive transport behavior. While this result thus provides first evidence for the existence of edge state transport in inverted HgTe quantum well structures we so far did not present evidence for the proposed helical nature of these edge channels. To do so we performed a set of non-local transport experiments in the quantum spin Hall regime. These experiments will be described in the following section.

2.3 Nonlocal transport in the quantum spin Hall state

The measurements presented in the last section have been performed in a standard 4 terminal geometry and we observe a conductance of $2e^2/h$ when measuring the longitudinal resistance. At first glance, when compared to similar measurements on quantum Hall systems this is a somewhat surprising observation. For chiral quantum Hall edge states, a 4 terminal longitudinal measurement will yield a vanishing longitudinal resistance. This difference can be understood when applying the Landauer-Büttiker quantum transport formalism [43, 44] to the helical edge state system of the quantum spin Hall effect. In the the Landauer-Büttiker formalism, the relation between current and voltage is described as:

$$I_i = \frac{e^2}{h} \sum_j (T_{ji} V_i - T_{ij} V_j). \tag{2.1}$$

In this equation, I_i denotes the current flowing out of the ith contact into the sample region, V_i is the voltage on the ith contact and T_{ij} the transmission probability between contact i and j. To ensure that the total current is conserved, one demands that $\sum_i I_i = 0$; the voltage leads can be defined by setting the net current on the corresponding contact to zero.

Solving this equation for a general two-dimensional sample can be complicated since the number of conduction channels scales with the sample width, which will lead to a complex and non-universal transmission matrix T_{ij}. For edge channel transport, however, the equation is significantly simplified. For example, in the $\nu = 1$ quantum Hall state only the elements $T_{i+1,i} = 1$ remain while all other elements vanish. This is due to the chiral nature of the quantum hall edge states allowing transport only in one direction along one edge of the sample. Edge states for electrons moving in opposite direction are located on opposite sides of the sample. If we now apply this formula to the quantum Hall case and calculate the expected resistance for a 4 terminal measurement of the longitudinal resistance on a 6 terminal Hallbar we indeed get $R_{14,23} = 0$.

In the case of the quantum spin Hall effect, however, the result will be different, since there are two counterpropagating channels on each side of the sample (as schematically shown in the inset of figure 2.7). The transmission of each edge state is still perfect, as in the quantum Hall case, since the edge states are protected against backscattering by time reversal symmetry. But since there is a forward and backward moving edge channel on each side of the sample, the non-vanishing edge transmission matrix elements are now given by

$$T_{i+1,i} = T_{i,i+1} = 1. \tag{2.2}$$

The result for the 4 terminal resistance in such a system is $R_{14,23} = h/2e^2$ which corresponds to the values measured in the experiments shown in the previous section. This result also implies that in the quantum spin Hall regime, all contacts to the mesa act as a source for dissipation. (This is in contrast to the situation in the quantum Hall regime where contacts downstream from the voltage probes do not influence the potentials at the voltage probes themselves.)

Contacts are metallic regions with a quasi infinite number of low energy degrees of free-

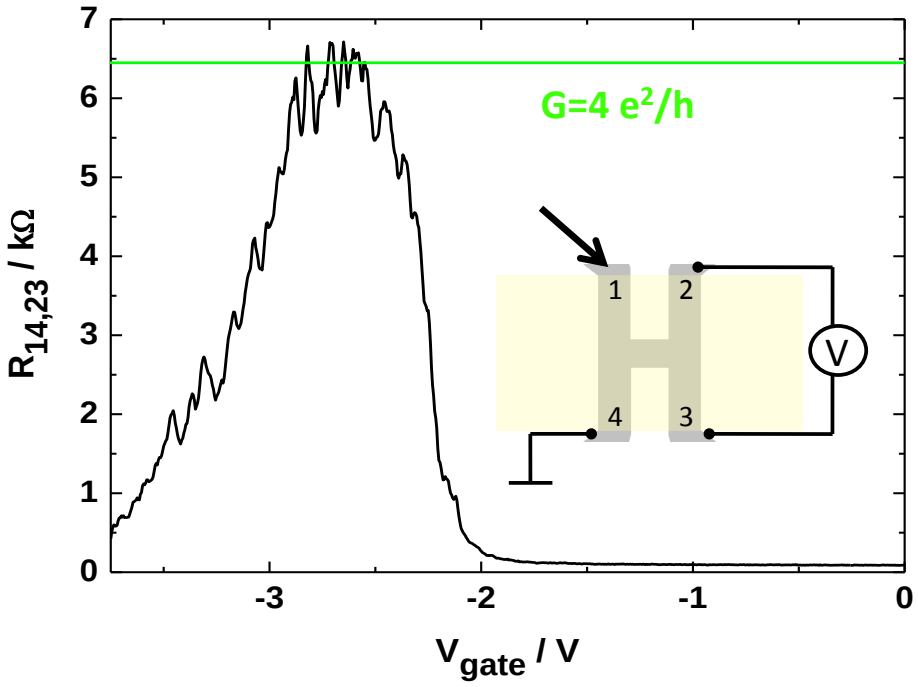

Figure 2.8: non-local measurement on a 4-terminal sample. the green line indicates the expected conductance value of $4e^2/h$

dom available with which the quantum spin Hall states can interact. This will introduce irreversibility on the macroscopic level, break the time reversal symmetry and destroys the phase coherence. This effectively broken time reversal symmetry inside the contacts lifts the protection against dissipation of the quantum spin Hall states [25].

The expected differences between chiral and helical edge states can be further tested in non-local transport experiments [25]. These experiments are conducted on samples which have been specially designed to observe non-local signals (schematically shown in the insets of figure 2.8 and figure 2.9).

Figure 2.8 shows a measurement in a fully non-local configuration on a device which for obvious reasons we refer to as an "H-bar". In this experiment the current is applied along one part of the sample between contacts 1 and 4, while the voltage is measured between contacts 2 and 3 on the other leg. The measured non-local signal reaches ≈ 6.5 kΩ when the Fermi energy is located inside the band gap. This result agrees very well with the expected conductance value of $4e^2/h$ or 6.45 kΩ in resistance from Landauer-Büttiker

calculations. This data is direct evidence of edge channel transport; neither diffusive nor ballistic transport will show such a large non-local signal.

A striking difference between chiral (quantum Hall) and helical (quantum spin Hall) edge states arises when one uses the two measurement configurations shown in Fig 2.9. In the upper panel a measurement in a typical longitudinal configuration is presented (same data as the blue trace in figure 2.7). The current is applied between the contacts 1 and 4 while the voltage is probed between contacts 3 and 4. This measurement yields a conductance of $2e^2/h$ as expected from the Landauer-Büttiker model. If one now applies the current between contacts 1 and 3 and measures the voltage between contacts 4 and 5 (bottom inset) we measure a different value of $3e^2/h$. This result is consistent with calculations for helical edge states and distinguishes the quantum spin Hall from the quantum hall system. For chiral edge channels (as well as in diffusive transport) there is only one longitudinal resistivity and these two configurations should deliver the same resistance values. From these insights and observations we can understand the importance of contacts and contact configurations for resistance measurements in the quantum spin Hall state.

The Landauer-Büttiker picture can also be used to explain why relatively small samples are needed to observe these effects. For this we can consider the influence of potential fluctuations on the quantum spin Hall state. In our samples a main source for potential fluctuations are interface states between the gate oxide and the sample surface. These interface states screen the gate potential locally and thereby lead to potential fluctuations in the 2-dimensional electron gas. A large enough potential fluctuation will shift the conduction (valence) band edge below (above) the Fermi energy locally and a metallic puddle will form. If this puddle is large enough and has sufficient spin orbit coupling it can lead to inelastic scattering and loss of spin information thus effectively acting in the same way as a contact. A cartoon picture showing the influence of a potential fluctuation on the quantum spin Hall state is shown in figure 2.10.

The 3 panels show the impact of a metallic puddle (grey) - growing in size from top to bottom - onto the transport properties of the quantum spin Hall state. The upper panel shows the situation for small metallic puddles. If these puddles are small enough they will not allow for inelastic scattering and the loss of phase coherence. Thus transport will only happen in the two edge channels connecting the macroscopic contacts in the direction of the applied voltage and the transport will be completely phase coherent (denoted by solid lines). Larger puddles will allow for partial dephasing and backscattering (middle panel). Incoherent transport is visualized as dotted lines. Even larger metallic puddles

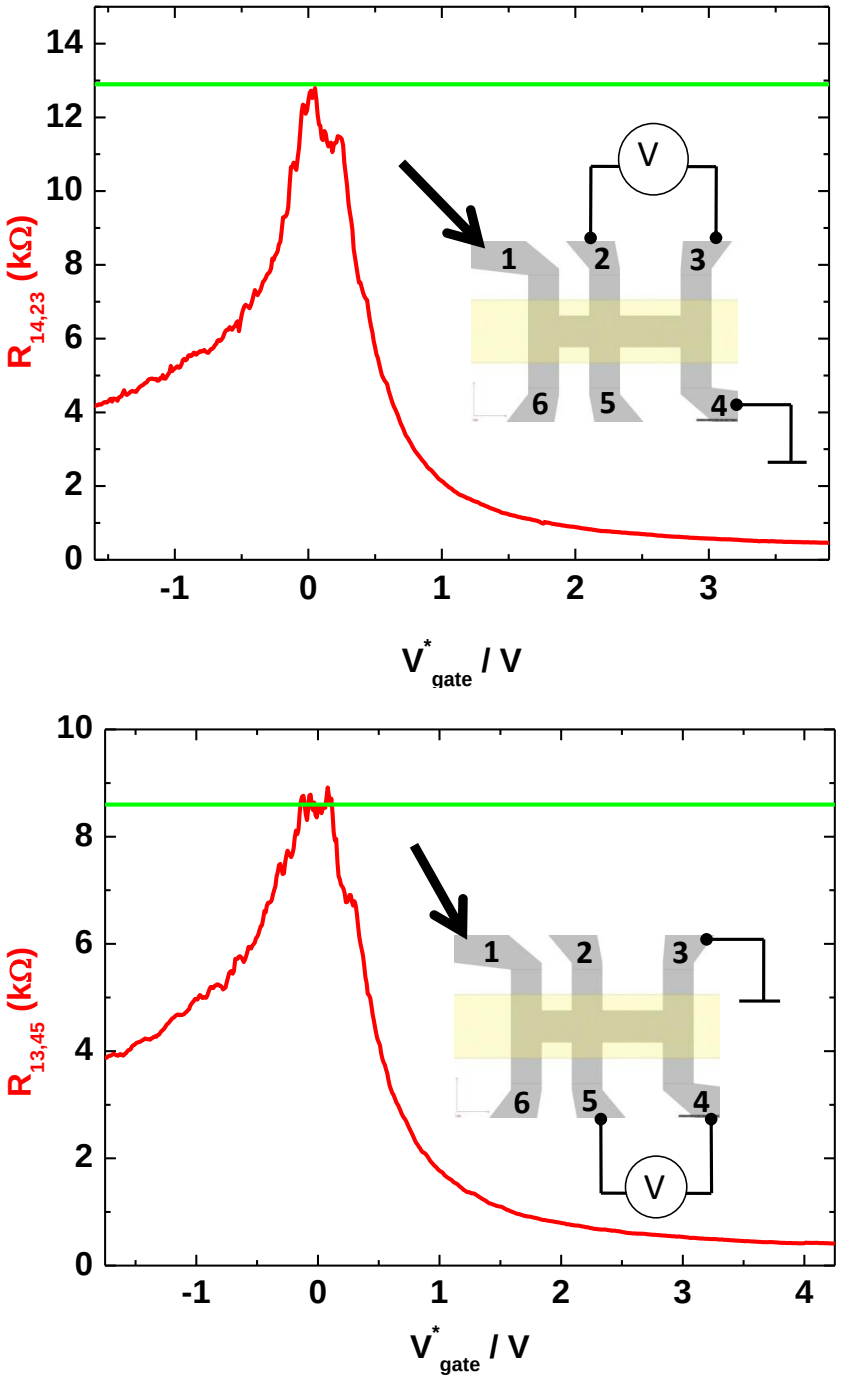

Figure 2.9: non-local measurements in the quantum spin Hall state. The schematic sample layout and the measured contact configurations are displayed as insets. The green lines indicate the expected quantized conductance values.

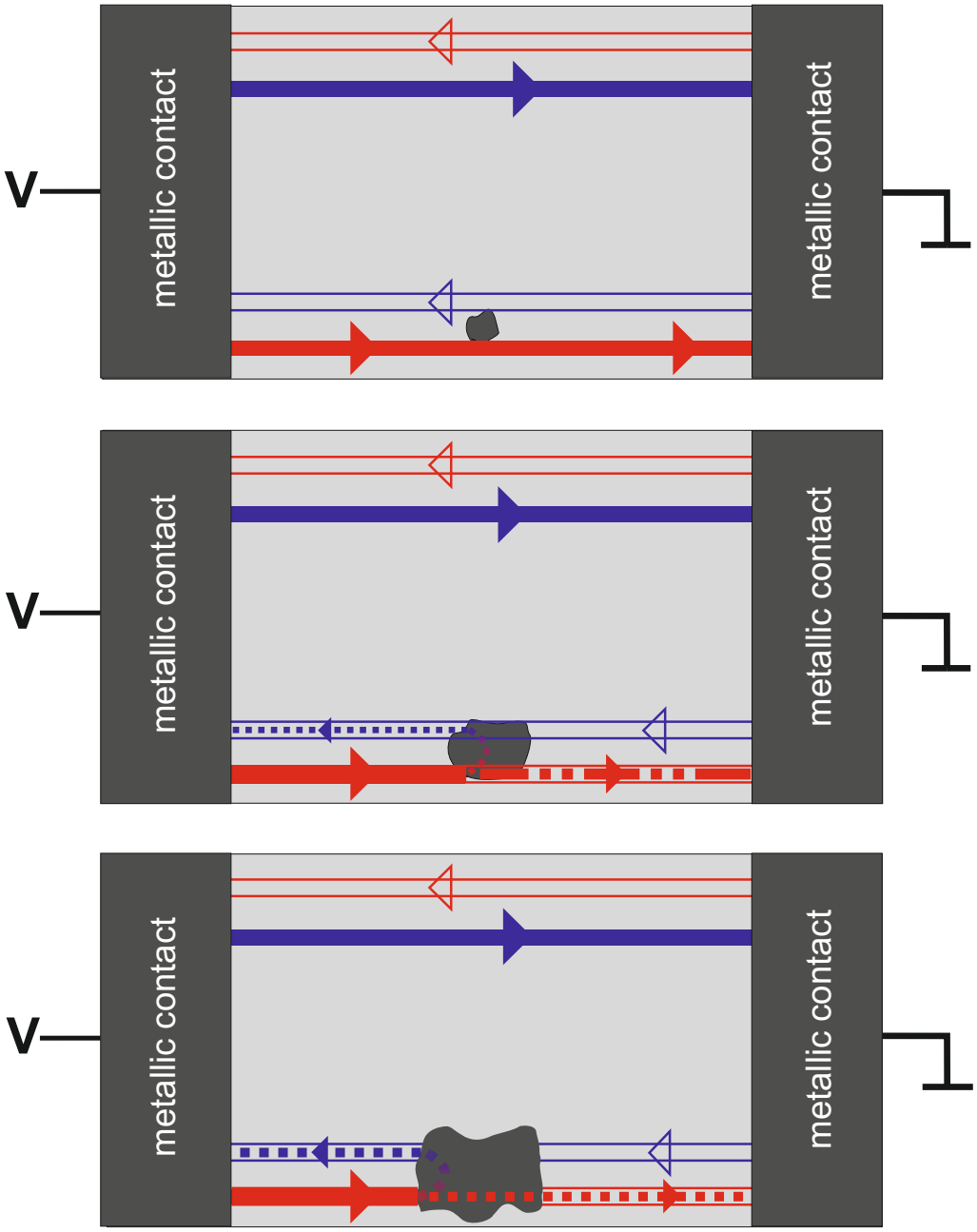

Figure 2.10: Cartoon picture showing the impact of potential fluctuations on the quantum spin Hall effect. For large enough potential fluctuations a metallic puddle is formed (grey). The 3 panels show the influence of a metallic puddle (growing in size from top to bottom) onto the edge channels.

(lower panel) will lead to completely incoherent transport thus leading to a fully dissipative behavior similar to the situation in macroscopic contacts. Further, more in depth discussion and examples can be found in the supplementary material of reference [25].

2.4 Spin polarization of the quantum spin Hall edge states

So far we obtained evidence for the existence of the quantum spin Hall effect and its edge state nature. The spin polarization of the edge states however still needs confirmation. This will be the topic of the present section.

The direct detection of a magnetic field generated by the spin polarized carriers inside a helical edge state is challenging. The magnetic field generated by a current flowing through the edge state exceeds the component originating from the spin polarized electrons [45]. This problem can be circumvented by converting the magnetic into an electric signal. This can be achieved by utilizing the spin Hall effect in a degenerate (metallic) semiconductor and its counterpart, the inverse spin Hall effect. The spin Hall effect is the appearance of a spin current flowing perpendicular to a charge current in systems where spin orbit interaction is present [46, 47]. In the case of the inverse spin Hall effect, the Onsager counterpart of the spin Hall effect, a spin current is transformed into a charge current.

HgTe quantum wells feature strong spin orbit interaction effects due to their narrow band gaps and the large atomic spin orbit coupling. This leads to a large Rashba splitting in HgTe quantum wells when the Fermi energy is located in the conduction or valence band and a perpendicular electric field is applied across the structure [48]. Such strong Rashba effects enable the observation of the ballistic intrinsic spin Hall effect [49, 50, 51]. Combining the spin Hall and the inverse spin Hall effect in a non-local experiment allowed us to detect the spin Hall effect in an all electrical measurement [52]. The sample design is similar to the one used in the previous section, a simple H-bar with a single top gate. To suppress the non-local signal originating from the quantum spin Hall state (which is much larger than the expected response from the spin Hall effect) we adjust the sample dimensions and add additional contact leads. The width of the legs and connecting parts is reduced to approximately 200 nm, this will enable backscattering between the quantum spin Hall channels of opposite edges [53]. The added contacts and increased gate dimensions will lead to additional backscattering in the quantum spin Hall edge states. The

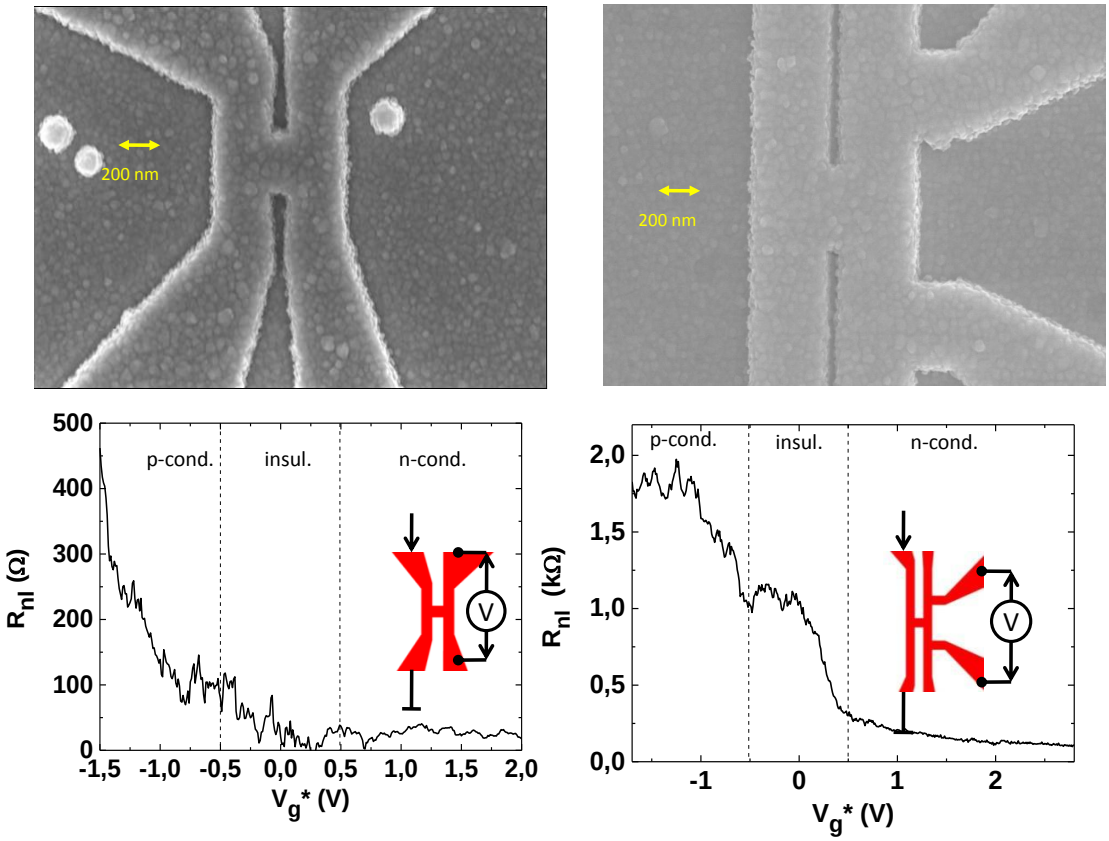

Figure 2.11: Non-local measurements of the spin Hall effect in HgTe quantum wells. The upper panels show electron micrograph of the H-structures used in the experiments. The experimental results of the non-local measurements are shown in the lower panels. Dimensions are shown in yellow.

undesired non-local signals originating from the quantum spin Hall effect are also suppressed when using quantum wells below the critical thickness with a conventional band ordering. This kind of samples yield similar results to the ones discussed below, see [52]. Figure 2.11 shows the electron micrographs of two inverted quantum well samples (upper panels) and the corresponding non-local measurements (lower panel). The measurement configurations are depicted in the insets. A current is applied to one leg of the H-bar and the corresponding non-local resistance is measured on the other leg. The non-local resistance is then recorded depending on the applied gate voltage. We observe a strong non-local response in both samples when the Fermi level is tuned into the p-conducting region while the non-local resistance is comparatively low for the n-conducting case. This behavior is expected for the spin Hall effect in HgTe quantum wells since the strength of the intrinsic spin Hall effect depends on the Rashba k-splitting [49]:

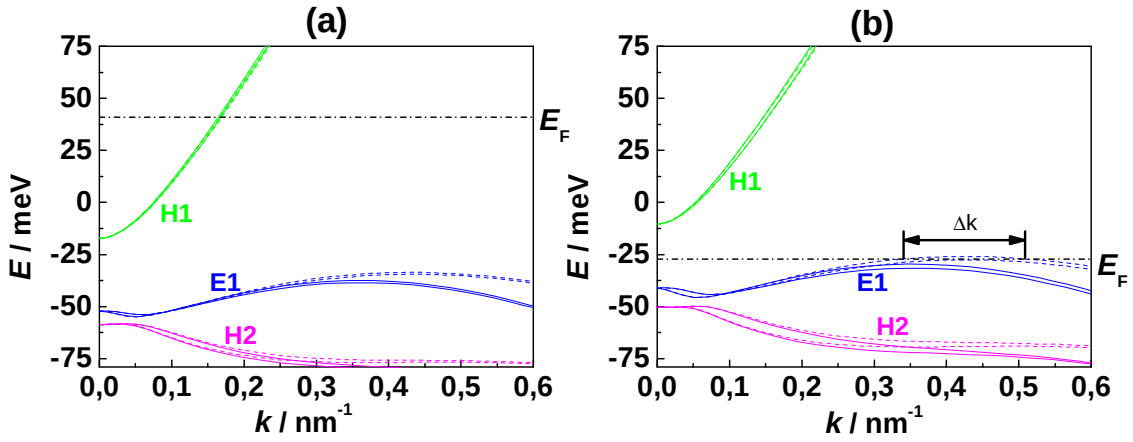

Figure 2.12: Band structure calculations including the Rashba splitting for one of the samples used in the experiments. a) Fermi level is situated in the conduction band, b) Fermi energy touches the first valence band. Δk marks the k-splitting in this case

$$j_{s,y} = \frac{-eE_x}{16\pi\lambda m}(p_{F+} - p_{F-}) \propto \Delta k, \tag{2.3}$$

with $j_{s,y}$ the spin current in y direction, e the electron charge, E_x the electric field applied in x direction, λ the Rashba coupling constant, the effective electron mass m, p_{F+} and p_{F-} the Fermi momenta for the Rashba split bands, respectively and Δk the k-splitting. Figure 2.12 shows exemplary band structure calculations for one of the samples used in the experiments [39, 52]. In figure 2.12 a) the band structure is calculated for the Fermi level in the conduction band. One can see that the k-splitting between the two Rashba split subbands contributing to the transport (H1 bands - green) is relatively small in this situation. However, if the Fermi level touches the first conduction band (E1 - blue), as shown in figure 2.12 b), the k-splitting can be an order of magnitude larger than in the conduction bands, matching our experimental observations. A more detailed description of our work on the spin Hall effect can be found in chapter 4.

For the detection of the spin polarization of the quantum spin Hall states we now utilize the metallic spin Hall effect [26]. The device design is once again similar to the H-bar design used to detect non-local signals shown in the previous section (figure 2.9). The H-bar is now fitted with 2 top gates, one for each leg of the structure, so that we can tune the carrier density independently in both legs. Figure 2.13 shows an electron micrograph of the split gate structure used in the experiments, the sample dimensions are displayed in yellow.

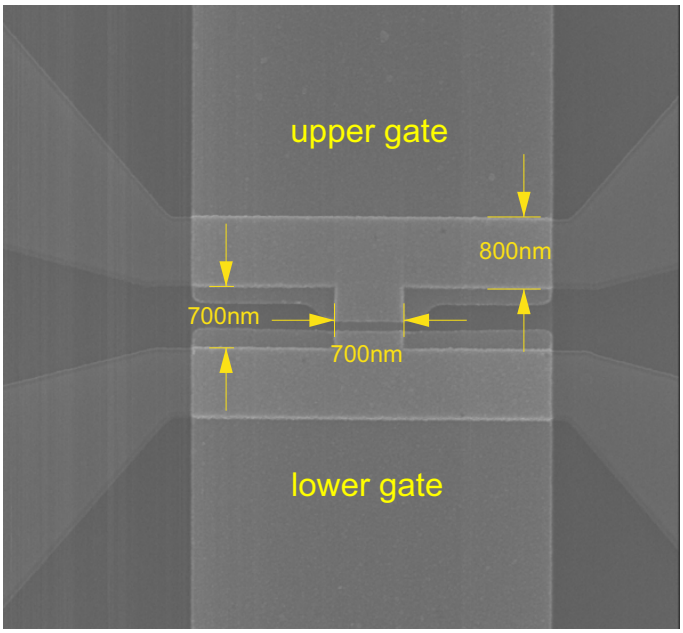

Figure 2.13: Electron micrograph of a split gate H-structure used in the experiments. Dimensions of the sample are shown in yellow.

The experiment follows two main approaches: The first approach is to use the quantum spin Hall channels to detect the spin polarized currents from the spin Hall effect. The measurement configuration for this approach is schematically drawn in figure 2.14. The upper leg between contacts 1 and 2 will be tuned into the quantum spin Hall state. In the lower leg the Fermi energy is located in the metallic regime of either the conduction or valence band. If we now apply a current in the lower leg between contacts 3 and 4, this current will lead to a spin polarized current flowing perpendicular to the charge current. This spin current causes a difference in chemical potential for the two spin states and the quantum spin Hall states will couple selectively to the potential of the matching edge channel. The potential difference will thereby be transferred to contacts 1 and 2 and should lead to a non-local voltage signal that can be detected in the experiment. Non-local signals can only be observed when the metallic regions exhibit a spin Hall effect and the quantum spin Hall states are spin polarized otherwise the non-local voltage will be zero. Note that the above experiment is a direct demonstration of the magnetoelectric effect of the topological surface state in a 2-dimensional system [54]. The detection of non-local signals is therefore evidence for the spin polarization of the quantum spin Hall states. We can furthermore test if the spin Hall effect signal strength differs in the n- and p-conducting regime as one would expect from the different spin orbit splitting strengths. Finally we can check if we are able to observe a strong non-local signal if we tune the Fermi level

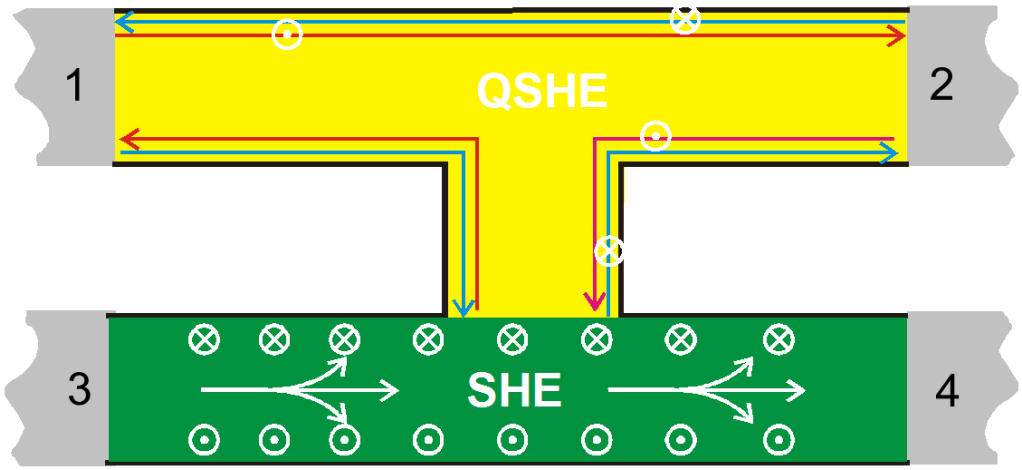

Figure 2.14: Concept for utilizing the quantum spin Hall state as spin polarization detector. Here the spin Hall effect, induced by a current flowing in the lower leg, leads to a spin accumulation on the edges of the leg which can be transformed into a non-local signal by the spin polarized quantum spin Hall states.

into the gap in both legs of the structure, similar to the experiments we described in the last section.

During the measurement, the gate voltage on the lower leg is held constant while the upper gate is swept such that the Fermi level changes from n-type metallic through the band gap to p-type metallic. This means the spin injection properties from the lower leg (where the current is applied) remain unchanged while we vary the upper gate voltage to investigate the spin detection capabilities of the different regimes.

Figure 2.15 shows the resulting non-local resistance signals for this measurement configuration. The measurement was performed for three different, fixed, gate voltages on the lower gate. Panel a) shows the non-local resistance for metallic p-type transport and panel b) for metallic n-type transport in the lower leg. These measurements show a significant increase in the non-local signal and the occurrence of a pronounced maximum when the gate voltage is swept through the quantum spin Hall regime. The maximum non-local resistance that can be observed is an order of magnitude higher for injection from the p-conducting regime. This is again in agreement with the difference in spin Hall effect strength between valance and conduction band as mentioned above. The existence of these large non-local signals when the detection occurs through quantum spin Hall states is evidence for the spin polarization of the quantum spin Hall edge states. These signals can only arise if the metallic region exhibits a spin Hall effect which can be detected by spin polarized edge states.

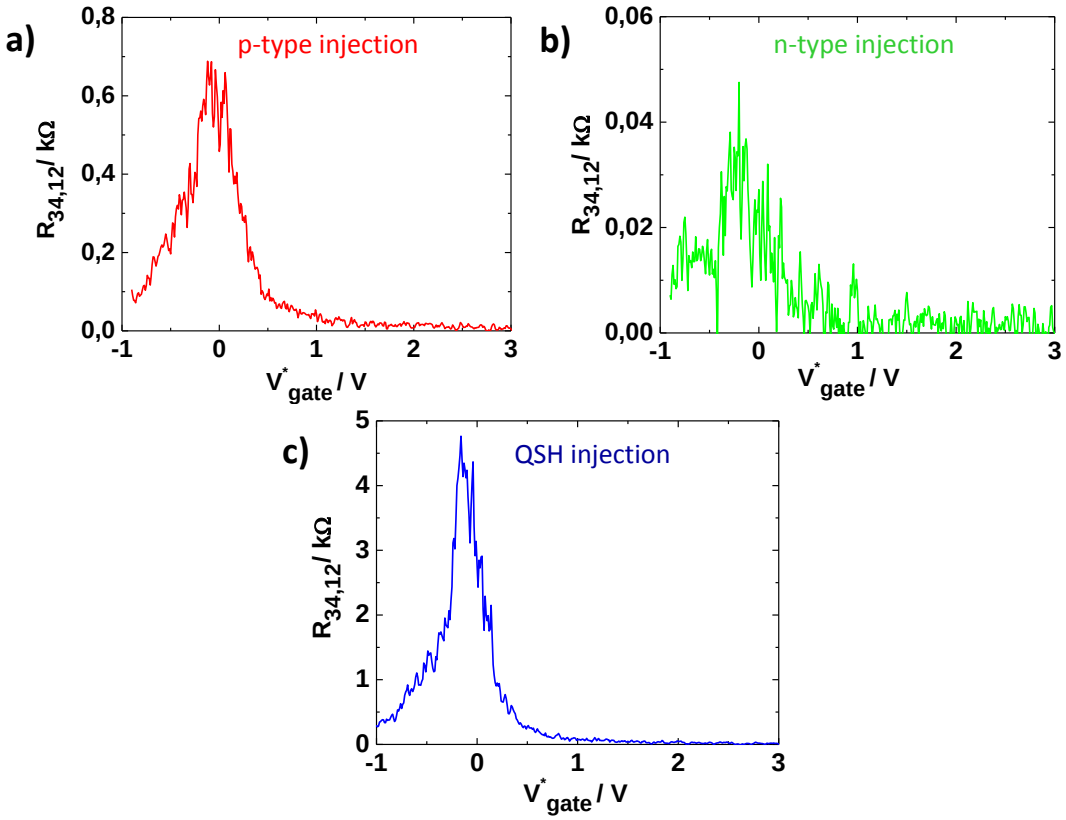

Figure 2.15: Non-local resistance data for measurement configuration 1. Current is applied on the lower leg while the non-local voltage is measured on the upper leg. Panel a) shows the signal for a p-type lower leg. In b) the lower leg is n-conducting while c) corresponds to a Fermi level inside the band gap.

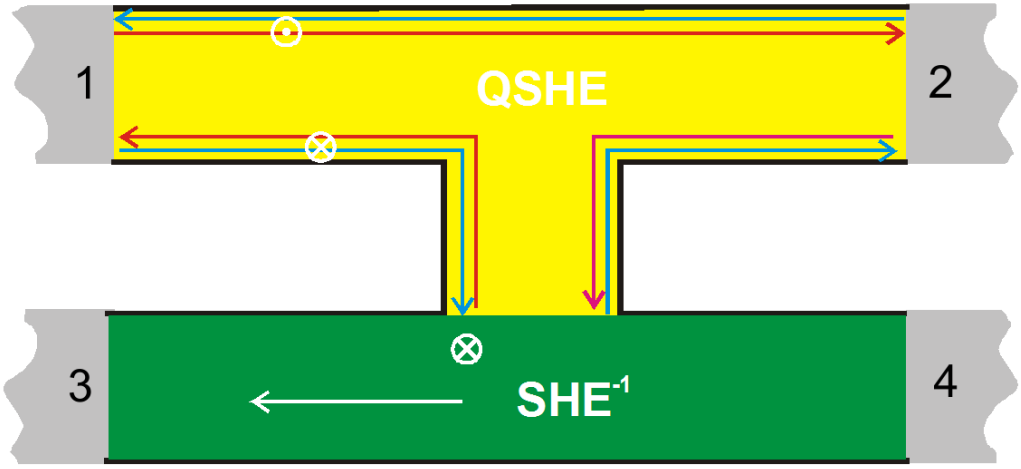

Figure 2.16: Concept for using the quantum spin Hall state as spin injector. If a current is injected in the upper leg the spin polarized edge states will induce a spin current in the lower leg. This spin current will be transformed into a non-local voltage by the inverse spin Hall effect.

As a further test we can measure the non-local signals that develop when both injection and detection happen in the quantum spin Hall regime. The result is shown in panel c). Since this measurement configuration is similar to the non-local resistance measurements presented in the previous section one would expect to observe a strong non-local resistance in this measurement as a signature of edge channel transport in the whole sample. As can be seen in panel c) this is indeed the case and the non-local resistance reaches values of several kiloohms. This value is slightly lower than the value one would expect for perfect quantization, which is not surprising due to the use of two separate gates in this experiment. In the region between the two gates (see also 2.13) the gating effect will be weak and metallic puddles can form. These will act as dephasing centers and lead to additional backscattering as described in the previous section.

The second experimental approach focuses on using the quantum spin Hall channels to inject a spin polarized current. A schematic layout for this experiment is shown in figure 2.16. Here the current is applied in the upper leg between the contacts 1 and 2 and the edge channels will inject a spin polarized current into the lower leg. This spin polarized current will lead to a different chemical potential for spin up and spin down electrons. The spin polarized current will lead to a voltage difference between contacts 3 and 4 due to the inverse spin Hall effect [50]. Due to the Onsager-Casimir symmetry relations for non-local resistances this setup should yield similar results to the first approach [43, 55]. The Onsager-Casimir symmetry relation for a four-terminal device is

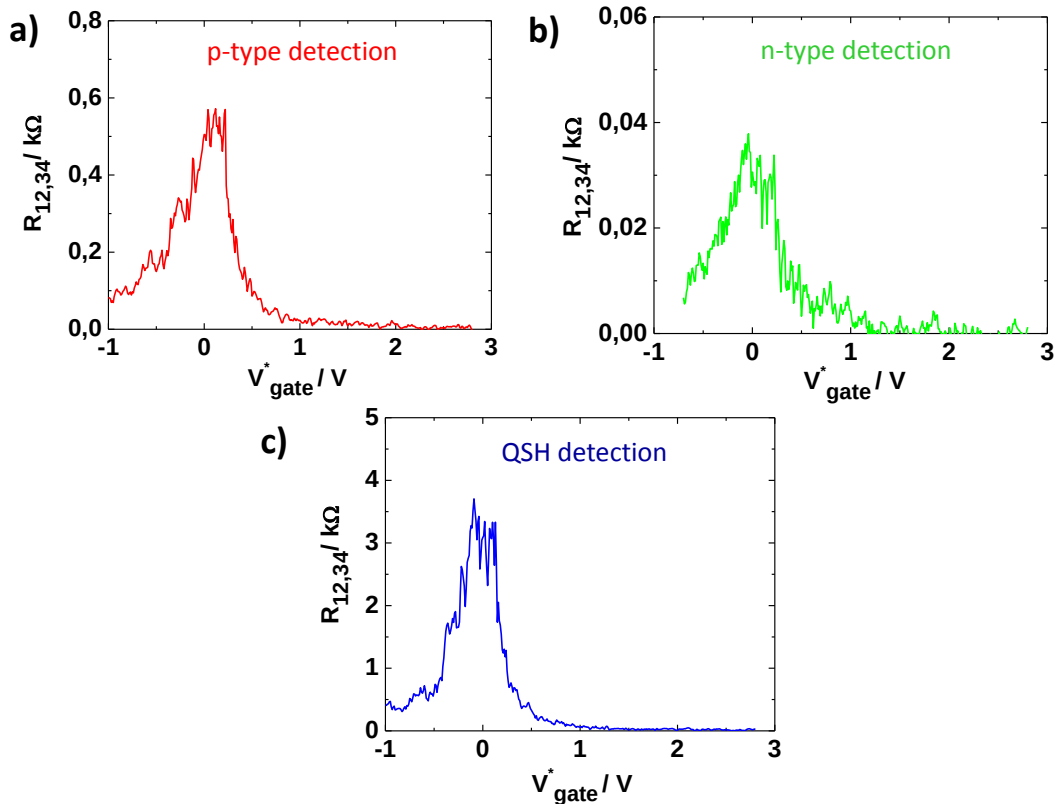

Figure 2.17: Non-local resistance data for measurement configuration 1. Current is applied on the upper leg while the non-local voltage is measured on the lower leg. Panel a) shows the signal for a p-type lower leg. In b) the lower leg is n-conducting while c) corresponds to a Fermi level inside the band gap.

$$R_{mn,kl}(\mathbf{B}) = R_{kl,mn}(-\mathbf{B}). \tag{2.4}$$

Current probes are denoted by mn and voltage probes by kl while B refers to the applied magnetic field. Since the magnetic field is zero in our experiment we expect $R_{34,12} = R_{12,34}$.

In the experiment we apply the gate voltages in the same way as before. This means we can now modify the injection properties by scanning the upper gate voltage while the detection of non-local signals happens with a fixed gate voltage on the lower gate. The results for this setup are shown in figure 2.17. Panel a) and panel b) show the results for p-type and n-type detection, respectively. The non-local response for detection using the quantum spin Hall state is displayed in panel c).

As expected we obtain results that resemble the observations in the first experimental approach. We observe a maximum in the non-local resistance when the upper leg is tuned into the quantum spin Hall regime while the lower leg remains metallic. This observation serves as evidence for an injection of spin polarized electrons from the quantum spin Hall edge states which are detected in the lower leg via the inverse spin Hall effect. We again observe an order of magnitude larger non-local signal when the lower leg is tuned into the p-conducting regime compared to the n-conducting case. Additionally, when the lower leg is tuned into the quantum spin Hall regime we can again observe the largest non-local resistance signals since we reach the fully edge state dominated transport.

In summary these two experiments show that transport in the quantum spin Hall states is indeed spin polarized. This provides the last missing experimental evidence that the picture of the quantum spin Hall state as counterpropagating spin polarized edge channels is correct.

Further information on the detection of the spin polarization of the quantum spin Hall state can be found in chapter 5.

2.5 Conclusion

This chapter has focused on the experimental verification of the quantum spin Hall effect in two dimensional topological insulators and its properties. We use HgTe quantum wells as a model system for a two dimensional topological insulator. In this system the band inversion of the Γ_6 and Γ_8 states leads to a topologically non trivial band structure. Transport studies on these quantum well structures give experimental evidence for the existence of the quantum spin Hall effect. Furthermore non-local transport experiments confirm that the quantum spin Hall state consists out of two counterpropagating oppositely spin polarized edge states.

Chapter 3

HgTe as a 3-dimensional topological insulator

3.1 Strained bulk HgTe

Bulk HgTe has a topologically non-trivial bandstructure due to the inversion of the Γ_8 and the Γ_6 bands but it is a zero gap material with the Γ_8 light hole and heavy hole bands touching at the Γ point and forming the conduction and valence bands, respectively (see figure 2.2). This degeneracy between the Γ_8 bands has to be lifted to observe topological insulator behavior in HgTe. This can be achieved by lowering the crystals symmetry for example by applying strain to the lattice [32, 40]. Experimentally this can be accomplished by growing a HgTe layer on a lattice mismatched substrate. A band gap will open if the strain is tensile, while compressive strain leads to an increased overlap of the Γ_8 bands. Therefore, our material of choice for the substrate is CdTe since it has a slightly larger lattice constant than HgTe ($a_{CdTe} = 0.6482\,\text{nm}$; $a_{HgTe} = 0.6462\,\text{nm}$ [56]). This relatively small difference in lattice constant enables the growth of fully strained HgTe layers with a critical thickness of approximately 200 nm where relaxation starts to set in. Thus 3-dimensional topological insulator behavior should be observable in such layers. However, the band gap is relatively small, theoretical calculations estimate a band gap size of $22\,\text{meV}$ for the HgTe/CdTe system [35].

In order to verify the occurrence of topological surface states in MBE grown bulk HgTe, angle resolved photo emission spectroscopy studies were carried out on a $1\,\mu\text{m}$ thick HgTe

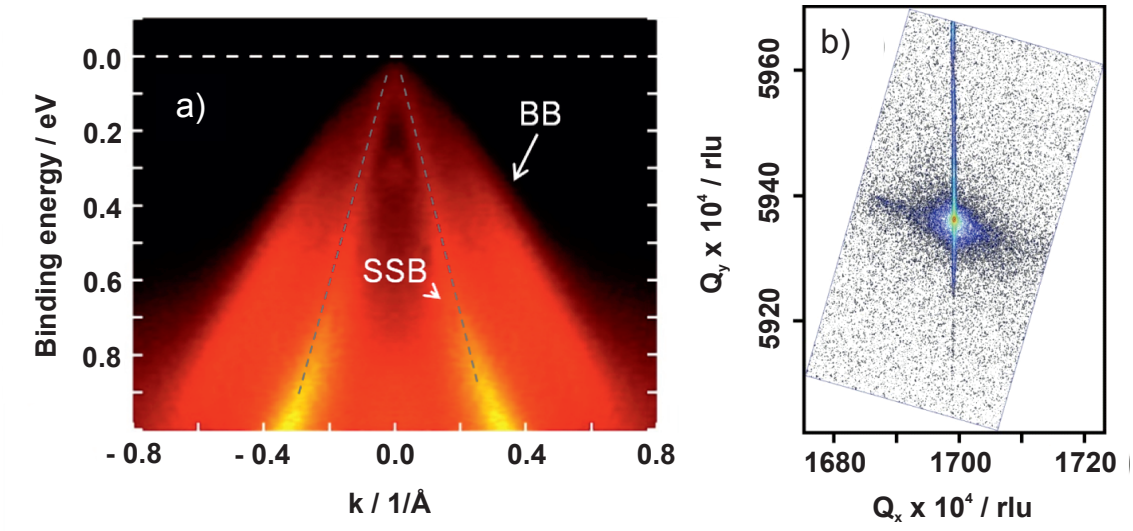

Figure 3.1: a) angle resolved photo electron spectroscopy picture of the band structure in a 1 µm thick bulk HgTe layer. BB denounces the bulk band while SSB and the gray dotted lines show the position of the surface state bands. The position of the Fermi energy is marked by the dotted white line. b) reciprocal space map around the [115] reflex of the measured HgTe layer.

layer [35]. Figure 3.1 a) shows the resulting spectrum. The main visible feature is the bulk valence band in bright red labeled BB. Overlaying the valence band one can see the linear dispersing surface state bands merging into the yellow features deep in the valence band (SSB). Another noteworthy result of these measurements is the position of the Fermi energy, which appears on top of or directly above the valence band. This means that these MBE grown HgTe layers feature a very low carrier concentration of bulk carriers in contrast to the results that are found in the Bi based materials (see chapter 1).

The first investigations on thinner strained bulk HgTe 3-dimensional topological insulator samples were carried out on a 70 nm thick HgTe layer grown directly on a [001] oriented CdTe substrate [35]. To establish the strain in this layer it was studied via high resolution x-ray diffraction. Figure 3.1 b) shows a reciprocal space map of the sample around the [115] reflex. The [115] reflex of the CdTe substrate is visible in the center of the graph. The thin vertical line in the upper part of the graph originates from the HgTe layer. Both features exhibit the same reciprocal lattice vector $\mathbf{Q}_x$ thus confirming that the HgTe layer is grown fully strained, retaining the lattice constant of CdTe.

In order to perform transport experiments on this layer, a Hallbar, with a width of 200 µm and a length between contacts of 600 µm, was patterned using optical lithography. The

magnetotransport measurements were carried out in a ^{3}He/^{4}He-dilution refrigerator system at 50 mK and magnetic fields up to 16 T. The magnetic field was aligned perpendicular to the plane of the Hallbar, consequently top and bottom surface of the Hallbar are both perpendicular to the magnetic field, while the side surfaces are parallel.

The transport results of a standard Hall measurement on the sample are shown in figure 3.2. From the low field data one can extract the following values for the electron density

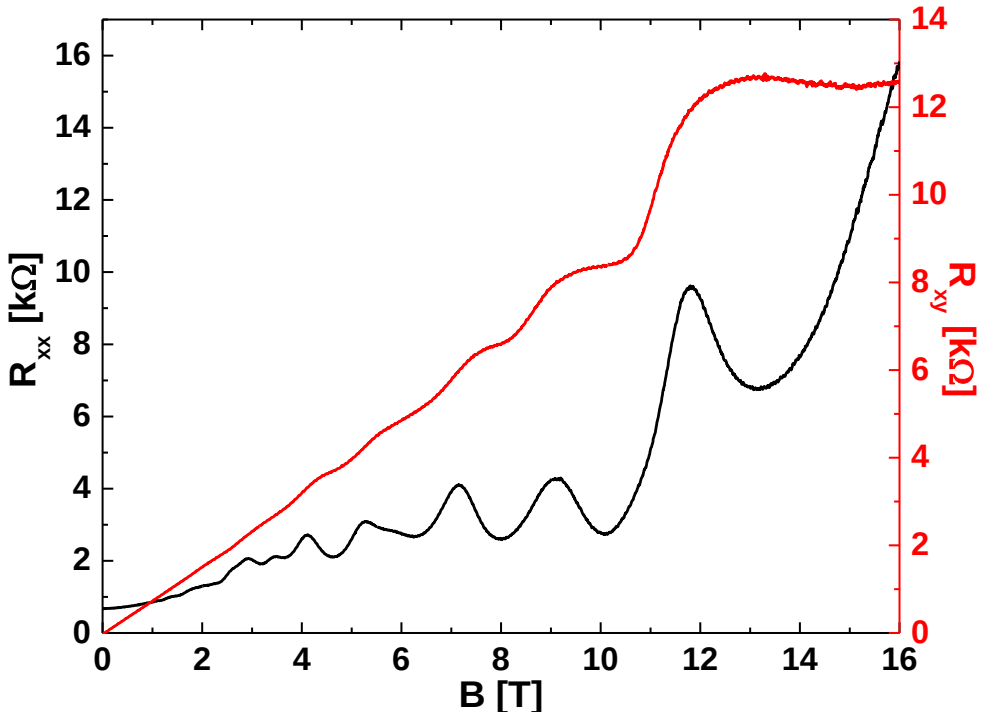

Figure 3.2: Hall measurements of a 70 nm thick strained bulk HgTe layer measured at 50 mK. The longitudinal resistance R_{xx} is plotted in black and the Hall resistance R_{xy} in red.

and mobility in the sample: $8.5 \times 10^{11}\,\mathrm{cm}^{-2}$ and $34\,000\,\mathrm{cm}^2\,\mathrm{V}^{-1}\,\mathrm{s}^{-1}$. This mobility is significantly higher than the mobilities observed in the Bi-based systems [57, 58]. Interestingly, the longitudinal resistance data show clear Shubnikov-de Haas oscillations while the Hall measurements exhibit quantum Hall plateaus at higher magnetic fields, a characteristic signature for transport in a 2-dimensional electron gas. This is surprising since the confinement energies in a 70 nm thick HgTe layer should be small and thus the energetic distance between subands. This should lead to a suppression of the quantum Hall effect due to multisubband averaging. Another possible source of the quantum Hall effect in this system is the 2-dimensional topological surface state. As mentioned above, top and

bottom surface are perpendicular to the applied magnetic field and thus are expected to show the quantum Hall effect. Indeed, upon closer inspection, the observed quantum Hall effect shows an unusual plateau sequence pointing to a linear Dirac like dispersion. At lower fields one can observe only plateaus with odd filling factors of ν = 9, 7, 5 while at higher fields odd and even filling factors of 4, 3, 2 are resolved. This behavior can be seen easier when looking at the Hall conductivity which is plotted in figure 3.3. The quantum

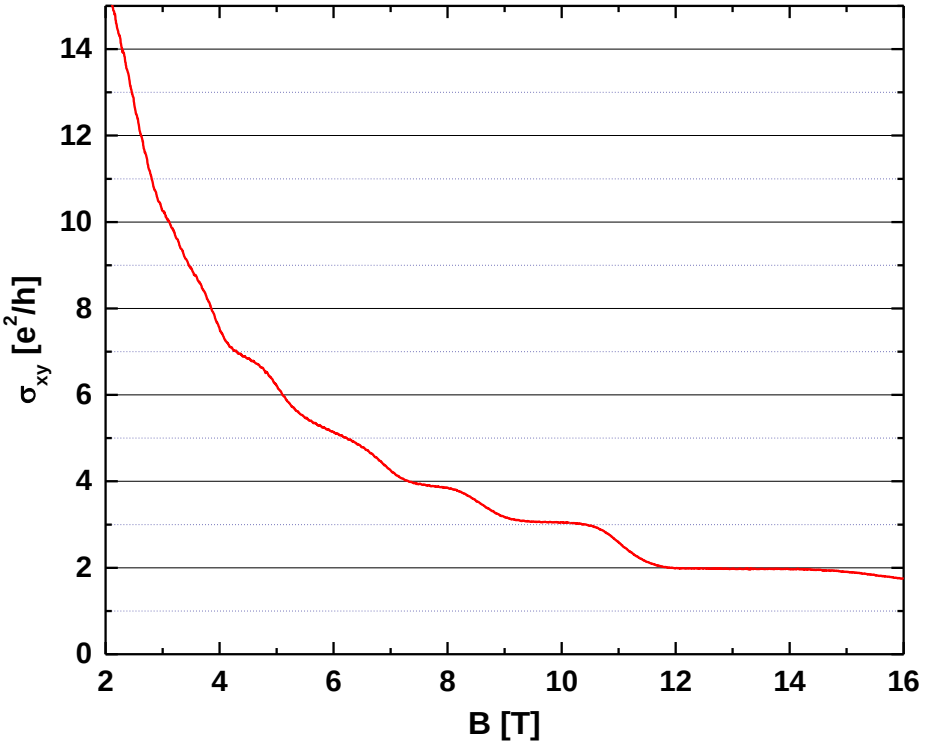

Figure 3.3: Hall conductivity of the strained bulk HgTe layer.

Hall conductivity in Dirac systems is given by

$$\sigma_{xy} = m\left(n + \frac{1}{2}\right)\frac{e^2}{h}, \tag{3.1}$$

where m is the number of degenerate Dirac cones in the system, n the Landau level index, e the electron charge and h Planks constant [32, 59]. Compared to conventional systems, this shifted Hall sequence originates from the occurrence of a Landau level at zero energy in Dirac systems [17]. The odd integer sequence observed at low fields therefore corresponds to the quantum Hall effect of a system of two degenerate Dirac cones. This is expected in a 3-dimensional topological insulator since only two surfaces (top and bottom) are subjected to a perpendicular magnetic field. The appearance of additional even

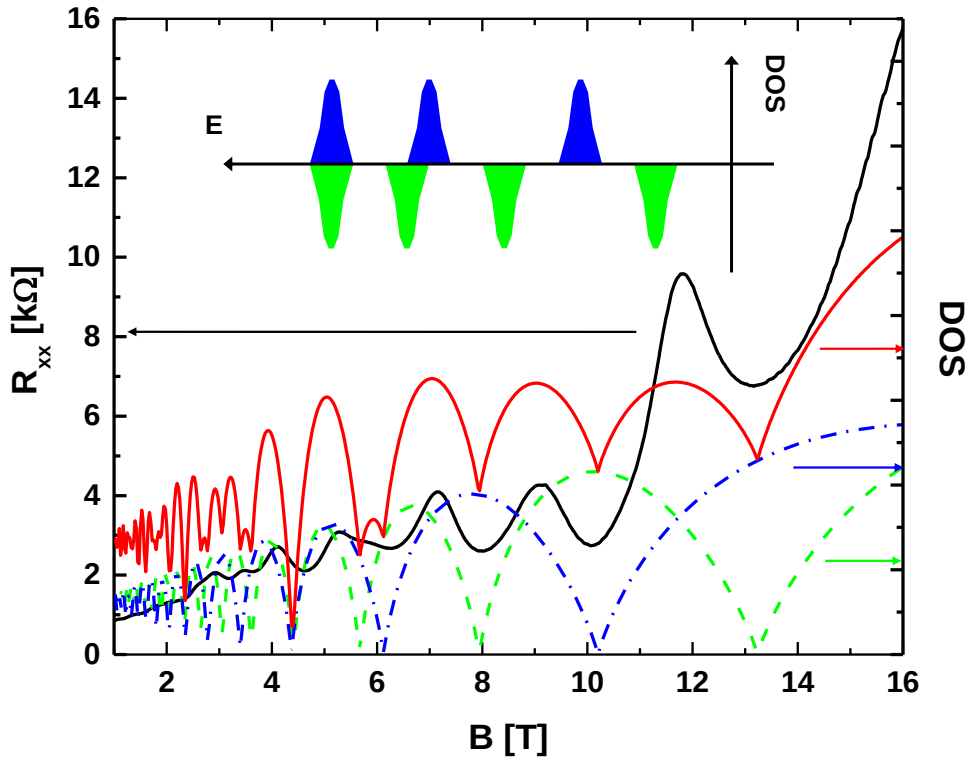

Figure 3.4: Calculated density of states (DOS) compared to the measured Shubnikov-de Haas oscillations (black curve). The DOS is calculated under the assumption of two Dirac cones with carrier densities of 3.7×10^{11} cm^{-2} (for the surface at the CdTe substrate - shown in blue) and 4.8×10^{11} cm^{-2} (surface to vacuum - green curve) The sum of both DOS is shown in red. The inset shows a schematic of the Landau level ladders for both surfaces.

integer Hall plateaus at higher magnetic fields, however, does not fit the simple explanation of two completely degenerate systems. This can be understood when the sample structure is taken into account: Top and bottom surface are not subjected to the same electrostatic environment. While the lower surface is connected to the CdTe substrate the upper is connected to vacuum. This difference in electrostatics will also lead to a different electron density on both surfaces and thereby lift the degeneracy. For the quantum Hall measurements this lifted degeneracy shows up only at higher magnetic fields when the energy splitting between adjacent Landau levels becomes large enough to resolve them individually. This is depicted schematically in the inset of figure 3.4. For a more quantitative assessment of the situation, density of state calculations were performed assuming two Dirac cones with slightly different densities of 3.7×10^{11} cm^{-2} and 4.8×10^{11} cm^{-2} for the CdTe-HgTe interface and the HgTe-vacuum interface, respectively. The sum of the

density of states from both surfaces can then be compared with the measured Shubnikov-de Haas oscillations. The resulting calculated density of states is in good agreement with the data as can be seen from figure 3.4.

Another interesting aspect in the measured data is the non-vanishing longitudinal resistance at higher magnetic fields. Conventionally quantum Hall plateaus are accompanied by a longitudinal resistance approaching zero especially at high magnetic fields when the energetic gap between Landau levels exceeds the cyclotron energy. Here however, e.g. the well formed $i = 2$ plateau around $14\,\mathrm{T}$ is accompanied only by a high resistive minimum in the Shubnikov-de Haas oscillations. This indicates the existence of additional channels contributing to the longitudinal transport. A possible source for these additional channels can be found in the side surfaces of the system [60]. The side surfaces will not be gapped by the applied magnetic field since they are aligned in parallel to the field. Thus they can coexist with the edge states of the top and bottom surface and provide a backscattering possibility.

A more detailed description of the experimental findings and especially the theoretical modeling can be found in chapter 6 and Ref. [35].

3.2 Transport in gated samples

In order to further address the aspect of the different electrostatic environments on both surfaces, a sample with a top gate was fabricated. The sample is again a Hallbar sample with $L \times W$ = $600\,\mu\mathrm{m} \times 200\,\mu\mathrm{m}$, the Au top gate is insulated from the Hallbar with a $110\,\mathrm{nm}$ SiO_2/Si_3N_4 multilayer structure. A picture of the gated Hallbar structure is shown in figure 3.5.

The longitudinal and Hall resistances are measured for gate voltages (V_g) between $-5\,\mathrm{V}$ and $5\,\mathrm{V}$ in steps of $0.5\,\mathrm{V}$. For gate voltages between $-1\,\mathrm{V}$ and $5\,\mathrm{V}$, the sample is n-conducting and shows well developed quantum Hall plateaus and corresponding Shubnikov-de Haas oscillations. Below $-1\,\mathrm{V}$ p-conductance starts to set in and the quantum Hall plateaus weaken. The following analysis therefore focuses on the n-conducting region. The Hall traces for the different gate voltages are shown in figure 3.6 a) and the corresponding Shubnikov-de Haas measurements can be found in figure 3.6 b). The measurements for a gate voltage of $5\,\mathrm{V}$ are plotted as the lowest dark blue trace. The carrier density extracted from the low field Hall data varies from $3.5 \times 10^{11}\,\mathrm{cm}^{-2}$ at $V_g = -1\,\mathrm{V}$

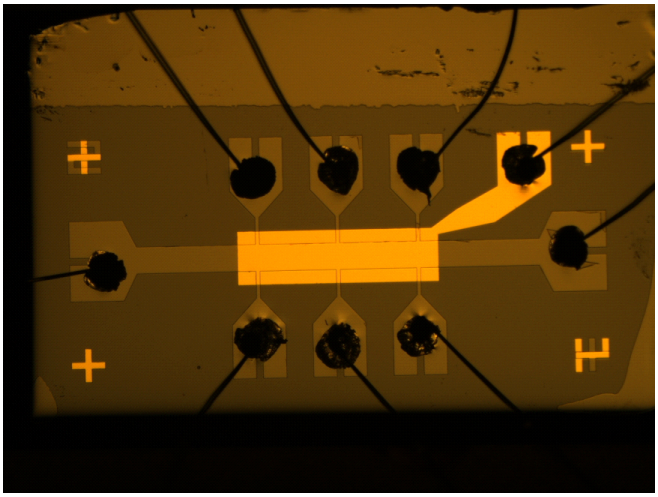

Figure 3.5: Micrograph of the used gated Hallbar sample.

to $2.0 \times 10^{12}\,\mathrm{cm}^{-2}$ at $V_g = 5\,\mathrm{V}$. Well pronounced quantum Hall plateaus and Shubnikov-de Hass oscillations are visible over the entire gate voltage range with predominantly odd quantum Hall plateaus visible at low magnetic fields (similar to the behavior of the ungated sample). The robustness of the quantum Hall state even up to such high carrier densities (for a 2-dimensional electron gas) of $2.0 \times 10^{12}\,\mathrm{cm}^{-2}$ is a surprising find. Lowering the gate voltage leads to a decreased carrier density in the system (visible by the increased Hall slopes and the expected behavior for an n-conducting system). At $0\,\mathrm{V}$ gate voltage [single trace also shown in figure 3.7 c)] the magnetotransport results are comparable with the observations on the ungated sample: At low fields only odd sequenced quantum Hall plateaus are resolved while the $i = 2$ plateau is visible at high fields. This data can again be fitted under the assumption of two slightly degenerate Dirac cones as presented in the previous section for the ungated sample. The result is shown in figure 3.7 d). For the lowest gate voltages, the Hall resistance reaches the $i = 1$ quantum Hall plateau, the $i = 2$ plateau first weakens at a gate voltage of $-0.5\,\mathrm{V}$ [figure 3.7 b)] - accompanied by a merging of the corresponding Shubnikov-de Haas peaks - and then vanishes completely for the $-1\,\mathrm{V}$ measurement [figure 3.7 a)]. This means that we observe an only odd sequenced quantum Hall effect at this gate voltage, the typical signature of a Dirac system with two degenerate Dirac cones. This observation further confirms that the observed quantum Hall effect indeed originates from the topological states in this system. Furthermore this result shows that it is possible to detune the electrostatic potential on both surfaces with respect to each other by the use of a top gate.

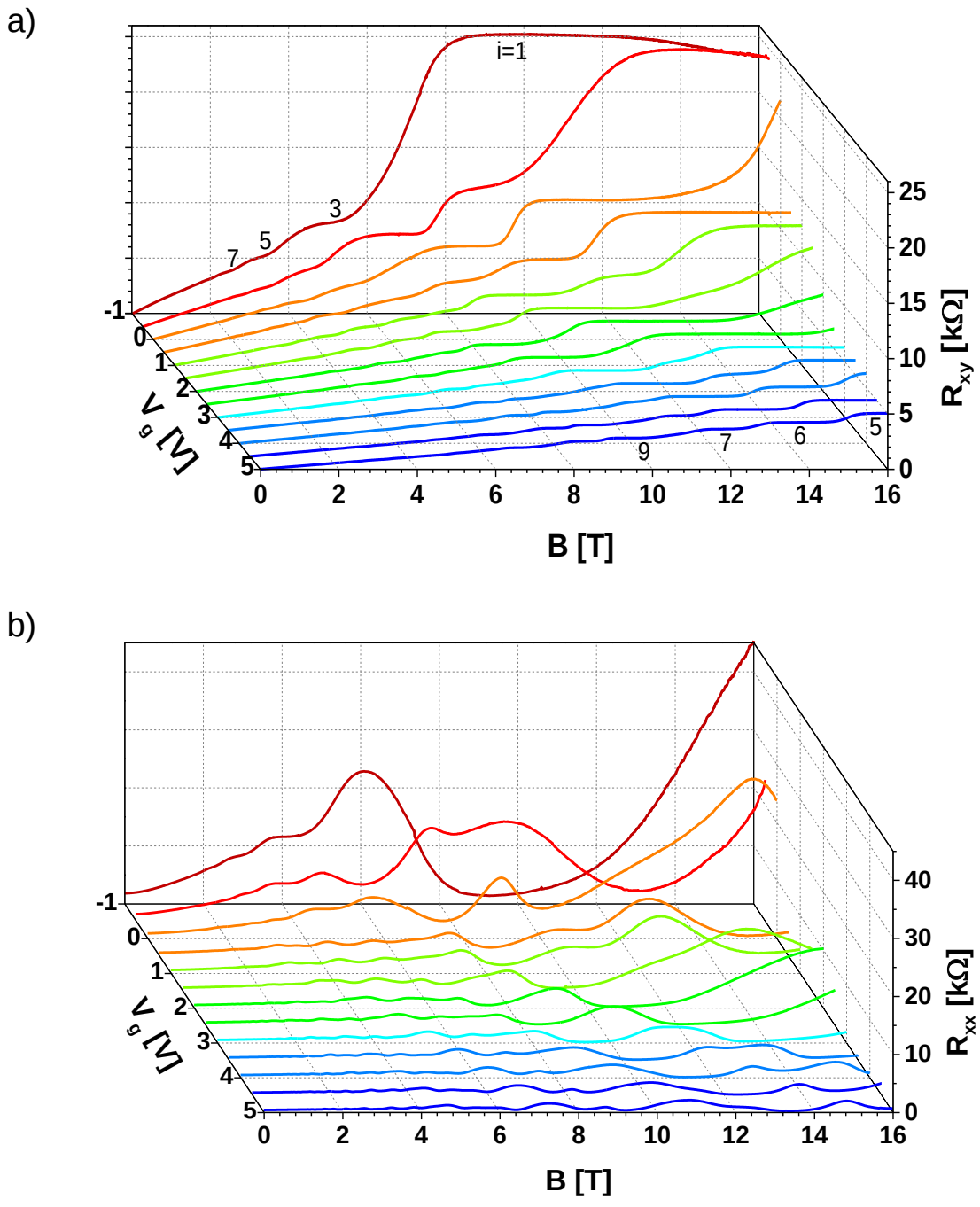

Figure 3.6: Gate dependent Hall a) and longitudinal b) resistance for the strained bulk HgTe layer. The gate voltage is changed from -1 V to 5 V in steps of 0.5 V. The lowest dark blue traces are for a gate voltage of 5 V.

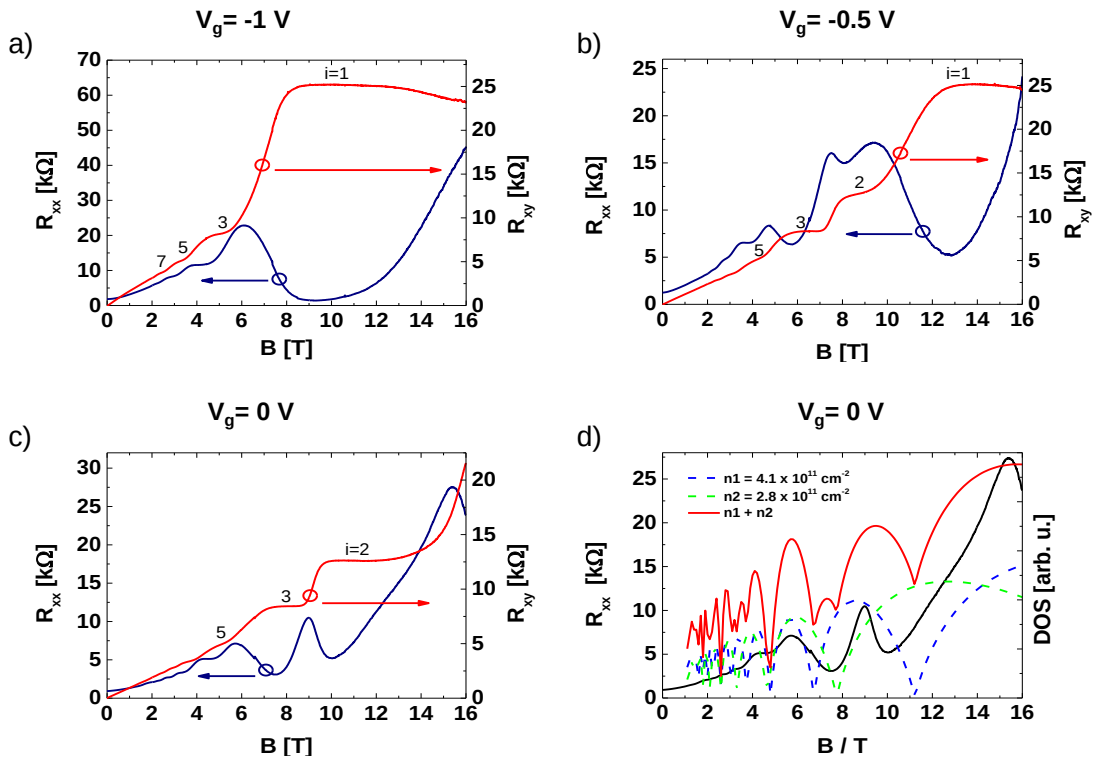

Figure 3.7: Detailed plots of the Hall and longitudinal resistance at the gate voltages of -1, -0.5 and 0 V in panel a), b) and c), respectively. Panel d) shows a fit to the 0 V data using a calculated density of states under the assumption of two Dirac cones at different carrier densities.

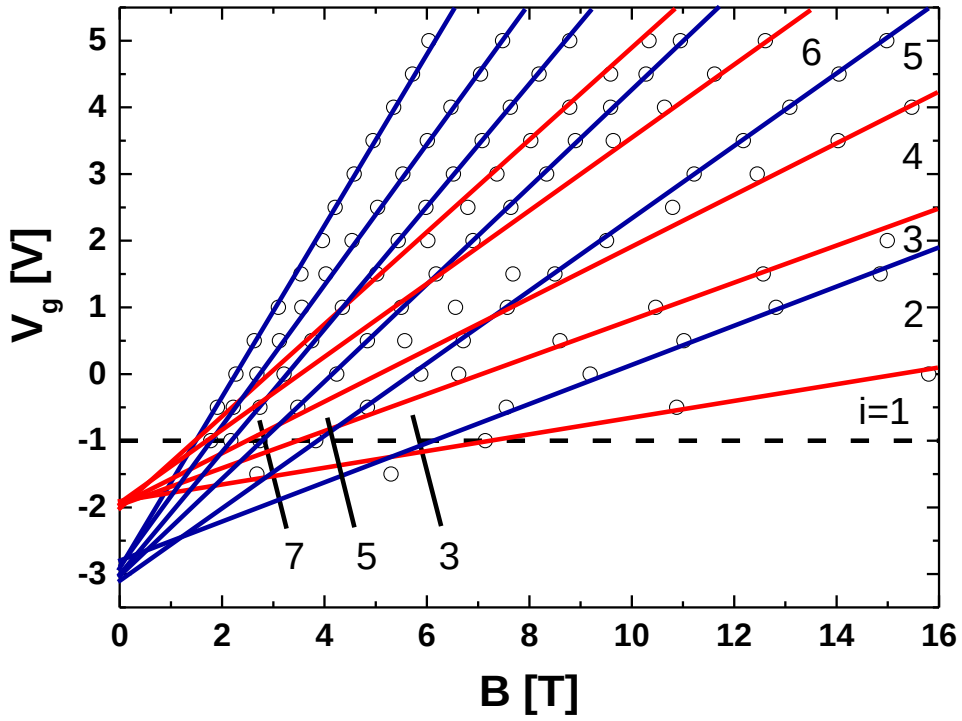

Figure 3.8: Landau level fan extracted from the Hall measurements. Circles mark the position of plateau transitions in the magnetotransport data, the red and blue lines indicate the positions of Landau levels originating from the top and bottom surface, respectively. The numbers mark regions in which the plateau i can be observed.

Detailed analysis of the data allows for the identification of contributions from top and bottom surface. These can be found most prominently by extracting a Landau level fan chart from the magnetotransport data. The positions where the Landau levels cross the Fermi energy can be obtained from the positions where the transition between plateaus occurs (for improved accuracy the readout was performed by numerically differentiating the Hall traces). The results are displayed in figure 3.8. The circles represent the positions on which Landau levels are found in the individual magnetic field sweeps using the method described above. The positions can be assigned to two separate Landau level fans with a different origin, marked by the red and blue lines in figure 3.8. The regions in between the levels correspond to the quantum Hall plateau positions, the numbers indicate which plateau i can be observed (e.g at $-1\,\mathrm{V}$ gate voltage the sequence of only odd plateau values $i = 7, 5, 3, 1$ can be found again). The individual fan charts that were observed have a nearly equidistant spacing at fixed magnetic fields. This rules out an additional Zeeman splitting, which is expected to be absent for the Dirac surface states of

a 3-dimensional topological insulator where each surface hosts only one spin direction. Furthermore one can observe a different slope of the Landau fans when comparing lines with the same Landau index. This means the two systems are influenced differently by the top gate since the change in carrier density per applied gate voltage defines the slope of the individual Landau levels. This can be well understood in the framework of Dirac surface states, since top and bottom surface reside at different distances from the top gate. Thus the upper surface (corresponding to the system responsible for the red fan chart) will be influenced stronger by the top gate than the lower surface (blue fan chart). Indications for individual contributions from top and bottom can also be found in the longitudinal resistance traces of figure 3.7 b) and c). Especially in the high field region one can see that neighboring Shubnikov-de Haas oscillations are differently broadened which again indicates that two 2-dimensional electron gasses are responsible for the observed pattern. The broader oscillations most likely originate from the top surface state. The interface between the gate insulator and the HgTe is expected to be rougher than the epitaxial interface between CdTe and HgTe, additionally the top surface will be prone to oxidization and influence from ionized dopants in the insulator. This identification of top and bottom surface contributions is also consistent with the one found in the Landau level fan chart. It is interesting to note that different mobilities on the two surfaces indicate that top and bottom surface state are not strongly coupled since this should lead to equal mobilities in both systems.

The observed results can be explained solely by transport through the Dirac surface states on top and bottom surface. This is a surprising find since one would expect the onset of bulk contributions especially for higher gate voltages/carrier densities due to the relatively small band gap in the system. The absence of bulk contributions can also be inferred from figure 3.9, here the deviations from the expected Hall plateau quantization are plotted. As one can see the deviations are constant over the complete gate voltage range which contradicts increased bulk conductivity. Bulk contributions should lead to parallel conductance channels which would result in lowered observed plateau values. This unexpected stability of the surface state transport is not fully understood and warrants future investigations.

A detailed overview of the data presented in this section is being prepared for publication [61].

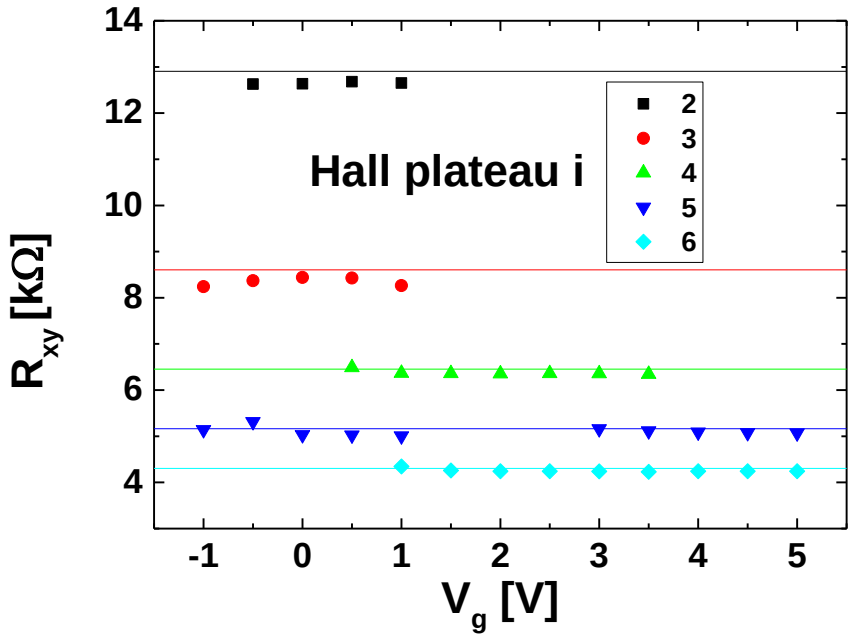

Figure 3.9: Deviations from the expected quantum Hall plateau value i depending on V_g

3.3 Conclusion

The presented findings establish strained bulk HgTe as a 3-dimensional topological insulator system. The high crystalline quality in HgTe compared to Bi-based materials allowed for the first observation of the quantum Hall effect originating from the surface states of a 3-dimensional topological insulator. A characteristic Dirac type quantum Hall effect is visible in these samples and measurements using a top gate allow for the identification of contributions from individual surfaces. Surprisingly, the surface state transport can be observed even at very high carrier densities unobstructed by bulk contributions. One possible explanation for this observation is that the gate influence is screened by the surface states very efficiently such that the Fermi energy in the bulk stays fixed inside the bulk band gap. Such an enhanced reduced gate influence on the bulk states would be possible if the dielectric constant ϵ of the layer would be very high (above 100) for the zero frequency limit. Another possibility to explain the observed behavior is a reduced interaction between bulk and surface states e.g. due to a large difference in carrier mobility in the two components (maybe paired with a low scattering possibility between surface and bulk due to e.g. small wavefunction overlap between the two). If the surface carriers

are highly mobile compared to bulk carriers, the current in the system could flow almost exclusively in the surface states and especially for relatively low bulk carrier densities only the surface states would be probed in transport experiments. In order to address this questions, future investigations will focus on improved growth of HgTe layers aiming for even higher carrier mobilities and well defined interface properties. A possible way to achieve this is to grow HgCdTe layers above and below the HgTe layer such that both surfaces are connected to a similar, well defined environment. Higher mobilities should also enable a closer inspection of the transport behavior in the p-conducting regime which should help to address the validity of the models that are discussed above. The implementation of a back gate to the structures could help to further strengthen the identification of contributions from the different surfaces. Similarly investigating the quantum Hall effect in tilted magnetic fields could answer some of the open questions.

Chapter 4

Evidence for the ballistic intrinsic spin Hall effect in HgTe nanostructures

This chapter is based on the publication: *C. Brüne, A. Roth, E. G. Novik, M. König, H. Buhmann, E. M. Hankiewicz, W. Hanke, J. Sinova and L.W. Molenkamp; 'Evidence for the ballistic intrinsic spin Hall effect in HgTe nanostructures', Nature Physics* ***6****, 448-454, 2010.*

4.1 Abstract

In the spin Hall effect, a current passed through a spin-orbit coupled electron gas induces a spin accumulation of inverse sign on either side of the sample. A number of possible mechanisms have been described, extrinsic as well as intrinsic ones, and they may occur in the ballistic as well as the diffusive transport regime. A central problem for experimentalists in studying the effect is the very small signals that result from the spin accumulation. Electrical measurements on metals have yielded reliable signatures of the spin Hall effect, but in semiconductors the spin accumulation could only be detected by optical techniques. Here we report experimental evidence for electrical manipulation and detection of the ballistic intrinsic spin Hall effect (ISHE) in semiconductors. We perform a non-local electrical measurement in nanoscale H-shaped structures built on high-mobility HgTe/(Hg,Cd)Te quantum wells. When the samples are tuned into the p-regime, we observe a large non-local resistance signal due to the ISHE, several orders of magnitude

larger than in metals. In the n-regime, where the spin-orbit splitting is reduced, the signal is at least one order of magnitude smaller and vanishes for narrower quantum wells. We verify our experimental observations by quantum transport calculations.

4.2 Introduction

Control, manipulation, and detection of spin polarized carriers are the focal goals of spintronics [62]. The creation of new technologies based on spin current manipulation requires new methods and materials for generating and controlling spin-based properties of active devices. Although progress has been made in spin injection from a ferromagnetic metal into a semiconductor through tunnel barriers, its detection efficiency is still problematic. Applications of ferromagnetic semiconductors are challenged by their ferromagnetic transition temperatures which remain below room temperature. A clear avenue to circumvent several of these key problems is the direct use of electric fields to manipulate electron spins through spin-orbit coupling based effects in paramagnetic systems. Of this class of effects one of the premier candidates at present is the spin-Hall effect (SHE) [46, 47, 63, 64, 65, 49] in which a transverse spin accumulation is created when an electric current is passed through a material with strong spin-orbit coupling, coming either from the band structure (intrinsic spin-Hall effect, ISHE) or from the scattering of electrons on heavy impurities (extrinsic spin-Hall effect, ESHE). Although the SHE has been very actively studied theoretically over the past few years [64], few experimental results have been reported because of the difficulty of detecting the effect. Early experiments demonstrating the effect utilized sensitive optical techniques [66, 67, 68]. Electrical detection of the SHE, although much more desirable from the device point of view, is even more challenging and has been demonstrated only in metallic nanostructures [69, 70, 71, 72, 73]. The detected signals are weak, to a large extent because are in the diffusive transport regime. Whereas most of the above experiments appear to result from the ESHE, Refs. [67] and [73] have attributed their observations the ISHE, involving the actual band structure spin-orbit coupling effects. A larger effect can be expected in samples where the transport is ballistic and the effect unequivocally stems then from the ISHE [50, 51]. Such an experiment is the topic of this paper: we provide experimental evidence for the electrical detection of the ballistic ISHE in high mobility HgTe-based nanostructures.

4.3 Sample layout and experiment

HgTe is a zero gap semiconductor which forms a type-III QW with $Hg_{0.3}Cd_{0.7}Te$ barriers that have an inverted band structure when the well width is larger than 6.3 nm [8] and a normal band structure for narrower widths. The two-dimensional electron gas (2DEG) in these structures exhibits a high carrier mobility and a large, gate-controllable, Rashba-type spin-orbit splitting [48, 74].

The three samples studied in this paper were chosen to represent various regimes of Rashba splitting: we study QWs with an inverted band structure (8.0 nm wide), in which the spin-orbit splitting is very large as a resultof the extensive mixing of the valence and conduction bands [39], these are Q2197 and Q2198. In the former, the structure contains donor-doped barrier layers on both sides of the QW, resulting in a smaller electric field across the well at zero gate voltage, and thus a smaller Rashba splitting than in Q2198, where the QW is asymmetrically doped. Additionally, we study a narrow (5.7 nm width, asymmetrically doped) sample, Q2398, which has a normal band structure, leading to a much reduced spin-orbit splitting, especially in the conduction band. At zero gate voltage , we find mean carrier mobilities of $\mu = 2.5,\ 1.2$, and 1.3×10^5 cm^2/Vs), and carrier densities $n_s = 1.7,\ 2.0$, and 5.5×10^{11} cm^{-2} for samples Q2197, Q2198, and Q2398, respectively.

To electrically detect the ISHE, we have fabricated H-shaped mesa structures (see Fig. 4.1) using electron beam lithography and dry-etching techniques, following a design proposed previously by some of us in Ref. [50]. A Au/Ti electrode is deposited on top of a 110-nm-thick SiO/SiN gate insulator layer that covers the entire sample. Ohmic contacts are fabricated by thermal In-bonding. Two additional leads have been added to the H-structures to allow further characterization measurements. These leads are attached to a vertical leg either far away from (e.g. sample Q2197, Fig. 4.1 (a)) or in close proximity to the horizontal leg of the H-bar (e.g. sample Q2198, Fig. 4.1 (b)). The H-structures consist of legs 1 μm long and 200 nm wide, with the connecting part being 200 nm wide and 200 nm long. The estimated mean free path in these systems is $l \geq 2.5\ \mu\mathrm{m}$ which establishes that the samples studied are well within the quasi-ballistic regime.

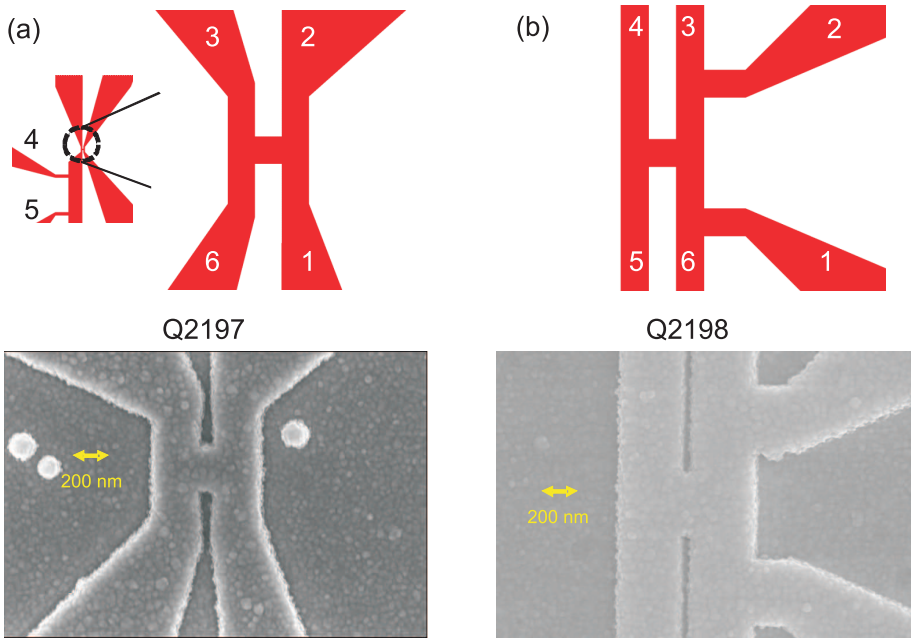

Figure 4.1: Sample layout and electron beam micrograph of samples (a) Q2197 and (b) Q2198.

4.4 Transport experiments on H-bar structures

The idea behind the transport measurements is as follows [50]. When an electric current flows in one of the legs of the H-bar structure [say between contacts 1 and 2 in 4.1 (a)], a transverse spin current due to the intrinsic spin-Hall effect is induced in the connecting part. Subsequently, this spin current produces, owing to the inverse spin-Hall effect [75], a non-local voltage difference in the opposite leg of the H-bar structure (in our example, between contacts 3 and 6 in Fig. 4.1 (a)) which can be measured by a voltmeter [47, 50]. Sweeping the gate voltage in the sample now allows us to vary the strength of the Rashba spin-orbit splitting by a variation of both the electrical field across the QW, as well as the Fermi level in the QW; this evidently results in a strong modulation of the non-local voltage, which can be analyzed by comparison with theory. The H-shape of the structure strongly suppresses any residual voltage between contacts 3 and 6 resulting from spreading of the potential difference applied between contacts 1 and 2. As an upper limit of the stray signal, we have computed the spreading voltage by solving Poisson's equation for the parameters of each sample (note that this implies assuming diffusive transport, as quasi-ballistic transport spreading effects are much smaller). Below we plot this residual voltage alongside the experimental non-local voltage to emphasize that the observed effect is solely due to the SHE. Experimentally, all measurements were performed using

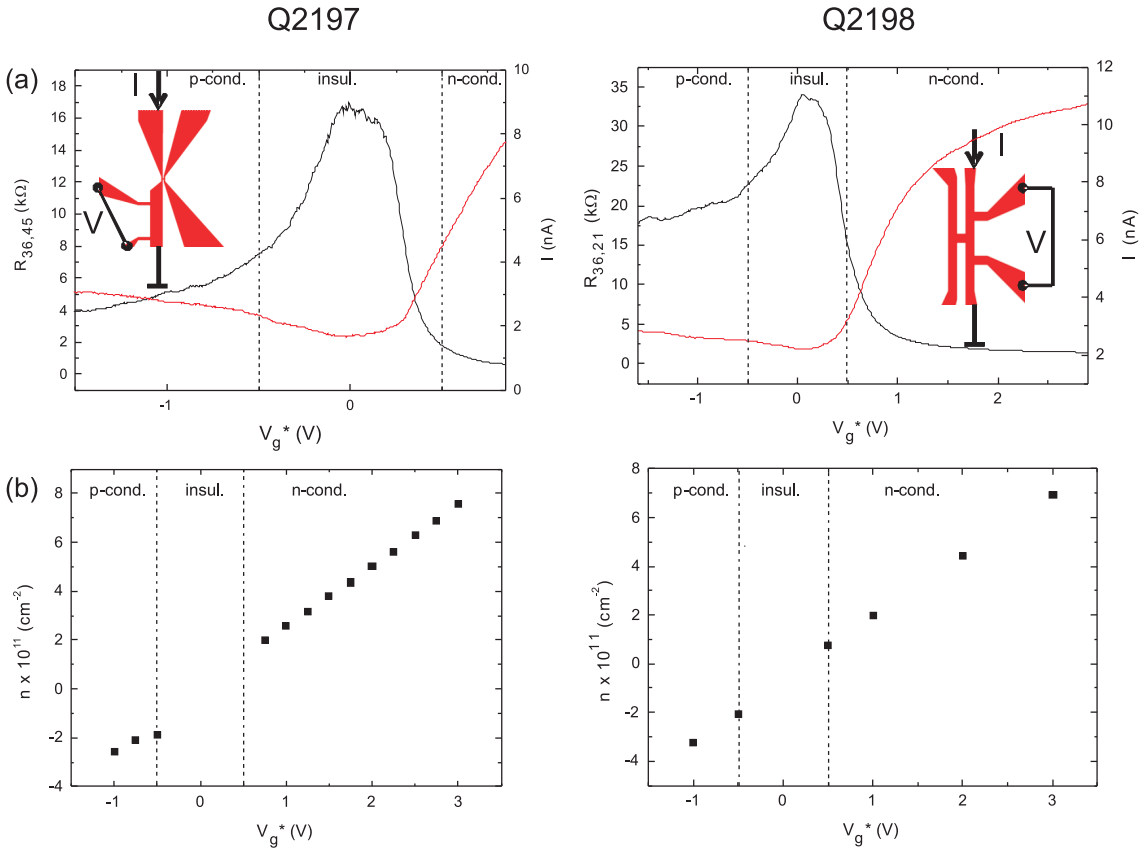

Figure 4.2: Local resistance data and carrier density of samples Q2197 and Q2198. (a) Resistance data (in black) in measurement configurations on one leg of the H-bar show signatures of the QSHE ; the red curves give the current through the samples. (b) Dependence of the carrier density on the applied gate-voltage. The contact configurations used here are indicated in the insets.

standard AC lock-in techniques under a voltage bias (we apply 100 μV across the sample and a reference resistor of similar resistance), at a sample temperature of 1.8 K.

Fig. 4.2 (a) shows the gate voltage dependence of the sample current (red traces) and the longitudinal resistance (black traces) of samples Q2197 and Q2198 ($R_{ij,kl}$ denotes a resistance calculated from the voltage measured between ohmic contacts k and l while passing a current between contacts i and j). For reasons of comparison, we shift the gate voltage axis such that renormalized gate voltage $V_g^* = 0$ V corresponds to the situation where the bulk Fermi level is in the center of the energy gap (the actual voltages where V_g^* = 0 V are $V_g \approx -1.0$ (-0.7) V for Q2197 (Q2198), respectively). Fig. 4.2 (b) shows the carrier density as a function of the renormalized gate voltage. This data was obtained through Hall-measurements on large Hall-bars fabricated from the same wafer and demonstrates that we can vary the carrier concentration enough to tune the sample

from strongly n-type ($n \approx 8 \times 10^{11}$ cm^{-2}), through the gap, down to a p-type regime at $V_g^* = -1$ V ($p \approx 3 \times 10^{11}$ cm^{-2}). For V_g^* between -0.5 V and 0.5 V the samples are insulating.

We recently showed [8] that the inverted band structure in HgTe quantum wells wider than 6.3 nm gives rise to the occurrence of the quantum spin Hall effect (QSHE), a novel type of quantum Hall effect that occurs at zero magnetic field, when the bulk of the sample is in the insulating regime. In samples that are smaller than the inelastic scattering length, the electrical conductance is then quantized at $2e^2/h$. Both the current and the resistance data on Q2197 and Q2198 [see Fig. 4.2 (a)] show indeed a resistance of the same order of magnitude as the conductance quantum when the gate voltage tunes the sample into the insulating regime ($-0.5\mathrm{V} < \mathrm{V_g^*} < 0.5$ V). As in the quantum Hall effect, QSHE quantization is caused by the formation of one-dimensional edge channels. The non-local character of carrier transport through these edge channels implies that the effect, which is much stronger than the signal anticipated for the ISHE in the insulating regime of our samples, should also show up in our H-bar geometry. We have indeed observed very strong non-local QSHE signals in the course of our experiments on (larger) H-bars, and an extensive report of these results is published elsewhere [25].

For our present objective of observing the ISHE, however, the QSHE is an unwanted effect in samples Q2197 and Q2198 as it tends to swamp the ISHE signal - despite the fact it shows its maximum at a different gate voltage. The experiments shown in Figs. 4.3 represent two different approaches to suppress the non-local QSHE signal. One approach is to make the devices sufficiently small so as to provoke backscattering of the QSHE edge channels. Zhou et al. recently showed theoretically [53] that QSHE backscattering occurs when the wave functions for opposite spin channels overlap, and estimate that this happens for a device width of around 200-250 nm. This is the reason we report here on very narrow (lateral) devices as well as (see below) a narrow quantum well device. The second method to suppress the QSHE is to choose a non-local configuration that implies edge channel transport over distances (much) longer than the inelastic length (which typically is a few micrometers [8]). This is why we have fabricated the additional leads in the Q2198 H-bar: in the QSHE regime, the extra leads to the mesa force the edge channels to take a detour of some 10 μm to ohmic contacts 3 and 6 [indicated by crosses in the insets of Fig. 4.3 (b)] before entering the detector contacts. An additional benefit is that the extra ohmic contacts cause equilibration of QSHE edge channels. Note that the ISHE signal is not affected by either of these mechanisms - actually, the close proximity of contacts

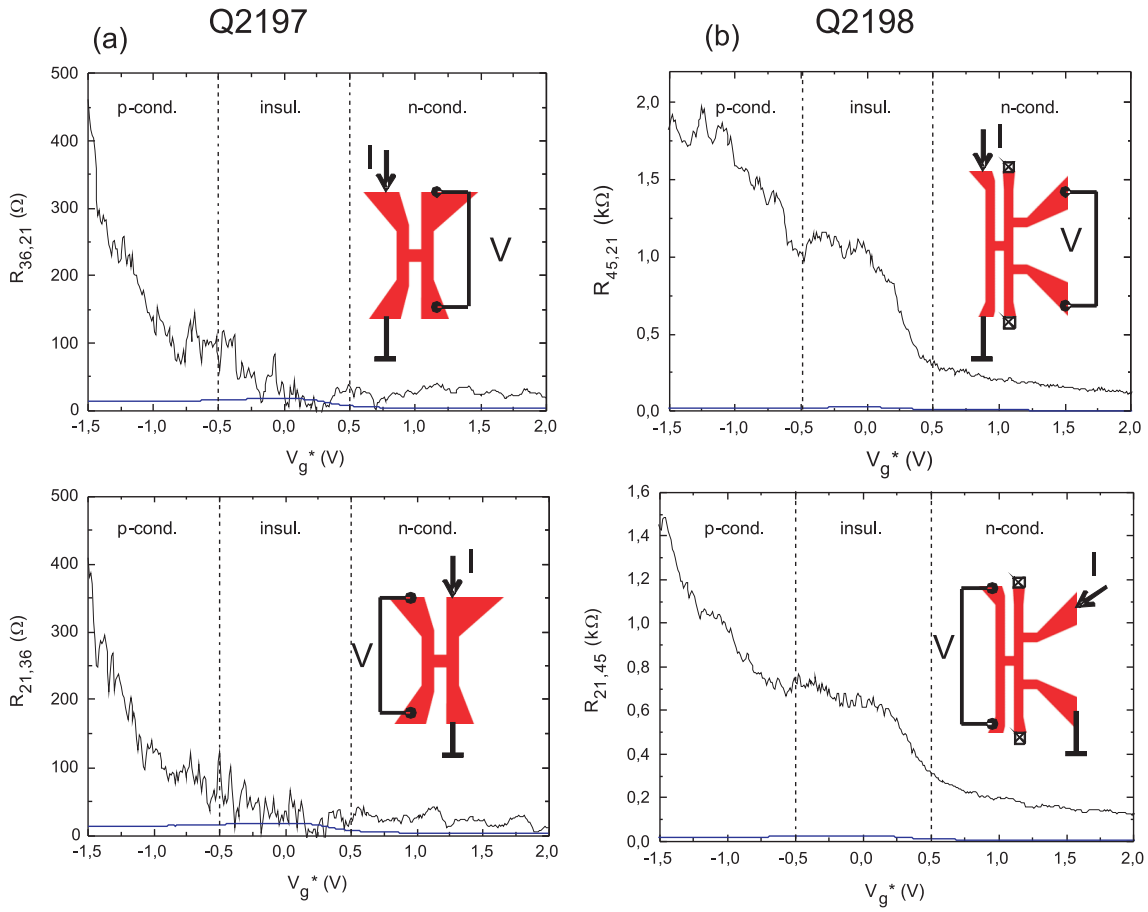

Figure 4.3: Non-local resistance signal for (a) Q2197 and (b) Q2198 . The inset indicates the measurement configuration for current injection (arrows) and voltage probes (V). The crosses indicate additional ohmic contacts. The blue solid curves indicates the residual voltage due to current spreading.

1 and 2 to the horizontal leg of the H-bar increases the ISHE signal in the measurement configurations of Fig. 4.3 (b), in agreement with the simulations.

Figs. 4.3 (a) and (b) show the non-local resistance in a configuration suitable for picking up the ISHE signal as a function of applied gate voltage for samples Q2197 and Q2198. The upper and lower panels show the results for an interchange of current and voltage contacts. One observes that for both samples the non-local signal strongly increases with gate voltage in the p-regime. The non-local resistance is of the order of several 100 Ω for sample Q2197 and larger than a kΩ for sample Q2198. This is the signal we attribute to the ISHE: on making the gate voltage more negative, we scan the Fermi level of the devices deeper and deeper into the valence band, leading to a strong increase in spin-orbit splitting [39]. The electrical signal of the H-bar is roughly quadratic [50] in the strength of the spin-orbit coupling. The relevant number here is the difference in population of the two spin-orbit split subbands, which evidently increases sharply from zero when the Fermi level leaves the gap. This explains the behavior observed for the p-regime. In the n-regime, the subband population asymmetry in the HgTe well is an order of magnitude smaller than in the p-regime and one hardly expects to observe a strong ISHE signal. Indeed, the experimental signal for positive gate voltages is small, does not show an appreciable dependence on gate voltage and cannot with confidence be attributed to the ISHE. Thus the phenomenology of our observations agrees well with what we expect for the ISHE. Moreover, for sample Q2197, any non-local contribution of the QSHE edge channels is totally suppressed, therefore, we attribute the observed signal to the ISHE. The finite non-local resistance around $V_g^* = 0$ for sample Q2198 is an indication that in this experiment we have some residual non-local QSHE signal, possibly owing the slightly larger width of the horizontal bar. However, the significant increase of the non-local resistance signal in the p-type metallic regime can only be induced by the ISHE. For both samples, the strong non-local signal in the p-regime remains almost unchanged even if the current and voltage contacts are exchanged. The traces thus obey the Onsager symmetry relations for linear response, which evidences the robustness of the experiment. We have incorporated in Fig. 4.3 (blue traces) the calculated residual voltages owing to current spreading at the applied bias voltage, to illustrate clearly that the observed signal is solely because of the ISHE. Note that these traces, calculated for diffusive transport, represent an upper limit for the actual spreading signal, as the transport in the devices is in fact quasi-ballistic, which strongly reduces the spreading effects.

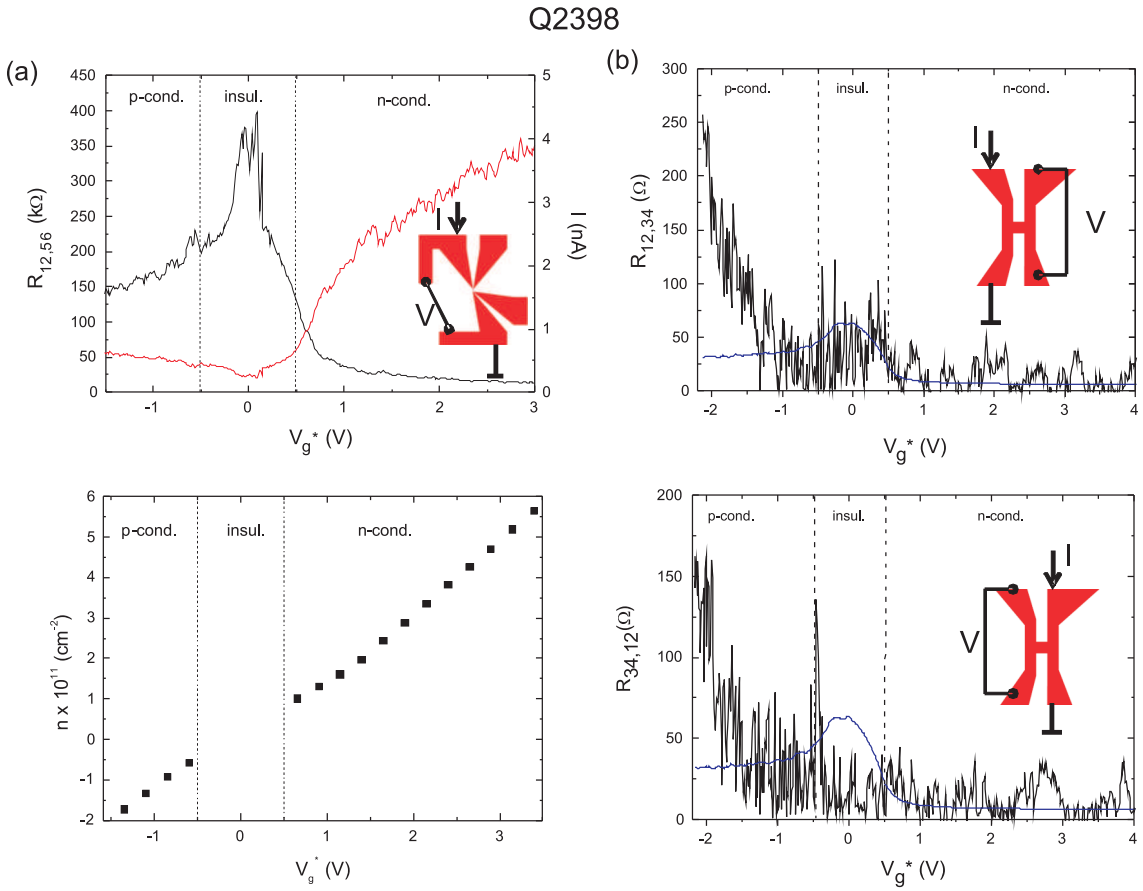

Figure 4.4: Non-local resistance signal for the non-inverted sample Q2398. Again, the insets indicate the measurement configurations, and the blue solid curves plot the residual voltage due to current spreading.

4.5 Non-inverted control sample

As a control experiment, we have performed similar experiments on sample Q2398, which has a narrower (5.7 nm) QW and a non-inverted band structure (its layout is similar to that of Q2197). Because of the much reduced Rashba spin-orbit splitting in this sample, one expects a much smaller non-local ISHE signal than for the experiments on Q2197 and Q2198. At the same time, the QSHE does not occur in wells with a normal band structure, so that in Q2398 any contributions from QSHE edge channels can be excluded. Fig. 4.4 a and b shows the results of these experiments. Fig. 4.4 a is comparable to Fig. 4.2 in that the top panel displays the device resistance and the bottom panel gives the dependence of the carrier concentration on the gate-voltage. Note that the resistance of the sample in the insulating regime is now much larger than for the inverted samples in Fig. 4.2. This is because the insulating regime in Q2398, owing to the absence of the QSHE edge

channels, is truly insulating. In the non-local resistance data of Fig. 4.4 b, we again observe a non-local voltage when the well is in the p-regime, but now reduced to a few hundred ohms, considerably smaller than in samples Q2198 and Q2197. We will show below that this signal is in line with theoretical expectations. In the insulating region and the n-regime the signal is virtually zero, which allows for a calibration of our estimate of the diffusive spreading signal (blue curve). Although in these experiments the spreading signal is no longer negligible in the p-regime, the different gate-voltage dependence of the spreading signal and actual data leaves no doubt that the observed signal is due to the ISHE.

4.6 Modelling by tight-binding calculations

For further confirmation of this interpretation of our experimental results, we now proceed with a numerical modelling of the experiments. Transport in the ballistic regime can be modelled theoretically within the well-established Landauer-Büttiker (LB) formalism. We first extract the effective masses and spin-orbit parameters from a series of 8×8 $\mathbf{k} \cdot \mathbf{p}$ band structure calculations [39], where the influence of the top gate voltage is included in a self-consistent manner. We evaluate these parameters in the vicinity of the Fermi energy, since at low temperatures, the quantum transport can be described by propagating modes at the Fermi energy. Figs. 4.5 (a) and (b) show the calculated inverted band structures for two representative carrier densities $n = 4.42 \times 10^{11}$ cm^{-2} and $p = 3.26 \times 10^{11}$ cm^{-2}. In inverted HgTe/HgCdTe quantum wells, the conduction band (conventionally labeled H1 [39]) has, in the vicinity of $k = 0$, a heavy-hole character while the valence band (E1) is electron-like. However, hybridization of the energy states starts to play a role for $k \neq 0$ and the spin-orbit splitting of both heavy hole- and electron-like bands must be considered in the form of a combination of linear and cubic terms. This is clearly relevant in samples Q2197 and Q2198, because we find that the Fermi level passes through the H1 band around $k = 0.15$ nm^{-1} in the n-regime and through the E1 band around $k = 0.35$ nm^{-1} in the p-regime (see Fig. 4.5). We find that the following Hamiltonian matches all important features emerging from the band structure calculations close to the Fermi level:

$$\begin{aligned} \hat{H} = & \frac{\hat{p}^2}{2m^*} + \frac{\lambda_1}{\hbar}(\hat{\sigma}_x p_y - \hat{\sigma}_y p_x) \\ & + \frac{i\lambda_2}{2\hbar^3}(\hat{p}_-^3 \hat{\sigma}_+ - \hat{p}_+^3 \hat{\sigma}_-) + H_{dis} \end{aligned} \tag{4.1}$$

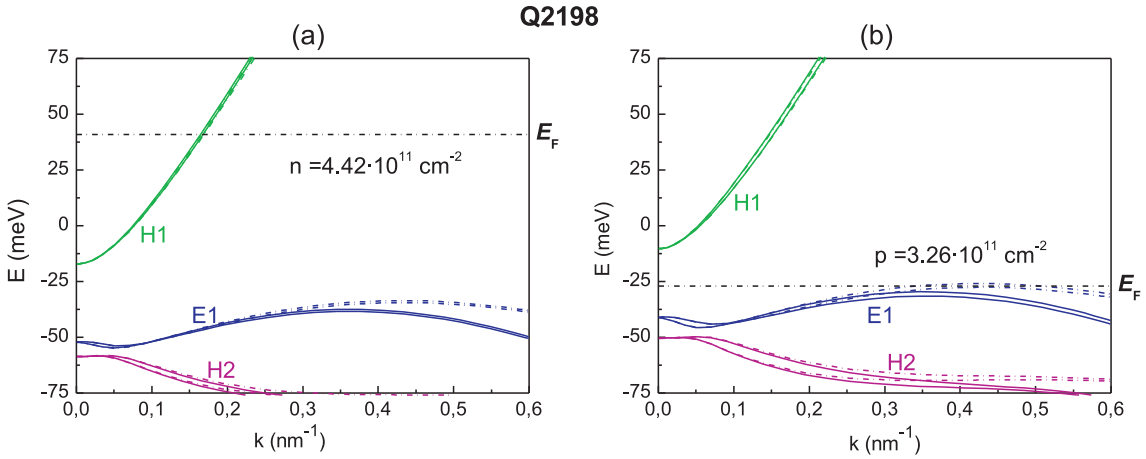

Figure 4.5: Band structure calculation for sample Q2198. 8×8 $\mathbf{k} \cdot \mathbf{p}$ band structure calculation for (a) n-type carrier density $n = 4.42 \times 10^{11}$ cm^{-2} and (b) p-type carrier density of $p = 3.26 \times 10^{11}$ cm^{-2}. The dashed-dotted line indicates Fermi level. The band structure calculations for sample Q2197 look similar.

where $m^* = 0.305\ m_e$ for the p-regime and $m^* = 0.03\ m_e$ for n-type samples. $\lambda_1 > 0$ and $\lambda_2 < 0$ are the spin-orbit coupling parameters and in the p-regime $|\lambda_2/\lambda_1| = 2.9$, $|\lambda_2/\lambda_1| = 2.5$ and 1.1 for samples Q2197, Q2198, and Q2398, respectively, while in the n-regime we have $|\lambda_2/\lambda_1| = 3.8$, $|\lambda_2/\lambda_1| = 4.5$, and 10.1 (again referring to samples Q2197, Q2198, and Q2398). H_{dis} is the disorder potential. The size of the structures used for the theoretical model is chosen in accordance with the actual dimensions of the experimental devices. In the experiments, the gate voltage causes changes in the spin-orbit splitting as well as in the carrier density and, as a consequence, in the Fermi energy. We include this effect in the simulations by changing the carrier density with gate voltage according to the experimental data of Figs. 4.2 (b) and 4.4 a. The Fermi energies depend on the strength of the spin-orbit interaction and the carrier densities. To perform real-space LB calculations we rewrite the continuum effective mass Hamiltonian in a tight-binding form (shown in detail in the online appendix), using the model structure shown in Fig. 4.6 (d). In the tight-binding calculations, the disorder is calculated by randomly selecting the on-site energies in the range $[-W/2, W/2]$, where $W = \hbar/\tau$, and τ is the transport scattering time calculated from the effective masses and the experimental mobility values. From the experimental mobility data, we find corresponding disorder strengths W between 0.155 and 0.3 meV. For such values of W, ten averages over disorder configurations are sufficient to obtain convergent results. The weak dependence of the observed effect on disorder in these materials is not surprising given that the disorder induced by short range scattering gives rise to vanishing vertex corrections [76].

We work in the linear response regime and the voltages on different probes are found within the LB formalism using boundary conditions where a charge current of 10 nA, for the setup of structure Q2197, is driven between contacts 1 and 2, while between contacts 3 and 4 the electric current is zero. In this configuration the non-local resistance signal is $R_{12,43} = V_{43}/I_{12}$. Details of the calculations can be found in the online Supplementary Information and in Ref. [50].

Fig. 4.6 (a), (b) and (c) show the theoretical predictions for the non-local resistance signal as a function of gate voltage for samples Q2197, Q2198, and Q2398, respectively, which can be directly compared with the experimental plots of Figs. 4.3 and 4.4. Clearly, the theoretical results not only show a very similar behavior to the experimental resistance signal, but even have semi-quantitative agreement. Furthermore, again in agreement with the experiment, the theoretically predicted signals are at least an order of magnitude stronger for the p- than for the n-regime, as a result of the much stronger difference in population of the valence band spin-orbit subbands. As in the experiment, we also find in the calculations that Q2198 exhibits a larger signal than Q2197. Analysis of the simulation results shows that this effect stems from the very close proximity of voltage leads 1 and 2 in sample Q2198 to the horizontal part of the H-bar. In addition, we calculate that both Q2197 and Q2198 yield larger signals than sample Q2398, where the spin-orbit interaction is smaller. The oscillating character of both experimental and theoretical non-local resistance data stems from the fact that the ratio of the Fermi energy to the spin-orbit splitting changes over the range of the gate voltage. We conclude that the numerical calculations are in good agreement with the experimental results and confirm that the observed effect is indeed the ballistic ISHE.

4.7 Supplementary Information for 'Evidence for the ballistic intrinsic spin-Hall effect in HgTe nanostructures'

In this section, we provide details about the model which has been used for our numerical calculations. In addition, we present experimental magnetoresistance data on our H-bar structures, which are fully consistent with an interpretation of the zero field non-local resistance data presented in the paper as being due to the ballistic intrinsic spin Hall effect.

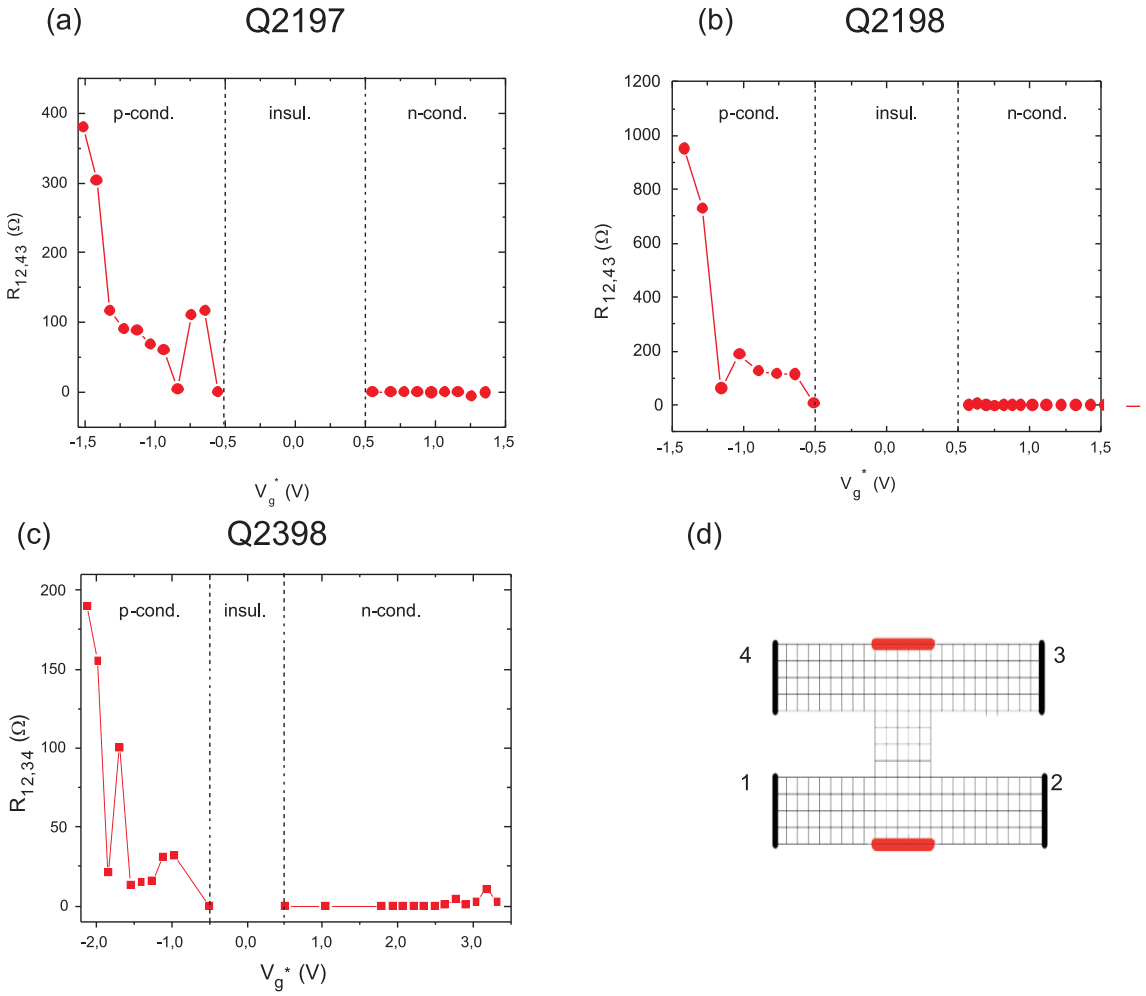

Figure 4.6: Theoretical predictions of the resistance signal induced by ISHE as a function of gate voltage for samples (a) Q2197 (b) Q2198 and (c) Q2398. For all samples, experimental values of the mobility and carrier densities were an input to the calculations. The effective mass and strengths of spin-orbit coupling were extracted from the band structure calculations (see text for details). (d) shows the tight-binding network used in the modeling.

4.7.1 Theoretical Appendix

For the high mobility HgTe-nanostructures studied experimentally an estimate of the mean free path yields $l \geq 2.5$ μm, which assures that the samples are in a quasi-ballistic regime and that the Landauer-Büttiker formalism is applicable. Thus, we need to build an appropriate effective mass Hamiltonian which can be discretized in real space through a tight-binding Hamiltonian. As a first step, we build an effective model which describes the transport properties of HgTe-nanostructures in the linear response regime in the vicinity of the Fermi energy. By analyzing the band structure, which is obtained from 8×8 $\mathbf{k}\cdot\mathbf{p}$ band structure calculations [39], it is found that the appropriate model contains linear and cubic Rashba contributions to the spin-orbit splitting. Therefore, the continuum effective mass model for inverted and normal band structure HgTe quantum wells has the form:

$$\hat{H} = \frac{\hat{p}^2}{2m^*} + \frac{\lambda_1}{\hbar}(\hat{\sigma}_x p_y - \hat{\sigma}_y p_x) + \frac{i\lambda_2}{2\hbar^3}(\hat{p}_-^3\hat{\sigma}_+ - \hat{p}_+^3\hat{\sigma}_-) + H_{dis}, \tag{4.2}$$

where $\hat{p}$ is the momentum operator, σ_x, σ_y are Pauli matrices, λ_1, λ_2 are the strengths of the spin-orbit interaction, m^* is the effective mass, and H_{dis} is the disorder potential. The spin-orbit coupling parameters as well as the effective mass are extracted from the band dispersions at the Fermi energy (values given above). In a tight binding model the momentum operator is substituted by: $\hat{p}_{x/y} = -\frac{i\hbar}{2a_{x/y}}(\hat{c}_j^\dagger\hat{c}_{j+a_{x/y}} - \hat{c}_j^\dagger\hat{c}_{j-a_{x/y}})$. This substitution leads to the transformation of the continuum effective mass Hamiltonian (Eq. 4.2) into the following (discrete) tight-binding form:

$$\begin{aligned}
H &= \sum_{j,\sigma}\epsilon_j c_{j,\sigma}^\dagger c_{j,\sigma} - t[\sum_{\langle i,j\rangle,\sigma} c_{i,\sigma}^\dagger c_{j,\sigma} + h.c.] \\
&+ t_{SO}[\sum_j -i(c_{j,\uparrow}^\dagger c_{j+a_y,\downarrow} + c_{j,\downarrow}^\dagger c_{j+a_y,\uparrow}) + \sum_j (c_{j,\uparrow}^\dagger c_{j+a_x,\downarrow} - c_{j,\downarrow}^\dagger c_{j+a_x,\uparrow}) + h.c.] \\
&+ t_{SO-k^3}[\sum_j c_{j,\uparrow}^\dagger c_{j+2a_x,\downarrow} - c_{j,\uparrow}^\dagger c_{j-2a_x,\downarrow} + i\sum_j c_{j,\uparrow}^\dagger c_{j+2a_y,\downarrow} - c_{j,\uparrow}^\dagger c_{j-2a_y,\downarrow} \\
&+ 3(1-i)\sum_j c_{j,\uparrow}^\dagger c_{j-a_x+a_y,\downarrow} - c_{j,\uparrow}^\dagger c_{j+a_x-a_y,\downarrow} + 3(1+i)\sum_j c_{j,\uparrow}^\dagger c_{j-a_x-a_y,\downarrow} - c_{j,\uparrow}^\dagger c_{j+a_x+a_y,\downarrow} \\
&+ 4i\sum_j c_{j,\uparrow}^\dagger c_{j+a_y,\downarrow} - c_{j,\uparrow}^\dagger c_{j-a_y,\downarrow} + 4\sum_j c_{j,\uparrow}^\dagger c_{j+a_x,\downarrow} - c_{j,\uparrow}^\dagger c_{j-a_x,\downarrow} + h.c.],
\end{aligned} \tag{4.3}$$

where $t = \hbar^2/(2m^* a_0^2)$ is a hopping parameter, $t_{SO} = \lambda_1/(2a_0)$ and $t_{SO-k^3} = -\lambda_2/(2a_0^3)$ are spin-dependent hopping parameters originating from the spin-orbit interaction terms, a_x,a_y are the mesh lattice parameters in x and y directions and a_0 is the mesh lattice spacing. The first term on the right hand side of Eq. 4.3 represents a quenched disorder potential. Disorder is introduced by randomly selecting the on-site energy ϵ_j in the range [-W/2,W/2]. Within the leads the SO coupling is zero and therefore each lead should be considered as having two independent spin-channels. Thus, there is no ambiguity with the definition of spin currents which is based on measurements in leads where the spin is conserved. These leads are modeled as electron reservoirs of chemical potentials $\mu_1, \ldots, \mu_N$, where N is the number of leads under consideration. Within the Landauer-Büttiker formalism [77, 50] the particle current which is passed through a particular channel is given in the low temperature limit, $k_B T << E_F$, and for low bias voltages by:

$$I_{p,\sigma} = (e^2/h) \sum_{q\sigma'} T_{p,\sigma;q,\sigma'}[V_p - V_q], \tag{4.4}$$

where p labels the lead and $T_{p,\sigma;q,\sigma'}$ is the transmission coefficient at the Fermi energy E_F between the (p,σ) channel and the (q,σ') channel. This transmission coefficient is obtained from $T_{p,\sigma;q,\sigma'} = \mathrm{Tr}[\Gamma_{p,\sigma} G^R \Gamma_{p,\sigma} G^A]$ where $\Gamma_{p,\sigma}$ is given by

$$\Gamma_{p,\sigma}(i,j) = i[\Sigma^R_{p,\sigma}(i,j) - \Sigma^A_{p,\sigma}(i,j)], \tag{4.5}$$

and

$$G^{R/A}(i,j) = [E\delta_{i,j} - H_{i,j} - \sum_{p,\sigma} \Sigma^{R/A}_{p,\sigma}(i,j)]^{-1} \tag{4.6}$$

are the retarded adwanced Green's function of the sample $G^{R/A}$. The leads are taken into account through the self energy $\Sigma^{R/A}_{p,\sigma}(i,j)$. Here, the position representation of the matrices $\Gamma_{p,\sigma}$, G^R, and Σ^R is in the subspace of the sample, i.e. it only includes sites within the sample and the self energy describes the fact that there is a finite probability that an electron will escape from the sample back into the leads. Within the above formalism we can define the spin current through each channel as $I^s_{p,\sigma} = (e/4\pi) \sum_{q\sigma'} T_{p,\sigma;q,\sigma'}[V_p - V_q]$. Defining lead $i = 1$ as source, lead $i = 2$ as drain, and leads $i = 3$ and 4 as voltage probes, all voltages are obtained considering the following boundary conditions: $I_{i,\uparrow} + I_{i\downarrow} = 0$ for $i = 3$ to 4, $I_{1,\uparrow} + I_{1\downarrow} = 1$ and $I_{2,\uparrow} + I_{2\downarrow} = -1$. These are later compared to measured voltages by setting the current value between leads 1 and 2 to a typical value of

$I_{1\to 2} = I_1 = 10$ nA. The arbitrary zero of the electric potential is fixed by setting $V_2 = 0$. Correspondingly, the non-local resistance is defined as $R_{12,34} = (V_3 - V_4)/I_1$, if current is driven between contacts 1 and 2, and the voltage difference is measured between contacts 3 and 4.

4.7.2 Additional Experimental Material

In this document, we discuss the magnetoresistive behavior of the nanostructures discussed in the paper. Specifically, we present experimental results on a gated H-bar structure with slightly larger dimensions, i.e. a nominal channel width of 0.7 μm. This sample serves as an intermediate between samples with 1 μm wide channels, where the QSHE edge channels are free from backscattering (Ref. [25]), and the narrow samples described in the manuscript, in which the QSHE is almost fully suppressed. The schematic layout of this sample, Q2345, is given in Fig. 4.7.

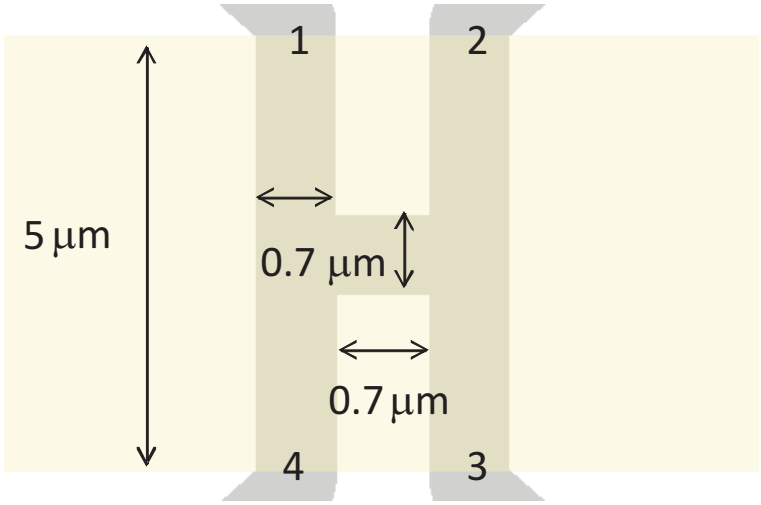

Figure 4.7: Schematic H-bar sample layout. The nominal sample (grey) width is 0.7 μm. The covering top gate is 5 μm long (light yellow). The numbers indicate the ohmic contacts.

The sample has been fabricated from a n-doped wafer with an inverted type-III QW of 11 nm width. The un-gated sample's carrier density and mobility are 3.9×10^{11} cm^{-2} and 286000 cm^2/(Vs), respectively. The gate dependent non-local resistance $R_{14,23}$ (where the driving current is passed between contacts 1 and 4 and the resulting voltage is measured between contacts 2 and 3) is shown in Fig. 4.8. On lowering the gate voltage, the carrier density is reduced, passes through an insulating regime between -2 and -3.5 V and

reaches the p-regime for gate-voltages more negative than -4 V. In the insulating regime, the non-local resistance shows a distinct maximum which is related to the quantum spin Hall effect (QSHE). For a four terminal device the expected quantized conductance value is 6.5 kΩ. The slightly higher value indicates that additional backscattering mechanisms are present in the QSHE regime. These effects are discussed in detail in Ref. 20 of the manuscript. Note that the QSHE signal presented here is obtained for the same current and voltage probes configuration as in Fig. 4.3 a) and b). In the somewhat wider sample Q2345 shown here, a very strong non-local signal is observed for the insulating (QSHE) regime. As discussed in the paper, the wider connection between the two legs of the H-structure reduces backscattering between counter-propagating channels on opposite edges and the QSHE survives the non-local experiment - in contrast to the results presented in the paper for narrower samples.

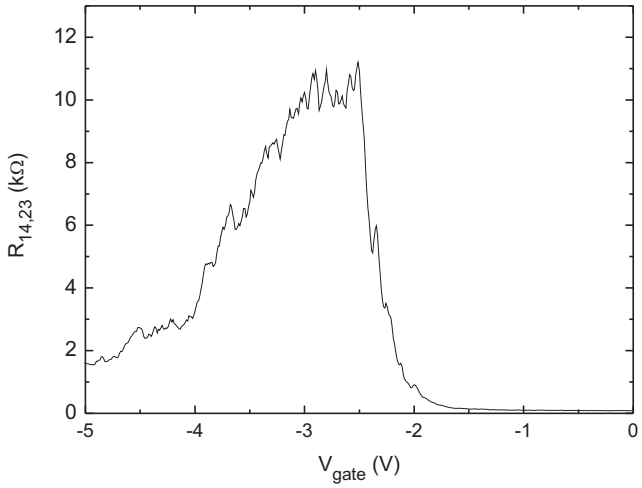

Figure 4.8: Gate voltage dependent non-local resistance $R_{14,23}$.

Additionally, Fig. 4.8 confirms the observations of the narrow channel device structures as to the ballistic intrinsic spin Hall effect (ISHE): the non-local signal in the metallic n-regime (V_{gate} $>$ -1 V) is vanishingly small, while it is of the order of a few kΩ in the p-regime.

Fig. 4.9 shows the behavior of the non-local ISHE signal deep into the p-regime as a function of magnetic field, both for in-plane and perpendicular-to-plane configurations. We

observe that $R_{14,23}$ drops to approximately 50% for a magnetic field of 3 T for perpendicular magnetic field, while the ISHE signal remains almost unaffected when magnetic field is parallel to the quantum well. This magnetic field-induced suppression is markedly smaller than known from the QSHE (which depends on time-reversal-symmetry), and it is exactly the behavior that is expected for the ballistic ISHE, as we will now discuss in detail.

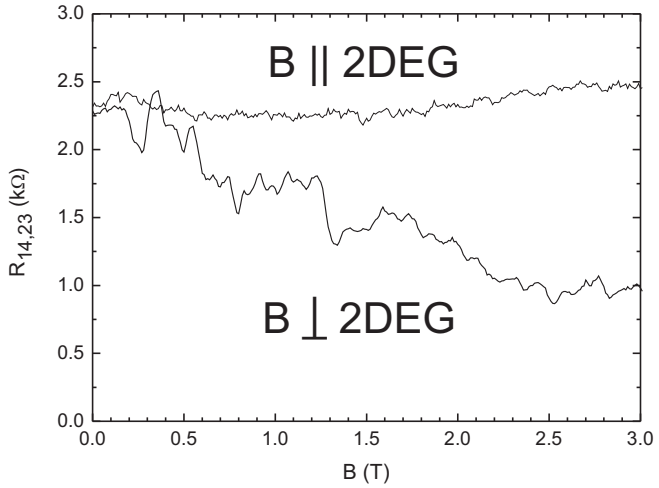

Figure 4.9: Magnetic field dependence of the non-local resistance $R_{14,23}$ for a gate voltage of -4.5 V. The magnetic field was oriented parallel ($||$) and perpendicular $\perp$ to the plane of the 2DEG.

In the simplest possible picture [49], the spin-Hall conductivity originates from the precession of electron spins around Rashba-type k-dependent magnetic field which gives rise to the effective spin-torque and spin-Hall current. An external magnetic field (perpendicular or parallel to 2DEG) causes a pinning of the carrier spins and hence, the spin-Hall effect decreases with increasing magnetic field strength (B). However, the strength of the external magnetic field which is required to destroy the spin-Hall effect depends on the angle between the Rashba- and the magnetic field. In the ballistic transport regime [78], the spin-Hall conductivity drops as $\alpha^2 k_F^2/(\alpha^2 k_F^2 + \hbar^2\omega_0^2)$ in a perpendicular magnetic field, where α is the strength of spin-orbit interactions, k_F is the wave vector at the Fermi level, $\hbar$ is Planck's constant and ω_0 is the Larmor frequency. In the parallel magnetic field configuration, if one assumes that magnetic and Rashba fields to point in the same direction, one expects that the signal will be less sensitive to the strength of the magnetic field. Even for $\alpha k_F = \hbar\omega_0$ there will be a large effective spin-current and, hence, the

magnetization and the non-local resistance signal will decrease much slower. This is exactly what is observed experimentally: for a magnetic field perpendicular to the plane of 2DEG, the non-local resistance signal drops to one half of its value in a magnetic field of 3 T where the magnitudes of the spin-orbit splitting (calculated using our 8×8 $\mathbf{k} \cdot \mathbf{p}$ band structure model) and the Zeeman energy are identical and equal to 3 meV. For a magnetic field applied in the plane of the 2DEG a much larger magnetic field strength is required to destroy the ISHE signal (thus, the signal remains constant up to 3 T).

Chapter 5

Spin polarization of the quantum spin Hall edge states

This chapter is based on the publication: *Christoph Brüne, Andreas Roth, Hartmut Buhmann, Ewelina M. Hankiewicz, Laurens W. Molenkamp, Joseph Maciejko, Xiao-Liang Qi and Shou-Cheng Zhang; 'Spin polarization of the quantum spin Hall edge states', Nature Physics* ***8****, 485-490, 2012*.

5.1 Abstract

The prediction and experimental verification of the quantum spin Hall state marked the first discovery of a new state of matter now known as topological insulators. The quantum spin Hall effect is characterized by gapless spin polarized counterpropagating edge channels in two-dimensional topological insulators. While the helical character of these edge channels is by now well established, an experimental confirmation that the transport in the edge channels is spin-polarized is still outstanding. We report experiments on nanostructures fabricated from HgTe quantum wells with an inverted band structure, in which a split gate technique allows us to combine both quantum spin Hall and metallic spin Hall transport in a single device. In these devices, the quantum spin Hall effect can be used as a spin current injector and detector for the metallic spin Hall effect, and vice versa, allowing for an all-electrical detection of spin polarization.

5.2 Introduction

The discovery that HgTe quantum wells (QWs) with an inverted band structure are 2-dimensional topological insulators has generated a great interest in this novel state of quantum matter [7, 8, 42]. When the thickness d of the HgTe QW is increased beyond a critical value d_c, a quantum phase transition turns a conventional insulator into its topologically non-trivial counterpart. In this so-called quantum spin Hall (QSH) phase [6, 22], current-carrying states are confined at the edge of the sample, while the bulk is insulating. These edge states are protected against backscattering from non-magnetic impurities [79, 80, 81] and their propagation direction is helical, i.e. that opposite spin states counter-propagate along a given edge of the sample. When the applied gate voltage places the Fermi level inside the bulk gap, two-terminal transport experiments measure a quantized conductance of $2e^2/h$ with e the electron charge and h the Planck constant, independent of the sample width, which constitutes strong evidence for edge state conduction [8]. More recent nonlocal transport measurements in the QSH regime unambiguously establish that transport occurs through topologically protected edge channels [25, 82]. While edge state conduction in the QSH regime is thus experimentally well established, there exists so far no direct experimental evidence that the transport in the helical edge states of 2D topological insulators is spin-polarized, which is a fundamental characteristic of this new state of matter.

In this work, we construct novel devices (Figs. 5.1 and 5.2 a) that enable us to study the spin polarization of the QSH edge states by purely electrical means. First of all, these devices allow us to detect the spin polarization of the QSH edge states (Fig. 5.1 b) via the inverse spin Hall effect [50, 69, 52] (SHE^{-1}). Second, our devices enable us to show that because of their helical nature, the QSH edge states can be used as a detector of spin current (Fig. 5.1 a). In our devices, the spin current is generated by the intrinsic ballistic spin Hall effect [50, 83] (SHE) exhibited by a HgTe QW in the metallic regime [52]. These two experiments establish for the first time spin polarization of the helical edge states in topological insulators, and also demonstrate potential applications of the QSH effect for spintronic devices.

5.3 Detecting the spin polarization in non-local transport experiments

Before presenting our results, we first describe the principle of our experiment in more detail. Since the magnetic field originating from spin polarized carriers in helical edge channels is too small to be detected directly, we have designed an experiment that converts magnetic information into an electrical signal. Figure 5.1 illustrates the idea of the experiments, which are performed on an H-shaped mesa structure (which we call 'H-bar') in which the carrier concentration in the two legs of the 'H' can be adjusted separately. Consider the situation illustrated in Fig. 5.1, where the bottom leg is metallic (indicated by the green color, and either n- or p-type) and the top leg is tuned into the QSH regime (indicated by the yellow color), with the counter-propagating helical edge channels depicted as blue and red trajectories. We perform two separate complementary experiments.

In Fig. 5.1 a, the current is injected into the metallic part of the structure (contacts 3 and 4) while a voltage signal is detected across the top leg (contacts 1 and 2), which is gated into the QSH insulator state. The inverted band structure in HgTe results in a large spin-orbit coupling [39, 83], which has previously enabled us to observe a ballistic intrinsic SHE in a small H-bar structure with a homogeneous carrier profile [52]. Similarly, when in the experiment of Fig. 5.1 a a charge current is injected into the metallic leg, the intrinsic SHE will induce a separation of carriers with opposite spin polarizations toward opposite edges of this leg. This leads to a difference in chemical potential for opposite spin states in the area where the metallic part of the structures borders on the QSH region. The spin polarized helical edge channels coming from the QSH region couple selectively to the chemical potential of the matching spin species in the metallic region and transfer this difference in potential to voltage contacts 1 and 2. For non-spin-selective edge channels the voltage signal is expected to be zero, while for the spin polarized QSH edge channels we expect a nonzero signal. Thus the observation of a nonlocal signal in this configuration is evidence that the metallic leg develops an intrinsic SHE, as well as that the helical edge channels are spin polarized in the QSH insulator regime.

In the reverse configuration of Fig. 5.1 b, the current is injected (contacts 1 and 2) into the area of the sample that is gated into the QSH regime, while a nonlocal voltage drop is measured across the metallic leg (contacts 3 and 4). In this configuration, the spin polarized helical edge channels inject a spin polarized current into the metallic leg, causing a local imbalance in the chemical potential of spin-up and spin-down polarized carriers.

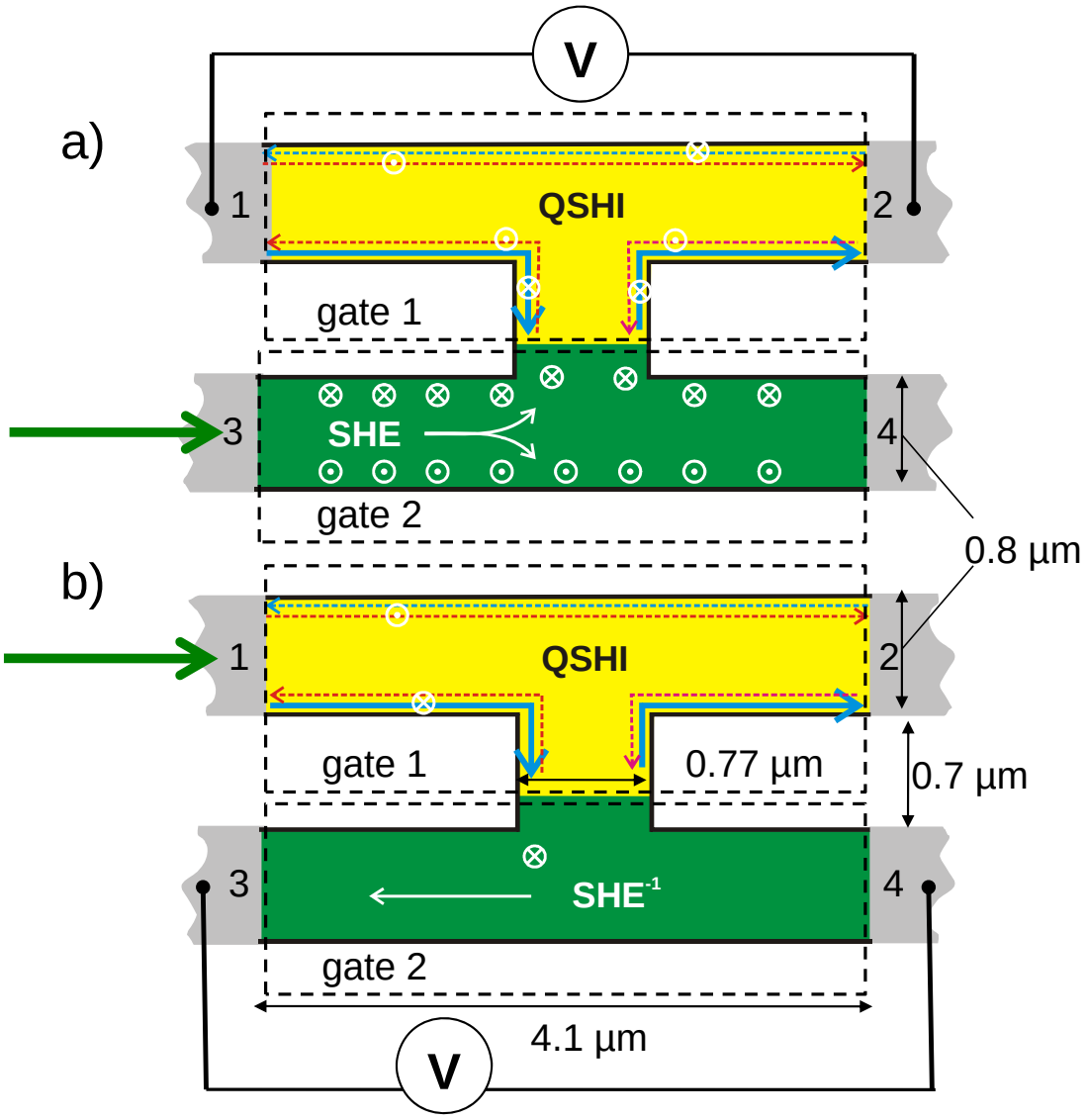

Figure 5.1: Schematic layout of the two experiments on split-gated H-bar devices discussed in this paper. The dimensions indicated are those of the actual devices used in the experiments. a) shows the configuration where the current is injected into a metallic region (green, contacts 3 and 4). The spin-orbit interaction leads, through the spin Hall effect (SHE), to spin accumulation at the edges of the leg, as indicated schematically. The upper part of the structure (yellow) is in the QSH regime; the difference in chemical potential between the two spin states in the interface region is transferred by the helical edge channels to voltage contacts 1 and 2. In b) the injector and detector regions are interchanged: the current is injected into the (spin-polarized) helical edge channels of the upper leg, causing a spin accumulation in the lower metallic region. The inverse spin Hall effect (SHE^{-1}) converts the spin accumulation into a voltage signal.

Due to the SHE^{-1} (see Refs. [50, 69, 52]), the spin current in the metallic region induces a voltage between contacts 3 and 4. Again, this voltage can only develop provided the helical edge channels are spin polarized, and the metallic leg exhibits the SHE^{-1}.

A possible complication in both of the above experiments is the detection of a stray spreading voltage. In the configuration of Fig. 5.1 a, this could result from a voltage drop in the metallic leg along the interface with the area in the QSH insulator regime, while in Fig. 5.1 b, the finite distance between in- and outgoing edge channels at this interface could produce a similar effect. However, in practice such stray voltages are strongly reduced by the exact layout of the experiment, the quasi-ballistic nature of the transport in the metallic leg and the finite width of the edge channels.

5.4 Fabrication and transport characterization of two-dimensional topological insulators

Our H-bar structures are fabricated from inverted symmetrically doped HgTe/HgCdTe type-III QWs with a nominal well width of 9 nm, located 74 nm below the surface. At a temperature of 4 K (and for a grounded gate), the carrier density is $n \approx 4 \times 10^{11}$ cm^{-2} . The carrier mobility is then $\mu \approx 1.1 \times 10^5$ cm^2/(V·s), yielding an elastic mean free path larger than 2 μm. The devices are patterned using optical and electron beam lithography, with dimensions as indicated in Fig. 5.1. In order to control the carrier density, the device is gated by Au gate electrodes separated from the sample surface by a 110 nm thick insulating Si_3N_4/SiO_2 multi-layer stack. By applying a voltage $V_{\rm gate}$ to the top gates, the electron carrier density of the QW can be adjusted, going from an n-type behavior for $V_{\rm gate} > 0$ through the bulk insulator state into a p-type regime for $V_{\rm gate} < 0$. For reasons of comparison, the experimental data in Fig. 5.2, 5.3 and 5.4 are plotted as a function of a normalized gate voltage $V^*_{\rm gate} \equiv V_{\rm gate} - V_{\rm thr}$, where the threshold voltage $V_{\rm thr}$ is defined as the voltage for which the resistance is largest in a particular fixed reference measurement. As is evident from the characterization data in Fig. 5.2 b and c, which were obtained from a Hall bar fabricated from the same wafer material as the H-bar nanostructures, we find that for gate voltages $V^*_{\rm gate} \gtrsim 0.5$ V the QW is n-type metallic, and for $V^*_{\rm gate} \lesssim -0.5$ V it is p-type metallic. The split-gate design (gates 1 and 2) of Fig. 5.1 provides an independent control of the carrier density for each leg of the H-bar structure, enabling us to gate one part of the sample into the QSH insulator regime and the other part into either n- or p-type

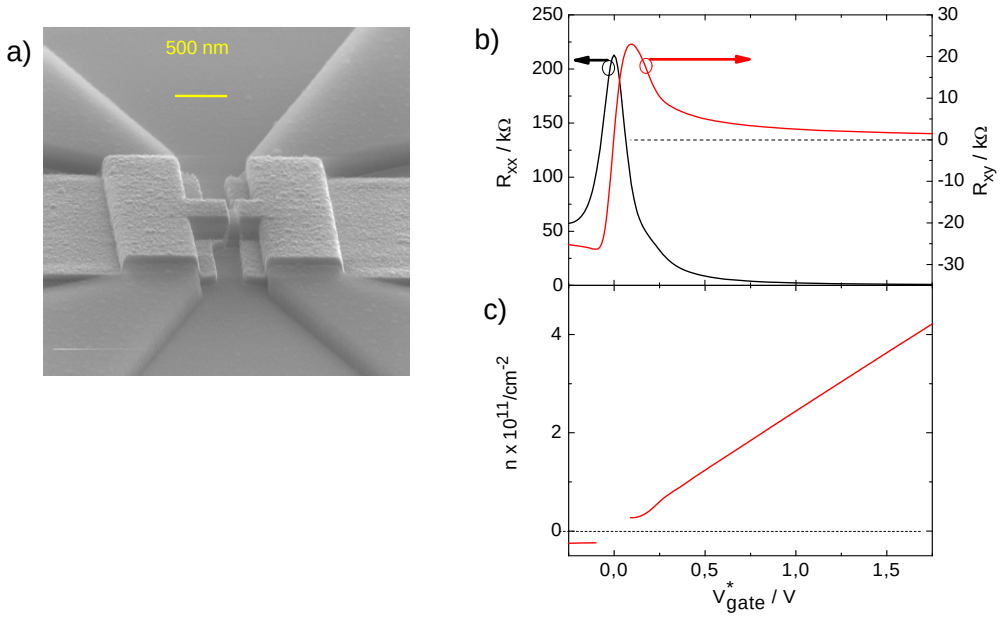

Figure 5.2: Characterization of devices. (a) An electron micrograph of the actual device structure (rotated by 90 degrees compared to Fig. 5.1). (b) and (c) Gate voltage dependence of the longitudinal resistance R_{xx} (black) and Hall resistance R_{xy} (red) at B = 1 T, and the inferred carrier density, n, of a macroscopic Hall bar, 600 μm x 200 μm in size, fabricated from the same HgTe wafer as the nanostructures used in the experiments of Figs. 5.3 and 5.4.

metallic regimes. An electron microscope picture of the actual device structure is shown in Fig. 5.2 a. The transport measurements are done at a constant temperature of 1.8 K employing quasi-dc low frequency (13 Hz) lock-in techniques using a voltage bias below 100 μV.

5.5 Nonlocal signals as evidence for the spin polarization of the quantum spin Hall state

While experiments have been performed on a variety of different devices and yield similar results, for reasons of consistency we will discuss here a single device with dimensions as indicated in Fig. 5.1. The results of the experiments are shown in Figs. 5.3 and 5.4, corresponding to the measurement configurations of Figs.5.1 a and b, respectively. In the upper three panels of the figures, the nonlocal resistance is plotted as a function of gate 1, while in the lower panel, gate 2 is swept.

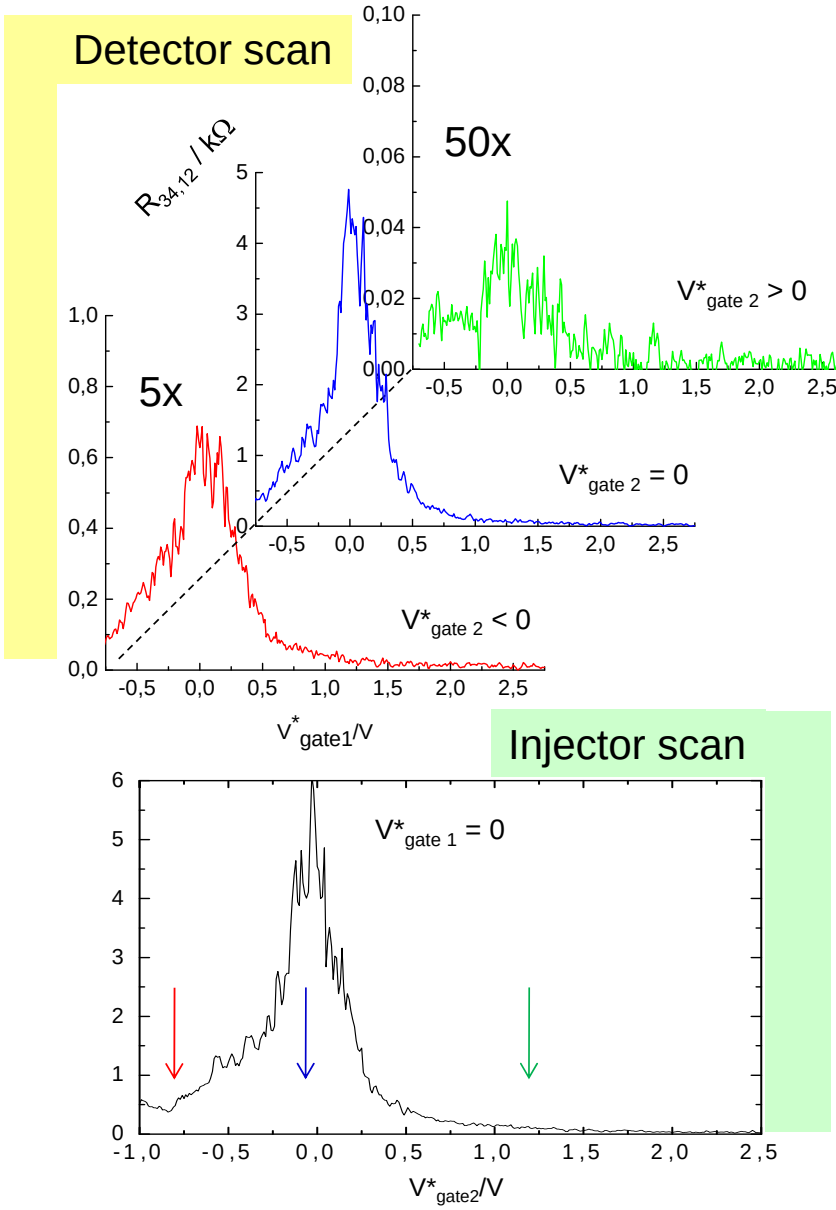

Figure 5.3: Experimental nonlocal resistance data corresponding to the measurement configuration of Fig. 5.1 a). In the bottom (green) panel, the gate on the current injection leg is swept, varying the area from p- to n-metallic conductance, while the detector (top) leg is kept in the middle of the QSH insulator regime. The red, blue and green arrows denote gate voltages where the injector region is p-type metallic, QSH insulating and n-type metallic, respectively. In the top panel, the gate in the detector area is varied at exactly these injector settings.

Figure 5.3 corresponds to the layout of Fig. 5.1 a, and the detected nonlocal signal can consequently be denoted as $R_{34,12}$, i.e. the voltage measured between contacts 1 and 2 divided by the current passed between contacts 3 and 4. When we sweep the gate on the injector area (gate 2) while the detector is tuned into the QSH regime ($V^*_{\mathrm{gate1}} = 0$), we observe (lower panel in Fig. 5.3 a pronounced maximum around $V^*_{\mathrm{gate1}} = 0$, and smaller but finite values on both sides. The signal around $V^*_{\mathrm{gate1}} = 0$ reaches approximately the quantized value ($h/4e^2$) observed in our previous experiments on nonlocal transport in the QSH regime [25]. We attribute the slight deviation from perfect quantization to imperfect gating in the not gate-covered region between gates 1 and 2. Imperfectly gated regions in the sample can act as dephasing centers for edge electrons, which can lead to a deviation from the expected quantized nonlocal resistance [25, 81]. In addition, in HgTe QW devices subsequent gate voltage sweeps can charge interface trap states in a different way [74], leading to different dephasing effects and a different magnitude of the deviation from quantized resistance for each gate voltage sweep.

Apart from the large signal in the QSH regime, the measurements also exhibit a non-vanishing nonlocal signal when the area underneath gate 2 is metallic, either n- or p-type, and thus corresponds to the injector region depicted in Fig. 5.1 a. The origin of this finite signal becomes more evident when the injector gate voltage is set at a fixed value either in the p-type ($V^*_{\mathrm{gate2}} = -0.75$ V < 0) or in the n-type metallic regime ($V^*_{\mathrm{gate2}} = 1.0$ V > 0) while the voltage on gate 1 is swept (top panel of Fig. 5.3). Evidently, a significant increase in the nonlocal signal is observed, with a peak when the detector is exactly in the QSH insulator regime. This is the observation anticipated above: one may expect a nonlocal signal of this amplitude only when the metallic leg exhibits a SHE and the edge channels in the QSH leg are spin polarized. Our data also show that the nonlocal signal for the p-type injector ($V^*_{\mathrm{gate2}} = -0.75$ V) is more than ten times larger than that for the n-type injector ($V^*_{\mathrm{gate2}} = 1.0$ V). This is consistent with our experimental observations on the SHE signal in all-metallic HgTe QW [52], where the nonlocal signal is about an order of magnitude larger in the p-regime than in the n-regime and results from enhanced spin-orbit splitting in the valence band [39].

Our data for the reverse configuration of Fig. 5.1 b are shown in Fig. 5.4. The sweep of gate 2 in the bottom panel now corresponds to the detection leg, and one can directly see that also in this configuration we observe a finite nonlocal signal (in this case $R_{12,34}$), even when the detector is metallic (red and green arrows). The upper panel shows the effect of sweeping the injector leg (gate 1), and indicates that the nonlocal signal peaks when

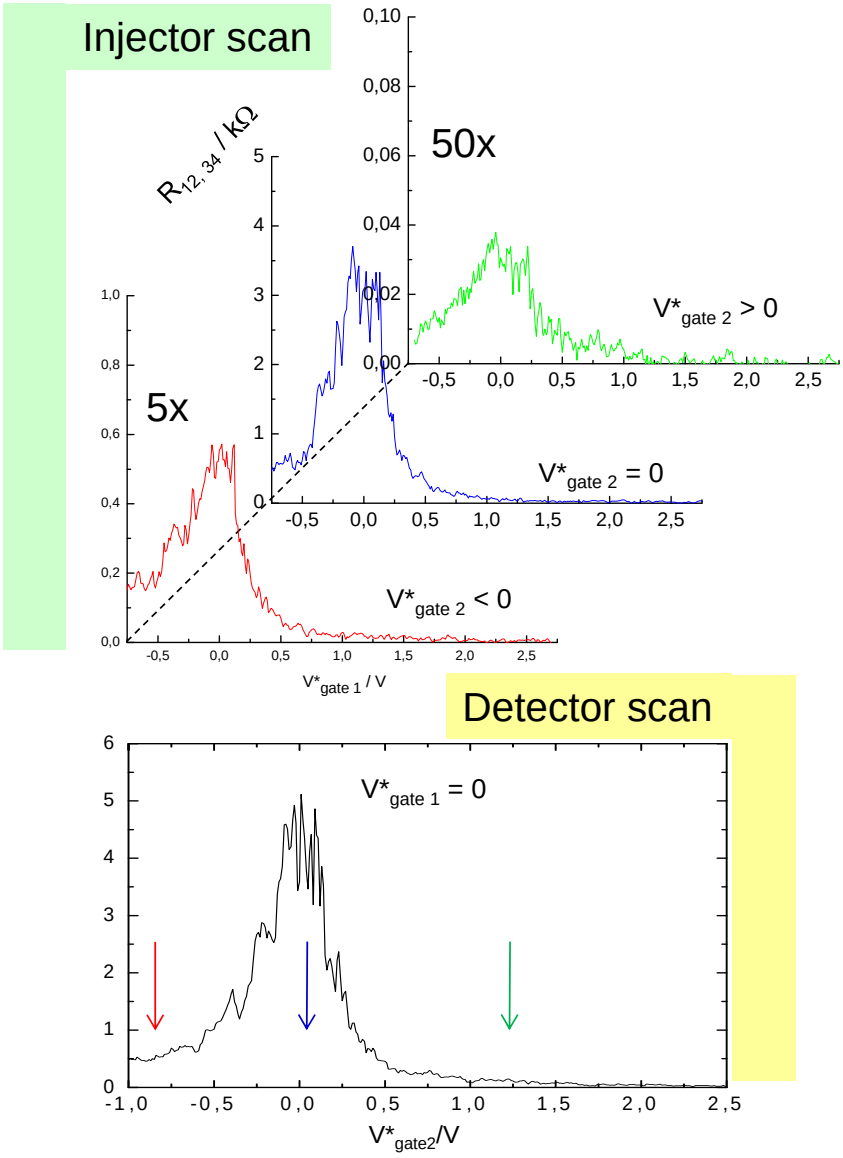

Figure 5.4: Experimental nonlocal resistance data corresponding to the measurement configuration of Fig. 5.1 b). In the bottom (yellow) panel, the gate on the detection leg is swept, varying the area from p- to n-metallic conductance, while the injector (bottom) leg is kept in the middle of the QSH insulator regime. The red, blue and green arrows denote gate voltages where the detector region is p-type metallic, QSH insulating and n-type metallic, respectively. In the top panel, the gate in the injector area is varied at exactly these detector settings.

the injector is in the QSH state. As in the previous configuration of Fig. 5.3, we observe an order of magnitude increase in the nonlocal signal when the metallic detector is p-type ($V^*_{\mathrm{gate2}} = -0.82$ V) as compared with an n-type detector ($V^*_{\mathrm{gate2}} = 1.2$ V). As noted above, our observation of the nonlocal signal is evidence that the helical edge channels generate a spin accumulation at the interface between the QSH injector and the metallic detector, which responds by the SHE^{-1}.

The results in Figs. 5.3 and 5.4 look very similar and, in fact, are expected to do so on account of the Onsager-Casimir symmetry relations for the nonlocal resistances $R_{mn,kl}$ in a four-probe device [43, 55],

$$R_{mn,kl}(\mathbf{B}) = R_{kl,mn}(-\mathbf{B}), \tag{5.1}$$

where the first pair of indices refers to the current probes, the second pair refers to the voltage probes, and $\mathbf{B}$ is the magnetic field. In the present setup, the magnetic field is zero and we expect $R_{34,12} = R_{12,34}$. One possible explanation for the small deviations from exact Onsager-Casimir symmetry observed in Fig. 5.3 and 5.4 is the random charging effects of pinned inhomogeneities (or 'trap states') mentioned earlier. Two subsequent gate voltage sweeps can result in a different interface potential due to these charging effects [74], which changes the internal state of the conductor. Note however that the symmetry between Fig. 5.3 and 5.4 is more accurate in the doped regimes away from the nominally insulating regime, which is expected since a higher carrier density can more effectively screen the interface trap potentials and thus make the internal state of the conductor less sensitive to trap charging effects.

5.6 Modelling and additional discussion of the experiment

In order to better understand the experimental results, we have performed semi-classical Monte Carlo calculations to obtain a theoretical estimate of the nonlocal resistance based on the sample geometry (Fig. 5.1). We focus on the setup illustrated in Fig. 5.1 b, where the QSH insulator acts as a spin injector and the metallic region detects the spin polarization of edge channels through the SHE^{-1}. We calculate the nonlocal resistance $R_{12,34}$ when the current is driven between contacts 1 and 2 and the voltage is measured between contacts 3 and 4. $R_{12,34}$ can be expressed in terms of the transmission coefficients [43, 55] T_{ij} for the metallic region only (Eq. S1 of the supplementary online material). The T_{ij} are

calculated within the semiclassical Monte Carlo method [84], which is a reasonable approximation for Fermi wavelengths $\lambda_F \ll L$ where $L \sim 1$ μm is the characteristic linear size of the device (Fig. 5.1 and 5.2 a). Electrons are injected at the QSH-SHE^{-1} interface (yellow-green interface in Fig. 5.1 b), and propagate quasi-ballistically into the metallic T-structure (green region in Fig. 5.1 b) according to semiclassical equations of motion [85]. These equations are derived using an effective 4-band model for HgTe QW [7] which explicitly contains the effects of intrinsic spin-orbit coupling due to atomic coupling between bands [83]. This intrinsic spin-orbit coupling can be visualized as resulting from a Rashba field due to the edges of the typical mesa structure used in experiments [83]. The samples were symmetrically doped and therefore designed the way so the Rashba term originating from the applied gate was minimal. Therefore we omitted this contribution in the simulations. Details of the calculation are included in the supplementary online material.

We find that the conversion of the spin signal to the electrical signal through the SHE^{-1} is dominated by the intrinsic spin-orbit interaction, while stray contributions due to voltage spreading are negligible (see Fig. S3 in the supplementary online material). Fig. 5.5 shows the theoretical prediction of the nonlocal resistance signal as a function of the carrier concentration in the metallic detector. (Note that the semiclassical simulation breaks down when the chemical potential is too close to the insulating gap.) The scattering induced by the intrinsic spin-orbit interaction is more effective when carriers have smaller kinetic energy, and therefore smaller wave vectors at the Fermi level. Since the effective mass in the p-regime is larger than that in the n-regime [52], for comparable densities the kinetic energy will be smaller in the p-regime. This can explain the larger nonlocal resistance signal for the p-regime in comparison with the n-regime, as well as the decrease of the signal upon increase in carrier concentration.

In order to further validate the above interpretation, we have performed a number of control experiments: Firstly, varying the injector size (from 200 nm to 400 nm) hardly influences the observed resistance signals. This rules out that the signal has a contribution due to (diffusive) voltage spreading and confirms that our samples are indeed in the quasi ballistic regime. Moreover, we have measured the dependence of the nonlocal resistance signals on perpendicular and in-plane magnetic fields. While the in-plane magnetic field does not influence the signal strength in the perpendicular case a decrease of the nonlocal signal can be observed. This shows that the effect indeed depends on the spin polarization of the electrons. A more detailed information about these additional experiments can be

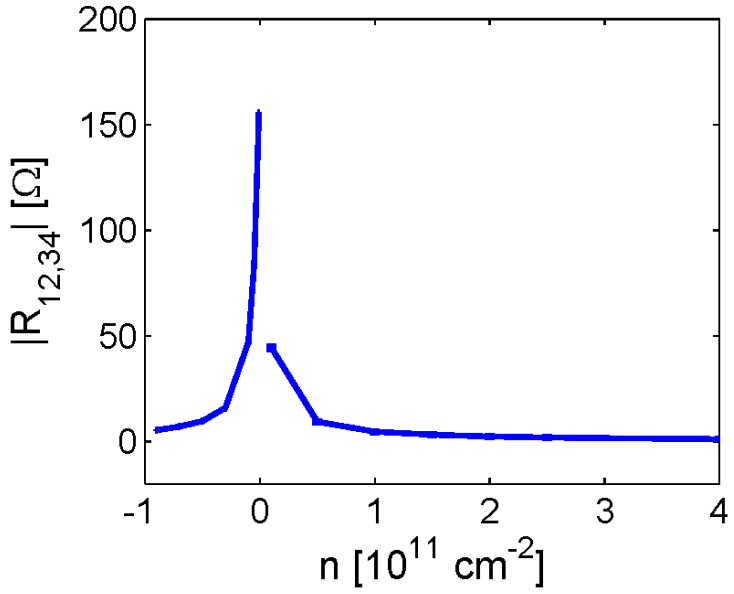

Figure 5.5: Semiclassical Monte Carlo simulation of the nonlocal resistance. Nonlocal resistance signal calculated in the setup of Fig. 5.1 b, as a function of carrier concentration in the metallic detector.

found in the supplementary online material.

The experiments presented in this paper are a first example of how helical edge states can be implemented to quantum transport studies, including semiconductor spintronics and one can envision many further experiments utilizing the concepts presented here.

5.7 Supplementary information for 'Spin polarization of the quantum spin Hall edge states'

In this supplementary information, we present further theoretical results and details of our semiclassical Monte Carlo calculations, additional experimental data for the nonlocal resistance signals in magnetic fields as well as data for structures with different injector sizes. Our supplementary information provides an additional evidence that the quantum spin Hall edge states are spin polarized.

5.7.1 Introduction

This document provides the details of our theoretical approach for the description of the hybrid quantum spin Hall – metallic spin Hall (QSH-SHE) 'H-bar' structures illustrated in Fig. 5.1. More specifically, we calculate the nonlocal four-terminal resistance $R_{12,34}$ in the configuration illustrated in Fig. 5.1 b and Fig. 5.6, where the quantum spin Hall (QSH) insulator state acts as a spin current injector, and the metallic region as a spin current detector through the inverse spin Hall effect (SHE^{-1}). The nonlocal resistance $R_{34,12}$ in the reverse geometry (Fig. 5.1 a), with voltage and current probes exchanged, is the same as $R_{12,34}$ by virtue of the Onsager-Casimir symmetry relations in the absence of a magnetic field (Refs. [43], [55] and Eq. (5.1)). We find a good qualitative agreement between the experimental and theoretical values (Fig. 5.4 and 5.5).

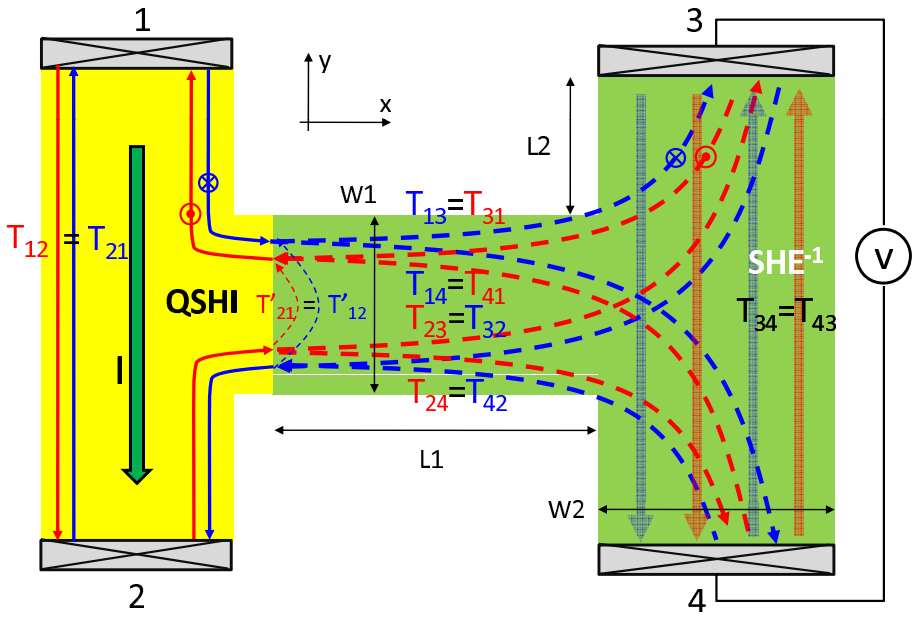

Figure 5.6: Transmission coefficients for Landauer-Büttiker calculation of nonlocal resistance $R_{12,34}$, in the geometry corresponding to the QSH state as spin current injector, with the metallic state exhibiting the SHE^{-1} as a spin current detector (similar to Fig. 5.1 b).

The main idea of our approach is the following. We consider the H-bar geometry illustrated in Fig. 5.6. The yellow region on the left is in the QSH regime, while the green region on the right is in the metallic regime, either n-type or p-type. Figure 5.6 represents the same setup as in Fig. 5.1 b, where L1 corresponds to the length of the part of the structure in the metallic regime.

We calculate the four-terminal nonlocal resistance $R_{12,34} \equiv (V_3 - V_4)/I$ where $I \equiv I_1 =$

$-I_2$ is the current injected into lead 1 and collected in lead 2, and $V_3 - V_4$ is the voltage difference between leads 3 and 4. An expression for $R_{12,34}$ in terms of the transmission coefficients T_{ij} from lead j to lead i, $i, j = 1, \ldots, 4$, can be derived from the multiprobe Landauer-Büttiker formula [43, 55], with $T_{ij} = T_{ji}$ from time-reversal symmetry [77] (TRS). The coefficients $T_{12} = T_{21} = 1$ in the QSH region are universal and are obtained simply by counting the number of edge states leading from one contact to the other [25]. In the same spirit, the coefficients $T_{34} = T_{43}$ can be approximated by counting the number of channels [86] $N_c \simeq k_F W/\pi$ (per spin) in the vertical arm of width $W \equiv \mathrm{W2}$ in the metallic T-structure (Fig. 5.6), with k_F the Fermi wave vector in the metallic region. The nontrivial part of the calculation is to determine the coefficients T_{13}, T_{14}, T_{23} and T_{24} for the transmission between the contacts attached to the QSH region and those attached to the metallic region. Since the right T-structure is metallic, for high enough densities the Fermi wavelength $\lambda_F \ll W$ is much smaller than the dimensions W of the T-structure and a semiclassical approach becomes justified. In other words, there is a large number of channels $N_c \gg 1$ in the metallic region and we can neglect the quantization of motion in the transverse direction.

Our approach for the calculation of $T_{13}, T_{14}, T_{23}, T_{24}$ is based on the Monte Carlo method for the simulation of semiclassical electron transport in semiconductors [87]. This approach has been used successfully for the study of magnetotransport in multiprobe conductors [84, 88, 89, 90], and in particular for the study of quasiballistic transport in HgTe quantum wells [91]. The procedure consists in injecting electrons with well-defined positions and momenta at the left of the metallic T-structure; the QSH edge states then act as 'injectors' of electrons into the metallic region. The electrons then propagate into the ballistic region according to semiclassical equations of motion [85], which include elastic scattering on the geometric boundaries of the T-structure, elastic scattering on nonmagnetic impurities through the inclusion of a phenomenological momentum relaxation time, and more importantly, the effect of spin-orbit coupling through the inclusion of a Berry phase term [85] which acts as a magnetic field in momentum space [85, 65, 92]. This last term is responsible for the SHE and SHE^{-1}. One then simply counts the fraction of electrons which reach contacts 3 and 4, from which the classical transmission probabilities $T_{13}, T_{14}, T_{23}, T_{24}$ can be extracted [84].

This document is structured as follows. In Sec. 5.7.2, we apply the multiprobe Landauer-Büttiker formula [43] to the geometry of Fig. 5.6, and give an explicit expression for the nonlocal resistance $R_{12,34}$ in terms of calculable quantities. In Sec. 5.7.3, we apply

the formalism of Ref. [85] to derive the form of the equations of motion describing carrier propagation in the metallic region, including the important Berry phase term. In Sec. 5.7.4, we give the details of the Monte Carlo algorithm. In Sec. 5.7.5, we present and discuss our numerical results. Finally, in Sec. 5.7.6 we present additional experimental and theoretical results which provide strong evidence that the observed nonlocal signal is a direct consequence of spin-orbit coupling in our samples.

5.7.2 Multiprobe Landauer-Büttiker formalism and nonlocal resistance

For a four-probe phase-coherent device, the nonlocal resistance $R_{12,34}$ is one of several possible four-terminal resistances, whose expressions in terms of transmission coefficients were all worked out long ago by Büttiker [43]. He obtained

$$R_{12,34} \equiv \frac{V_3 - V_4}{I} = \frac{h}{e^2}\frac{T_{31}T_{42} - T_{32}T_{41}}{D}, \tag{S1}$$

at zero temperature, where $I \equiv I_1 = -I_2$ is the current injected at contact 1 and collected at contact 2 (Fig. 5.6), and

$$D \equiv \det \begin{pmatrix} T_{12}+T_{13}+T_{14} & -T_{12} & -T_{13} \\ -T_{31} & -T_{32} & T_{31}+T_{32}+T_{34} \\ -T_{41} & -T_{42} & -T_{43} \end{pmatrix},$$

where $T_{ij} \equiv T_{i \leftarrow j}$ is the transmission probability from lead j to lead i at the Fermi level, and $T_{ij} = T_{ji}$ by TRS in the absence of a magnetic field [77].

From Fig. 5.6, one can read off $T_{12} = 1 + T'_{12}$, where 1 is universal and comes from the edge state propagating directly from contact 1 to contact 2 along the left edge of the QSH T-structure, while T'_{12} is nonuniversal and is the probability of an electron travelling from contact 1 along the top-right edge state of the QSH T-structure, entering the metallic region, propagating inside the metallic region, returning inside the QSH T-structure and propagating to contact 2 via the bottom-right edge state. In fact, T'_{12} corresponds to the probability of interedge tunneling [53], which is negligibly small for a wide enough device. Indeed, Ref. [53] finds that for a device width $\mathrm{W1} \sim 1\,\mu$m (we have $\mathrm{W1} = 0.77\,\mu$m, see Fig. 5.1), the gap Δ opened in the edge state dispersion by interedge tunneling is negligibly small, $\Delta \sim 10^{-7}$ meV. Also, nonlocal resistance mea-

surements (similar to those of Ref. [25]) performed on the actual devices when they are entirely gated into the QSH regime yield the values expected from unperturbed nonlocal edge state transport (see Ref. [25] and Fig. 5.2 b), suggesting that interedge tunneling is negligible. Finally, we have performed fully quantum-mechanical, numerical calculations of the S-matrix of a QSH/metal interface in a strip geometry using the tight-binding version of the four-band effective model for the QSH state in HgTe quantum wells [42], and confirm that T'_{12} is negligible for the sample widths considered here. Therefore we take $T'_{12} = 0$ and $T_{12} = 1$.

The coefficient T_{34} for transmission from contact 3 to contact 4 through the metallic region (Fig. 5.6) is obtained from the semiclassical Monte Carlo calculation as follows. We first calculate $\tilde{T}^{\sigma}_{34}$ and $\tilde{R}^{\sigma}_{3}$ defined as the fraction of electrons of spin $\sigma =\uparrow,\downarrow$ injected from contact 3 that reach contact 4, or that are reflected back into contact 3, respectively. They satisfy $\tilde{R}^{\sigma}_{3} + \tilde{T}^{\sigma}_{34} = 1$ since the metal/QSH interface is modeled as a perfectly reflecting interface and the z component of the spin is conserved in our model (the electron spin is discussed in Sec. 5.7.3 and 5.7.4). However, these coefficients assume only one transport channel (since they sum up to one [55]), and furthermore neglect the probability of being transmitted into the QSH region $T_{31} + T_{32}$. The metallic leads have N_c channels per spin at the Fermi level [86] with $N_c \simeq k_F W/\pi$ and $W \equiv \mathrm{W2}$ the width of the lead (Fig. 5.6). Taking this into account as well as the probabilities T_{31}, T_{32}, the actual transmission and reflection coefficients T^{σ}_{34}, R^{σ}_{3} should satisfy [86] $(T^{\sigma}_{31} + T^{\sigma}_{32}) + T^{\sigma}_{34} + R^{\sigma}_{3} = N_c$. We can thus construct transmission and reflection coefficients satisfying this constraint by defining

$$R^{\sigma}_{3} = \tilde{R}^{\sigma}_{3}[N_c - (T^{\sigma}_{31} + T^{\sigma}_{32})], \tag{S2}$$

$$T^{\sigma}_{34} = \tilde{T}^{\sigma}_{34}[N_c - (T^{\sigma}_{31} + T^{\sigma}_{32})]. \tag{S3}$$

The total transmission coefficient is then given by $T_{34} = \sum_{\sigma=\uparrow,\downarrow} T^{\sigma}_{34}$.

In the Monte Carlo procedure (to be detailed in Sec. 5.7.4), the semiclassical equations of motion, which are first order in time, are integrated numerically, starting from the initial positions and momenta of the charge carriers. In order to obtain the transmission coefficients, we need to perform two separate Monte Carlo calculations. A first calculation, where Fermi surface electrons are injected at the QSH/metal interface and collected at the contacts 3 and 4, yields T_{13}, T_{14}, T_{23} and T_{24}. The problem of the interface between a QSH insulator and a normal metal is nontrivial and has been studied in Ref. [93] using quantum-mechanical scattering theory. In the present work, we use a simpler semiclas-

sical approach. We take for initial conditions at the left of the metallic region a spatially uniform distribution, a fixed wave vector amplitude $k_F = |\mathbf{k}|$ equal to the Fermi wave vector, and an angular distribution given by [84, 86]

$$P(\theta) = \tfrac{1}{2}\cos\theta,\ -\frac{\pi}{2} \leq \theta \leq \frac{\pi}{2},$$

where θ is the angle between the carrier wave vector $\mathbf{k}$ and the the positive x axis (Fig. 5.6), and $\int_{-\pi/2}^{\pi/2} d\theta\, P(\theta) = 1$. The reason we choose a spatially uniform distribution is that although the electrons are injected from the QSH side with wave functions localized along the edge, as soon as they enter the metallic region their wave functions merge into the bulk and their localization length diverges [42]. A second calculation consists in injecting electrons from contact 3 and collecting them at contacts 4 or 3, and yields T_{34} according to Eq. (S3). The angular distribution is again given by $P(\theta) = \frac{1}{2}\cos\theta$, $-\frac{\pi}{2} \leq \theta \leq \frac{\pi}{2}$, but now θ is the angle between the carrier wave vector $\mathbf{k}$ and the the negative y axis (Fig. 5.6). Positionwise, the carriers are again injected uniformly across the width W2 of contact 3 (Fig. 5.6).

5.7.3 Semiclassical equations of motion and Berry phase

In this section we derive the equations of motion which contain the reciprocal magnetic field in momentum space, or Berry phase term [85]. We neglect the bulk inversion asymmetry terms which are a small perturbation [42]. We also neglect interband transitions and study separately the semiclassical dynamics of Kramers partners at the Fermi level in the metallic regime. For either of the n- or p-type regimes we have two degenerate bands that are related by TRS, which means that in our simulation we track the position and momentum of two species of particles denoted by $\uparrow$ and $\downarrow$. The energy of the degenerate conduction bands (n-type) is E_+ and that of the degenerate valence bands (p-type) is E_-.

As before, we use the convention of Ref. [53] for the Hamiltonian. The spectrum consists of two energy eigenvalues,

$$E_\pm(k^2) = \epsilon(k^2) \pm d(k^2), \tag{S4}$$

where $\epsilon(k^2) = -Dk^2$, $d(k^2) = \sqrt{A^2k^2 + M^2(k^2)}$, and $M^2(k^2) = M - Bk^2$. Each

eigenvalue is two-fold degenerate, with eigenstates

$$|u^{\pm}_{\uparrow}(\mathbf{k})\rangle = \left(u^{\pm}_{\uparrow}(\mathbf{k})\right)_1 |\tfrac{1}{2}\rangle + \left(u^{\pm}_{\uparrow}(\mathbf{k})\right)_2 |\tfrac{3}{2}\rangle,$$
$$|u^{\pm}_{\downarrow}(\mathbf{k})\rangle = \hat{T}|u^{\pm}_{\uparrow}(\mathbf{k})\rangle = \left(u^{\pm}_{\uparrow}(\mathbf{k})\right)^*_1 |-\tfrac{1}{2}\rangle + \left(u^{\pm}_{\uparrow}(\mathbf{k})\right)^*_2 |-\tfrac{3}{2}\rangle.$$

The eigenspinors are given by

$$u^{\pm}_{\uparrow}(\mathbf{k}) \equiv \begin{pmatrix} \left(u^{\pm}_{\uparrow}(\mathbf{k})\right)_1 \\ \left(u^{\pm}_{\uparrow}(\mathbf{k})\right)_2 \end{pmatrix} = \frac{1}{\sqrt{A^2k^2 + g^2_{\pm}(k^2)}} \begin{pmatrix} \pm A(k_x - ik_y) \\ g_{\pm}(k^2) \end{pmatrix},$$

and are orthonormal, where $g_{\pm}(k^2) \equiv d(k^2) \mp M(k^2)$. We can now calculate the Berry curvatures for each band [85],

$$\Omega^{\pm,\sigma}_{\alpha\beta}(\mathbf{k}) = -2\,\mathrm{Im}\left\langle \frac{\partial u^{\pm}_{\sigma}(\mathbf{k})}{\partial k_\alpha} \middle| \frac{\partial u^{\pm}_{\sigma}(\mathbf{k})}{\partial k_\beta} \right\rangle, \tag{S5}$$

with $\sigma = \uparrow, \downarrow$ and $\alpha, \beta = x, y$. We however immediately observe that due to TRS, we have

$$\Omega^{\pm,\downarrow}_{\alpha\beta}(\mathbf{k}) = -\Omega^{\pm,\uparrow}_{\alpha\beta}(\mathbf{k}),$$

therefore we only need to calculate the Berry curvature for spin $\uparrow$. Furthermore, $\Omega_{\beta\alpha} = -\Omega_{\alpha\beta}$ is antisymmetric from the definition Eq. (S5). In two dimensions, this antisymmetric tensor has a single component Ω_{xy} and we can define a pseudoscalar

$$\Omega^{\pm}(\mathbf{k}) \equiv \tfrac{1}{2}\epsilon^{\alpha\beta\gamma}\Omega^{\pm,\uparrow}_{\beta\gamma}(\mathbf{k}) = \Omega^{\pm,\uparrow}_{xy}(\mathbf{k}),$$

where $\epsilon^{\alpha\beta\gamma}$ is the Levi-Cività symbol and $\alpha = z$ necessarily. We obtain

$$\Omega^{\pm}(\mathbf{k}) = \Omega^{\pm}(k^2) = -\frac{A^2}{2}\frac{M + Bk^2}{d(k^2)}\frac{A^2k^2 \mp 2g_{\pm}(k^2)M(k^2)}{[A^2k^2 \mp g_{\pm}(k^2)M(k^2)]^2}.$$

Note that the physical units of the quantities A, k, Ω are given by $[A] = \mathrm{eV}\cdot\text{Å}$ and $[k] = \text{Å}^{-1}$, hence $[\Omega] = \text{Å}^2$. The anomalous or Hall velocities are given by [85]

$$\begin{aligned} \hbar\delta\dot{x}^{\pm}_{\sigma} &= -\hbar\Omega^{\pm,\sigma}_{xy}\dot{k}^{\pm}_{y,\sigma} = -\sigma\hbar\Omega^{\pm}\dot{k}^{\pm}_{y,\sigma}, \\ \hbar\delta\dot{y}^{\pm}_{\sigma} &= -\hbar\Omega^{\pm,\sigma}_{yx}\dot{k}^{\pm}_{x,\sigma} = \sigma\hbar\Omega^{\pm}\dot{k}^{\pm}_{x,\sigma}, \end{aligned}$$

with $\sigma = \pm 1$. Since the bands are doubly degenerate, the normal velocity is independent

of spin and is simply given by

$$\hbar \mathbf{v}_{\pm} \equiv \alpha_{\pm}(k^2)\mathbf{k} \text{ with } \alpha_{\pm}(k^2) \equiv -2D \pm \frac{A^2 - 2BM(k^2)}{d(k^2)},$$

where $[\alpha] = \mathrm{eV}{\cdot}\text{Å}^2$. The semiclassical equations of motion finally take the form

$$\hbar \dot{x}_{\sigma}^{\pm} = \alpha_{\pm}((\mathbf{k}_{\sigma}^{\pm})^2)k_{x,\sigma}^{\pm} - \sigma\hbar\Omega^{\pm}((\mathbf{k}_{\sigma}^{\pm})^2)\dot{k}_{y,\sigma}^{\pm}, \tag{S6}$$

$$\hbar \dot{y}_{\sigma}^{\pm} = \alpha_{\pm}((\mathbf{k}_{\sigma}^{\pm})^2)k_{y,\sigma}^{\pm} + \sigma\hbar\Omega^{\pm}((\mathbf{k}_{\sigma}^{\pm})^2)\dot{k}_{x,\sigma}^{\pm}, \tag{S7}$$

$$\hbar \dot{k}_{x,\sigma}^{\pm} = F_x^{\mathrm{coll}}(\mathbf{r}_{\sigma}^{\pm}, \mathbf{k}_{\sigma}^{\pm}, t), \tag{S8}$$

$$\hbar \dot{k}_{y,\sigma}^{\pm} = F_y^{\mathrm{coll}}(\mathbf{r}_{\sigma}^{\pm}, \mathbf{k}_{\sigma}^{\pm}, t), \tag{S9}$$

where $[\hbar\dot{\mathbf{r}}] = \mathrm{eV}{\cdot}\text{Å}$, and $\mathbf{F}^{\mathrm{coll}}$ is the force exerted on the particles due to collisions with the geometric boundaries of the sample and with impurities in the sample. The specific form of this term is detailed in Sec. 5.7.4.

5.7.4 Semiclassical Monte Carlo algorithm

For simplicity, we assume that the probability of reflecting into a state with opposite spin is very small, so that we are effectively simulating the semiclassical dynamics of a two-component gas, with the two components evolving in a perfectly independent manner.

The collision force is given by $\mathbf{F}^{\mathrm{coll}} = \mathbf{F}^{\partial S} + \mathbf{F}^{\mathrm{imp}}$ where $\mathbf{F}^{\partial S}$ is the force due to collision on the sample boundary (denoted by ∂S), and $\mathbf{F}^{\mathrm{imp}}$ is the force due to collisions on impurities. The effect of $\mathbf{F}^{\partial S}$ on a particle is implemented into the simulation as follows: by energy and momentum conservation, when a particle hits a boundary we simply flip the sign of the component of its momentum normal to the boundary (specular reflection). On the other hand, to take the effect of $\mathbf{F}^{\mathrm{imp}}$ into account we proceed as follows. We first generate a random free flight time [87] t_{free} from an exponential distribution

$$P(t_{\mathrm{free}}) = \frac{1}{\tau} e^{-t_{\mathrm{free}}/\tau},$$

where τ is a phenomenological collision time. We expect the metallic region to be in the quasi-ballistic regime [52] and thus consider that collisions are dominated by boundary scattering. Therefore, we choose $\tau > \tau_{\partial S}$ where $\tau_{\partial S} \sim L/v_F$ is the boundary scattering time with L the characteristic linear size of the device and v_F the Fermi velocity. The

impurity-free equations of motion, i.e. Eqs (S6)-(S9) with $\mathbf{F}^{\rm imp} = 0$, are then solved numerically for a time $t_{\rm free}$. At the end of the free flight time, we randomize the momentum of the particle (only the direction $\hat{k} = \mathbf{k}/|\mathbf{k}|$ as the magnitude $|\mathbf{k}| = k_F$ is fixed by energy conservation) according to an uniform angular distribution between 0 and 2π. This is meant to simulate isotropic scattering from rotationally invariant impurities. Finally, a new random free flight time is generated, and the procedure starts again until all particles have exited the device through either contact 3 or 4.

Since $\hbar\dot{\mathbf{k}}_\sigma^\pm = 0$ apart from boundary and impurity scattering, the Berry phase term vanishes for free propagation inside the boundaries and the semiclassical trajectories between collisions are simply straight lines. The Berry phase term generates a shift of position upon scattering on boundaries and impurities, an effect similar to the side-jump effect [94] in the anomalous Hall effect, with the exception that here the spin-orbit coupling is intrinsic (arising from the bandstructure) and not the spin-orbit coupling arising from impurity potentials. A scattering event resulting in a change of momentum $\Delta\mathbf{k}$ produces a position shift $\Delta\mathbf{r}$ given by

$$\begin{aligned}\Delta x_\sigma^\pm &= -\sigma\Omega^\pm((\mathbf{k}_\sigma^\pm)^2)\Delta k_{y,\sigma}^\pm,\\ \Delta y_\sigma^\pm &= \sigma\Omega^\pm((\mathbf{k}_\sigma^\pm)^2)\Delta k_{x,\sigma}^\pm,\end{aligned}$$

which can also be written

$$\Delta\mathbf{r}_\sigma^\pm = -\sigma\mathbf{\Omega}^\pm((\mathbf{k}_\sigma^\pm)^2)\times\Delta\mathbf{k}_\sigma^\pm, \tag{S10}$$

where $\mathbf{\Omega}^\pm \equiv \Omega^\pm\hat{\mathbf{z}}$ and $\Delta\mathbf{k}_\sigma^\pm$ depends on the boundary. Equation (S10) makes explicit the interpretation of the Berry curvature $\mathbf{\Omega}^\pm$ as a magnetic field in momentum space. Since $\Delta\mathbf{k}_\sigma^\pm$ is normal to the boundary for specular reflection, the position shift $\Delta\mathbf{r}_\sigma^\pm$ will be along the tangent to the boundary. For free propagation inside the boundaries, we have

$$\Delta\mathbf{r}_\sigma^\pm = \alpha_\pm((\mathbf{k}_\sigma^\pm)^2)\mathbf{k}_\sigma^\pm\frac{\Delta t}{\hbar},$$

where $[\frac{\Delta t}{\hbar}] = \mathrm{eV}^{-1}$, and Δt is the time between two collision events (impurity or boundary). Furthermore, since we are doing a Monte Carlo simulation we need to average over a large number of particles. We find that we get reasonably good statistics (error bars not too large) for $\sim 10^6$ particles.

5.7.5 Numerical results

We have performed the calculations for HgTe/HgCdTe quantum wells [42] of thickness $d = 89.9$ Å and device size (see Fig. 5.6) $\mathrm{L1} = 0.2$ μm, $\mathrm{W1} = 0.77$ μm, $\mathrm{W2} = 0.8$ μm and $\mathrm{L2} = 1.665$ Å (such that the distance between contacts 3 and 4 is 4.1 μm). These dimensions correspond to those of the device discussed above (Fig. 5.1). Note that although the length of the middle segment of the H-bar is 0.7 μm (Fig. 5.1), the actual length $\mathrm{L1}$ of the QSH injector region (yellow region in Fig. 5.1) is estimated as 0.2 μm. To avoid unphysical geometric resonances [84, 89], we consider that the corners of the T-structure are rounded, with radius of curvature $R = 100$ Å. For the devices studied in this work, the Dirac mass M (see Sec. 5.7.3) is estimated as $|M| = -6$ meV due to the small gap between the $H1$ and $H2$ subbands which are the lowest energy subbands for the quantum well thicknesses considered.

The results are plotted in Fig. 5.5. The calculated nonlocal signal is in good qualitative agreement with the experimental results of Fig. 5.3 and 5.4, with $R_{12,34} \sim 10^2\,\Omega$ in the p-type regime and $R_{12,34} \sim 10\,\Omega$ in the n-type regime. Since we are performing a semiclassical simulation for the detector region, we cannot simulate the transition through the insulating gap, since as the Fermi level approaches the gap, the density reaches a point where our semiclassical approximation $k_F W/\pi \gg 1$ breaks down. Although the qualitative agreement with experiment is good, we observe that the experimental signal is larger. We expect that the discrepancy is due to the additional contribution from Rashba spin-orbit coupling [83], which is not taken into account in the simple semiclassical approach with S_z conservation used in this work.

The increase of the nonlocal resistance signal with decreasing density (Fig. 5.5) is evidence that the signal is generated by the spin-orbit interaction, i.e. the Berry curvature term (Sec. 5.7.3). This can be understood if one remembers that the Berry curvature can be treated approximately as the magnetic field in reciprocal space of a magnetic monopole [65, 92] centered at $\mathbf{k} = 0$. As the density is reduced (decreasing $\mathbf{k}$), the particles are closer to the monopole and feel a stronger Berry magnetic field. Furthermore, due to the larger effective mass for holes (p-type) than for electrons (n-type) in our structures [52], for comparable densities the Fermi wave vector will be smaller for holes than for electrons, yielding a larger Berry phase effect in the p-regime as compared to the n-regime.

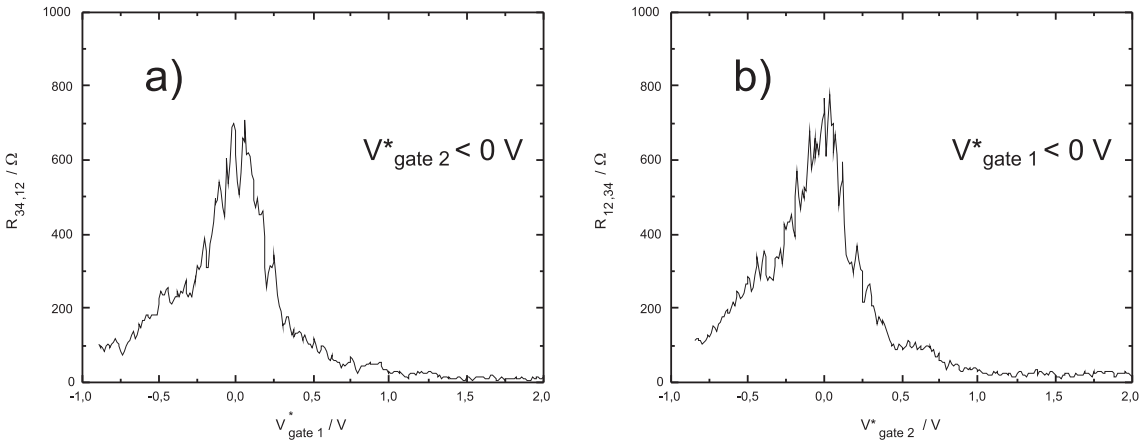

Figure 5.7: Nonlocal resistance signal for injector in the p-type regime, as a function of gate voltage in the detector and injector length: a) short p-type injector (200 nm); b) long p-type injector (400 nm). By Onsager-Casimir reciprocity, for the detector in the QSH insulating regime ($V^*_{\rm gate} \sim 0$) this is equivalent to the configuration of Fig. 5.6 with $L1 = 200$ nm in a) and $L1 = 400$ nm in b).

5.7.6 Additional experimental and theoretical evidence for spin-orbit origin of observed effects

We now present additional experimental and theoretical evidence that the observed nonlocal resistance signal is due to the spin-orbit interaction and not by some spurious effects. In Fig. 5.7, we plot the nonlocal resistance as a function of gate voltage for shorter (Fig. 5.7a, 200 nm) and longer (Fig. 5.7b, 400 nm) injector sizes. The sample parameters are the same as above. Although the data in Fig. 5.7 corresponds to a metallic (p-type) injector, for $V^*_{\rm gate} \sim 0$ in the detector (QSH insulating regime) the configuration is equivalent to that illustrated in Fig. 5.6, by Onsager-Casimir reciprocity (see Eq. (5.1)). In our calculation, therefore, we can compare theoretical results for $L1 = 200$ nm and $L1 = 400$ nm with the data in Fig. 5.7a) and b), respectively.

One can see in Fig. 5.7 that the nonlocal resistance is essentially independent of the injector length. The maximum signal is obtained when the detector is in the QSH insulator regime, as expected from previous nonlocal transport measurements in the QSH regime [25]. In the diffusive regime, we expect that a nonlocal resistance signal originating from spin effects would depend strongly on the system size. By a solution of the Poisson equation in the metallic T-structure we estimate that the stray diffusive signal for an Ohmic conductor doubles when the metallic leg of the injector is reduced by half. Therefore, a very weak dependence of the experimental nonlocal resistance on the injector length

excludes the possibility that our result is a diffusive stray signal and constitutes evidence that our samples are in the quasi-ballistic regime.

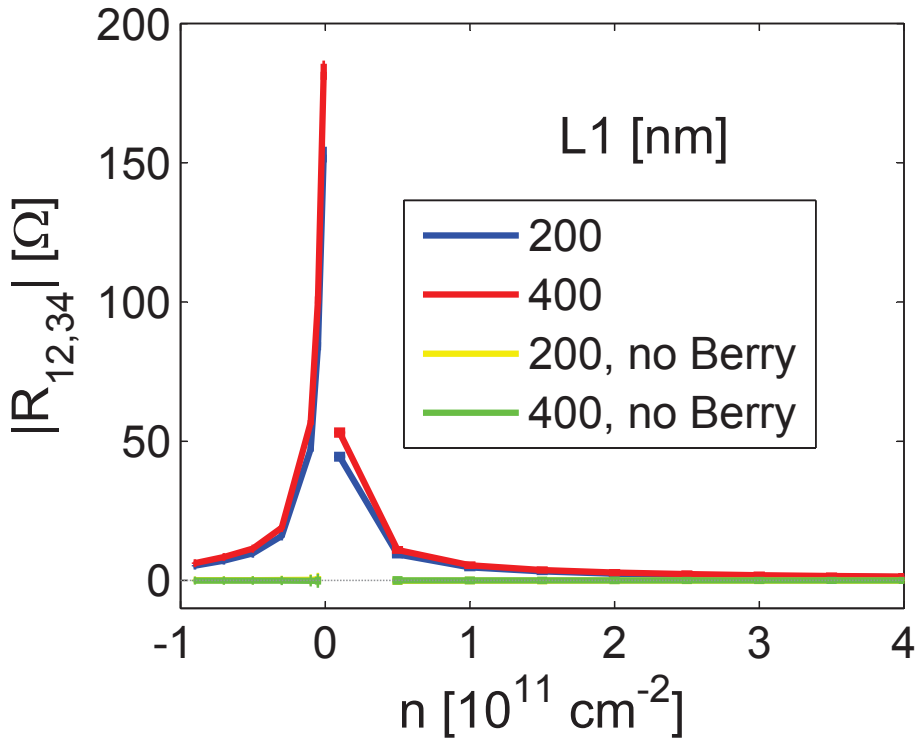

Figure 5.8: Effect of the detector size $L1$ (geometry of Fig. 5.6, equivalent by Onsager-Casimir reciprocity to Fig. 5.7) and Berry phase term on the nonlocal resistance. The dotted gray line denotes zero. The signal is essentially independent of $L1$, in agreement with experiment (Fig. 5.7). Furthermore, the signal is essentially zero in absence of the Berry phase term.

We now provide further theoretical evidence that our signal originates solely from the presence of strong spin-orbit interaction effects, i.e. the Berry phase term (Sec. 5.7.3). Fig. 5.8 shows the theoretically predicted nonlocal signal in the geometry of Fig. 5.6. As mentioned previously, this configuration is equivalent to that of Fig. 5.7 by Onsager-Casimir reciprocity. First, the nonlocal resistance exhibits almost no size dependence as observed experimentally (Fig. 5.7). Since we have chosen the bulk impurity scattering time τ to be larger than the boundary scattering time $\tau_{\partial S}$, the agreement between the theoretical and experimental results constitutes strong evidence that our samples are in the quasi-ballistic regime. Second, the nonlocal resistance signal is negligible in the absence of the Berry phase effect. Since the Berry phase term is a direct consequence of the intrinsic spin-orbit interaction (Sec. 5.7.3), we conclude that the observed signal is chiefly due to the intrinsic SHE. The samples were symmetrically doped and therefore designed

the way so the Rashba term originating from the applied gate was minimal. However, as mentioned previously, we expect the Rashba spin-orbit interaction [83] could also play some role for a non-zero external gate potential, which might account for the discrepancy between our simple theory and the experiment in the magnitude of the signal. We believe that our supplementary experimental and theoretical results provide strong evidence that we have detected the helical nature of the QSH edge states via the SHE^{-1}, and used the QSH helical edge states to convert the SHE into a charge signal.

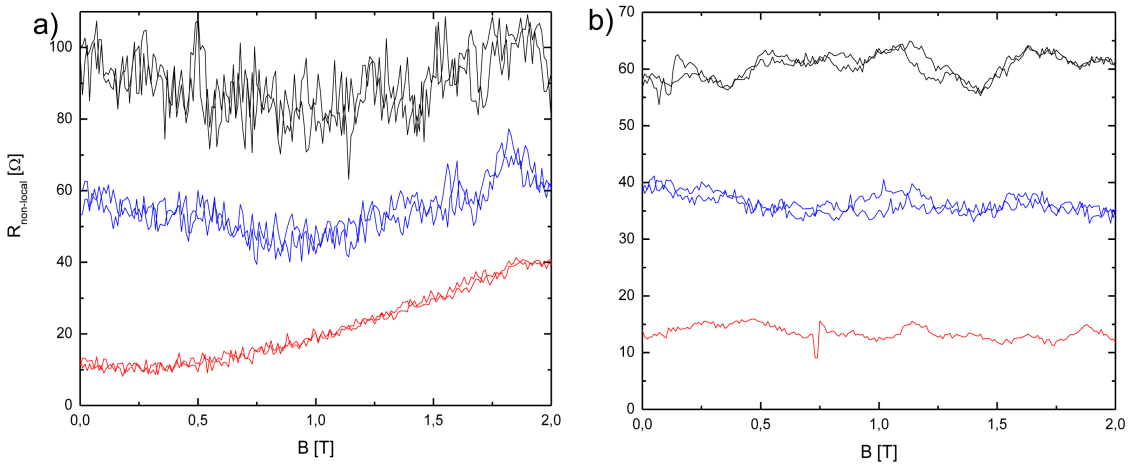

Figure 5.9: Non-local resistance signals in perpendicular (a) and parallel (b) magnetic fields. Black (blue) traces correspond to the injection of a spin current via the SHE (the QSH state) and detection of the signal by the QSH (the SHE^{-1}), respectively. Red traces correspond to a control experiment where both gated regions are in the n-conducting metallic state (the SHE acts as an injector while the SHE^{-1} as a detector).

5.7.7 Non-local resistance signals in magnetic fields

We have performed additional measurements to observe the evolution of the non-local resistance signals in magnetic fields. These measurements have been carried out in a similar manner as the two configurations presented above: In configuration 1 the injection of a spin current is realized via the SHE and detected by the QSH insulator (see Fig. 5.1 a) while in configuration 2 the injection is performed through the QSH state and the detection by the inverse spin Hall effect, SHE^{-1} (see Fig. 5.1 b). As described above, the Fermi level in the relevant parts of the sample is fixed by adjusting the relevant gate voltage. Additionally, as a control experiment, we have measured the magnetic field dependence of a non-local signal in a configuration where both regions are in the n-type conducting metallic state. Fig. 5.9a shows the obtained traces for magnetic fields perpendicular to

the 2DEG. The non local signals for the SHE injection (black) and the QSH injection (blue) show a clear decrease between 0 and 1 T, followed by an increase above 1 T. The constant shift between QSH/SHE$^{-}1$ and SHE/QSH curves in the magnetic field is caused by a slight difference in the initial carrier densities under the two gated regions due to a random hysteresis in the gate voltage behavior. The control measurement where all parts of the sample are n-type conducting and the SHE is detected by the SHE^{-1} is presented in red. When both regions are n-type conducting, the detected spin signal is small and hardly depends on magnetic field up to 1 T. Therefore we interpret the decrease of the signal in magnetic fields in the QSH/SHE^{-1} and SHE/QSH configurations as resulting from the decay of the spin polarization of the helical edge states. Indeed, the degree of spin polarization of the helical edge states can be significantly reduced in a transverse field by spin-orbit effects, bulk inversion terms, and the presence of metallic puddles in the mesa due to inhomogeneous gating [25, 95, 96]. As discussed by us previously [95], a strong perpendicular magnetic field (strong compared with the band gap) renders the dispersion of the edge states nonlinear and the group velocity of one of the helical edge states tends to zero. Roughly speaking, such a slowly moving helical edge state will interact more effectively with the electron puddles, leading to significant decay of spin polarization, even in the quasi-ballistic regime relevant to the present experiments. At perpendicular magnetic fields above 1 T, the non-local resistance signal increases for all three configurations. We attribute this increase to the onset of the quantum Hall edge channel transport which is superimposed on the spin-related signal from the SHE^{-1} and the QSH state.

Fig. 5.9b shows the behavior of the non-local resistance signals in parallel magnetic fields. In this configuration, the non-local resistance signals are independent of magnetic field strength. Because of the selection rules for zincblende-type systems, an in-plane magnetic field induces only a small (second order) Zeeman coupling and is much less effective in reducing the spin-polarization of the edge states than a perpendicular field of similar strength.

We conclude that the observed behavior of the device in magnetic fields is consistent with and yields additional independent evidence of the spin polarization of the helical edge states in our experiments.

Chapter 6

Quantum Hall Effect from the Topological Surface States of Strained Bulk HgTe

This chapter is based on the publication: *C. Brüne, C.X. Liu, E.G. Novik, E.M. Hankiewicz, H. Buhmann, Y.L. Chen, X.L. Qi, Z.X. Shen, S.C. Zhang and L.W. Molenkamp, 'Quantum Hall Effect from the Topological Surface States of Strained Bulk HgTe', Physical Review Letters* ***106****, 126803, 2011.*

6.1 Abstract

We report transport studies on a three dimensional, 70 nm thick HgTe layer, which is strained by epitaxial growth on a CdTe substrate. The strain induces a band gap in the otherwise semi-metallic HgTe, which thus becomes a three dimensional topological insulator. Contributions from residual bulk carriers to the transport properties of the gapped HgTe layer are negligible at mK temperatures. As a result, the sample exhibits a quantized Hall effect that results from the 2D single cone Dirac-like topological surface states.

6.2 Introduction

The discovery of two (2D) and three dimensional (3D) topological insulators (TI) [7, 6, 8, 32, 9, 10, 12, 97, 14, 15] has generated strong activity in the condensed matter physics community [18, 98]. Current research on 3D TIs is mostly focused on Bi_2Te_3, Bi_2Se_3 and Sb_2Te_3 compounds [97, 14, 15] due to their simple Dirac-like surface states, which have been observed by angle resolved photoemission spectroscopy (ARPES) and scanning tunneling microscopy [18]. However, these compounds show strong defect doping and low carrier mobility, and the observation of surface charge transport is obscured by the bulk conductivity. Many of the predicted novel properties of a 3D TI, such as the quantized magneto-electric effect [59, 54] and the surface Majorana fermions [99], can only be observed when bulk carriers are negligible compared to the surface states. Experimentally reaching the intrinsic TI regime, where bulk carriers are absent, is now the central focus of the field.

The two dimensional TI state was first predicted and observed in 2D HgTe quantum wells (QW) [7, 8], and non-local transport measurements demonstrate edge state transport without any contributions from 2D bulk carriers. [25] 3D HgTe is a semi-metal which is charge-neutral when the Fermi energy is at the touching point between the light-hole and heavy-hole Γ_8 bands at the Brillouin zone center. A unique property of the band structure of HgTe is the energetic inversion of the Γ_6 and Γ_8 band ordering, which is the origin of the quantum spin Hall effect in 2D HgTe/CdTe QWs [8]. Due to the band inversion, 3D HgTe is also expected to have Dirac-like surface states [100, 101], but since the material is semi-metallic, this state is always coupled to metallic bulk states. With applied strain, a gap opens up between the light-hole and heavy-hole bands, so that strained 3D HgTe is expected to be a 3D TI [40, 32]. In this paper we demonstrate experimentally that a gap opens up in in-plane strained 3D HgTe bulk layers grown by molecular beam epitaxy (MBE), and we reach the much sought after intrinsic TI regime in a material with negligible bulk carriers. In this regime, the Hall effect of the 3D HgTe bulk layer is quantized, due to the contributions from the surface states only. Theoretical considerations are in agreement with the experimental results and confirm the transport through 2D surface states with Dirac type dispersion.

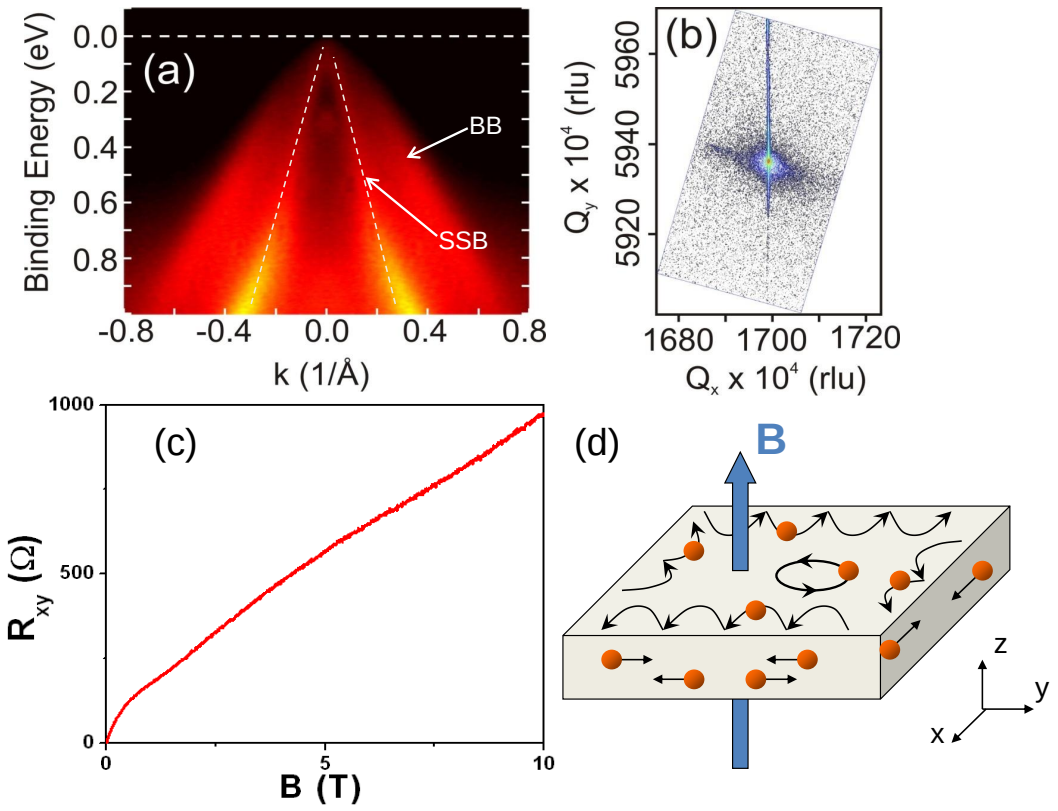

Figure 6.1: Supporting characterization experiments. (a) ARPES measurements on a relaxed, 1 μm thick HgTe sample. The dispersion of the surface state (SSB) and bulk bands (BB) are indicated by the arrows; (b) Reciprocal space map in the region of the [115] reflex of the 70 nm thick HgTe sample demonstrating that the epilayer is coherently strained; (c) Hall resistance as a function of magnetic field of the semi-metallic 1 μm thick sample ; (d) Schematic picture of the coexistence of the chiral edge states from the upper and lower surfaces and the non-chiral metallic modes at the side surfaces. The magnetic field is perpendicular to the upper and lower surfaces, but parallel to the four side surfaces.

6.3 Existence of the surface states and band gap in 3D HgTe.

HgTe bulk samples have been grown by MBE on CdTe subtrates, which have a lattice constant that is 0.3 % larger than that of bulk HgTe (0.646 nm). At this mismatch, the critical thickness for lattice relaxation is around 200 nm, implying that for thinner HgTe the epilayer adopts the lateral lattice constant of the substrate, while in thicker layers the strain is relaxed by the formation of dislocations.

To provide evidence for the occurrence of the topological surface state, we first show an ARPES measurement on a 1 μm thick HgTe layer in [Fig. 6.1 a)]. In this layer, the lattice strain is fully relaxed, and the surface has the lattice constant of unstrained bulk material. The figure clearly shows the presence of the predominantly linearly dispersing surface state band (SSB), coexisting with bulk bands (BBs) (more data on these assignments can be found in the supplementary material). According to the theoretical analysis in Ref. [40], the surface states originate from the inversion between the Γ_8 light-hole and Γ_6 electron bands, while the bulk bands, which appear nearly at the same energy range with the surface states, correspond to the Γ_8 heavy-hole band.

Since the relaxed sample is a semi-metal and thus not a TI in the strict sense, we have grown a thinner sample, which is only 70 nm thick, thin enough for the epitaxial strain due to the lattice mismatch with the substrate to coherently strain the sample, thus opening up a bulk insulating gap. Fig. 6.1 b) shows a high resolution X-ray diffraction map of the [115] reflex of this sample in units of reciprocal lattice space vectors. The bright spot in the center of this graph is the reflex from the substrate, while the thin vertical line stems from the HgTe epilayer. The absence of any relaxation of the reciprocal lattice vector $\mathbf{Q_x}$ for the epilayer is direct evidence that this sample is fully strained. [102] The deformation potentials of (Hg,Cd)Te have been reported in the literature [103]; using these values and the 0.3 % lattice mismatch we calculate an energy gap of the order of $\sim$ 22 meV for fully strained HgTe on CdTe, using an eight band k·p model [39]. We believe this energy gap to be the optimal gap value that can be obtained in HgTe. In principle substrates with a larger lattice mismatch would induce a larger gap, however, these are not readily available. In addition larger strain would also reduce the maximum thickness the HgTe layer can sustain without strain relaxation.

For transport experiments, we have subsequently patterned parts of both wafers into Hall-

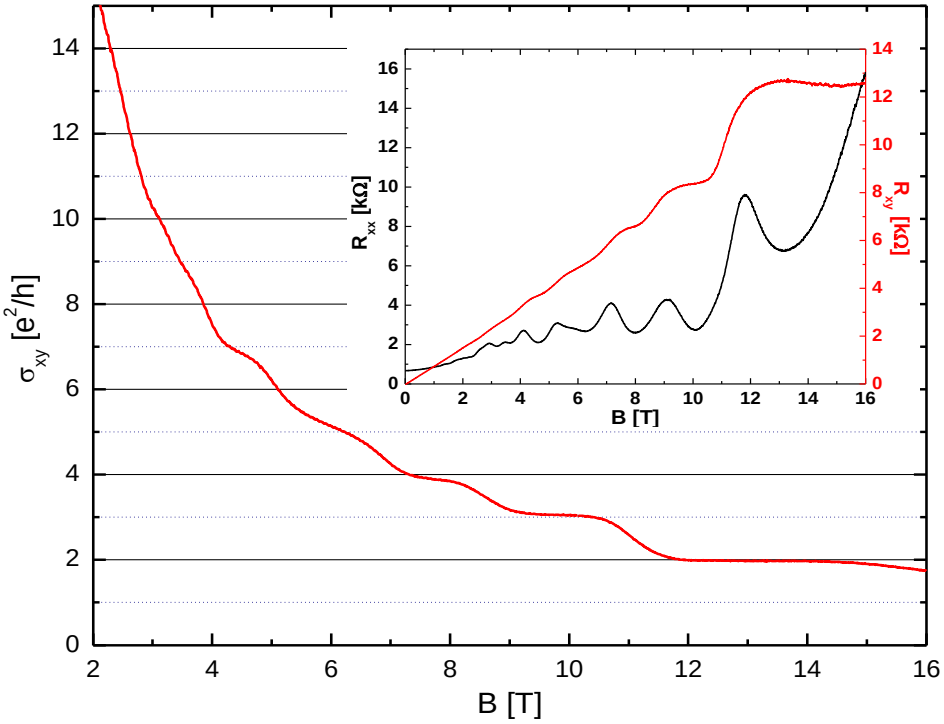

Figure 6.2: Transport data on the strain-gapped 70 nm thick HgTe sample. The Hall conductivity of the 70 nm thick HgTe sample measured at 50 mK shows plateaus at the quantized values. The inset shows the Hall resistance R_{xy}, together with the longitudinal resistance R_{xx}.

geometry devices with a mesa of 200 μm width and 600 μm length, using argon ion etching. The magneto transport of the samples has been investigated at a base temperature of 50 mK, in magnetic fields up to 16 T. In the 1 μm thick sample, the Hall data indicates that bulk conductance dominates the transport. Fig. 6.1 c) shows that for this sample we observe a non-monotonic dependence of the Hall voltage, which is characteristic for the multi-carrier transport expected from a semi-metal. Much more interesting behavior is observed for the 70 nm-thick sample, of which the longitudinal and Hall resistance are shown in the inset of Fig. 6.2. From the low field data, the electron mobility can be extracted, and estimated as 34000 $cm^2/(V{\cdot}s)$, which is significantly higher than that observed in Bi_2Se_3 and Bi_2Te_3 [57, 58]. At high magnetic fields, the longitudinal and Hall resistance exhibit distinct features which are characteristic for a 2D electron system (2DES): the Hall resistance R_{xy} shows plateaus at the same magnetic fields where the longitudinal resistance R_{xx} develops a minimum (inset of Fig. 6.2). Additionally, the Hall resistance R_{xy} shows the expected 2D quantized plateau values, which become clearer in a conductivity plot (Fig. 6.2).

Compared with the quantum Hall effect of an ordinary 2DES, two unusual observations should be emphasized, which indicate that the observed quantum Hall plateaus indeed result from the Dirac-type dispersion of the topological surface states. First, at low magnetic fields, a sequence of Hall plateaus develops with odd filling factors, ν = 9, 7, and 5, before at higher field the sequence is continued with ν = 4, 3, and 2. The occurrence of odd-number filling factors at low magnetic field indicates the presence of a zero mode (a Landau level at zero energy) due to the linear dispersion of Dirac fermions, as has also been found in graphene [17] and in HgTe/CdTe QWs with a critical thickness of 6.3 nm [29]. A 70 nm thick layer can safely be regarded as a 3D material; the confinement energies of bulk carriers are sufficiently small that Hall quantization effects would be washed out by multi-subband averaging. We thus assume that the Hall plateaus result from the topological surface states, and use a model with two Dirac cones, one on the top (vacuum) and one on the bottom (CdTe interface) to describe the system (see additional online material for details). Because massless Dirac fermions in a magnetic field always exhibit a zero mode, the Hall conductance of a single Dirac cone is given by $\sigma_{xy} = (n + \frac{1}{2})e^2/h$, where $n = n_t$ or $n = n_b$ (for the top and bottom surfaces, respectively) is always an integer [32, 59]. The fractional factor of $\frac{1}{2}$ in the Hall conductance σ_{xy} is a consequence of the quantized bulk topological term in the electromagnetic action [59], and is independent of the microscopic details. When top and the bottom surface have the same filling factor, *i.e.* $n = n_t = n_b$, the total Hall conductance is given by $\sigma_{xy}^T = (2n + 1)e^2/h$.

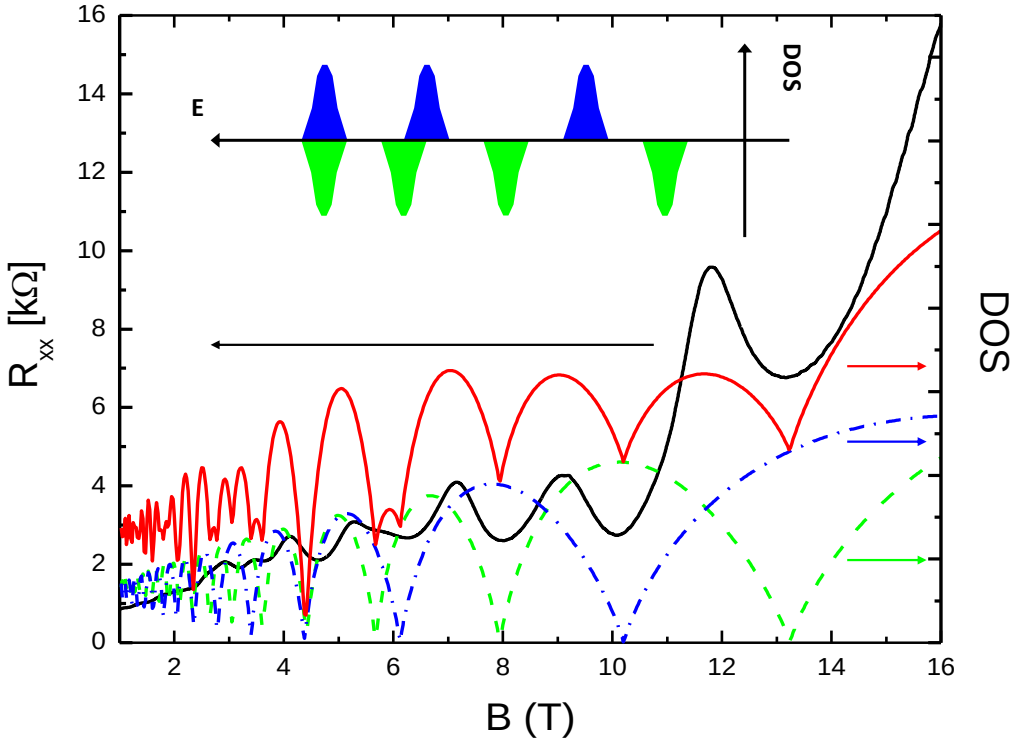

Figure 6.3: Comparison between the calculated density of states (DOS) and the measured Shubnikov- de Haas oscillations. The DOS are calculated for a two Dirac cones model for the surface states with one Dirac cone (at the CdTe interface) having a carrier density $3.7 \times 10^{11}\text{cm}^{-2}$ (blue dashed-dotted line) and the other (the surface facing vacuum) $4.8 \times 10^{11}\text{cm}^{-2}$ (green dashed line). The sum of the DOS for the two Dirac cones (red line) compares well with the measured longitudinal resistance R_{xx} (black line). The inset shows the Landau ladders of the Dirac fermions on both surfaces.

Therefore, within the two Dirac cone model, the odd filling factor at low magnetic fields can be naturally explained assuming both surfaces have the same density. The appearance of an even filling factor at high magnetic field indicates that the degeneracy is removed. In an ordinary 2D electron gas, such a lift of degeneracy usually occurs due to Zeeman coupling. However, Zeeman coupling cannot lift the degeneracy in inversion symmetric Dirac cones on the top and bottom surface of a topological insulator. As we explain in the supplementary material, this is because the inversion symmetry is preserved by the magnetic field. The Landau levels from the top and bottom surface states will remain degenerate as long as the hybridization between the two surface states is negligible. For a thickness of 70 nm, hybridization between the top and bottom surfaces can be neglected since the surface state width is around 2$\sim$3 nm. Thus we conclude that the inversion sym-

metry breaking is necessary for the explanation of the Landau level splitting. In practice, the different electrostatic environments of both surfaces break the inversion symmetry and lead to different densities at both surfaces. This then leads to different Landau filling factors for the top and bottom surfaces at high magnetic fields, and the visibility of even filling factors at high fields results from the increased energy splitting between adjacent Landau levels at lower filling factors in a Dirac system, as schematically indicated in the inset of Fig. 6.3. A calculation of the density of states in a magnetic field from a two Dirac cones model with an inversion breaking term indeed agrees well with the minima of the Shubnikov-de Haas oscillation, as shown in Fig. 6.3 (see additional online material for details). From the fit, we obtain very reasonable carrier densities of 3.7×10^{11}cm^{-2} for the bottom (CdTe interface) and 4.8×10^{11}cm^{-2} for the top surfaces, respectively. We note that the carrier densities found here also imply we can neglect any effects from bulk carriers - if the amount carriers found here would be evenly distributed over the 70 nm slab this would result in an overall 2D density of $\sim 10^{10} cm^{-2}$, yielding a very different quantum Hall behavior.

The second observation is that the minima in R_{xx} do not approach zero even at the highest magnetic fields although the Hall resistance is quantized and the plateaus have the expected resistance value. This indicates that besides the chiral edge modes from the quantum Hall effect, there are other modes contributing to the longitudinal, but not the Hall transport. A plausible candidate are the metallic states at the side surfaces [60]. While the above two Dirac cone model only takes the top and bottom surfaces explicitly into account, the topological surface states also occur on the four side surfaces, which see a parallel, rather than perpendicular, magnetic field. Consequently, at the side surfaces the Dirac points are not gapped, but only shifted by the applied magnetic field. Thus, the surface states at the side surfaces will remain metallic in magnetic field and coexist with the chiral edge states, as shown schematically in Fig. 6.1 d). This provides a backscattering mechanism when the transport on the top and bottom surfaces is in the quantum Hall regime [60]. A more systematic study of the influence of the residual bulk conductivity and side surface states is required to fully understand the quantitative behavior of R_{xx} and R_{xy}, which is beyond the scope of the present letter.

6.4 Conclusion.

In summary, we have experimentally reached the much sought after regime of the intrinsic 3D topological insulator with negligible bulk carriers, in an epitaxially strained 3D HgTe sample. Our observation of a quantized Hall conductance in a 3D sample conclusively demonstrates a key feature of 3D topological insulators. A simple model with two Dirac cones is proposed to understand the most salient features of the transport measurement qualitatively. The quality of our sample should be sufficient to observe the quantized topological magneto-electric effect [59], and directly determine the 3D topological invariant experimentally.

6.5 Supplementary material for "Quantum Hall Effect from the Topological Surface States of Strained Bulk HgTe"

6.5.1 Details of the ARPES Experiment

Angle resolved photoemission spectroscopy (ARPES) experiments on $1\mu m$ thick HgTe thin film (grown on CdTe substrate) were performed at Beamline 10.0.1 of the Advanced Light Source (ALS). During the experiments, the measurement chamber pressure was kept $< 4 \times 10^{-11}$ Torr, and data were recorded by a Scienta R4000 analyzers at 15 K sample temperature. The photon energy used was 65 eV and the total convolved energy and angle resolutions were 20 meV and 0.2 degree, respectively. The fresh surface for ARPES measurement was obtained by gently sputtering the HgTe (001) surface with Ar ion-beam, and no observable surface degradation was noticed during typical experimental period (12 hrs). We also measured the photon energy dependent (65-70eV) band dispersion of HgTe, as shown in Fig. 6.4. For all measurements at different energies, the surface state band can clearly be observed, superimposed on a blurry background of bulk bands. The shape and dispersion of the band do not vary with photon energy, while its intensity may vary. This is direct evidence that the feature does not have k_z dispersion, as expected from a two dimensional (surface) state. We note that at the vicinity of the Gamma point, the surface state has gained finite curvature, similar to that observed[14, 104] in Bi_2Se_3. The difference between the HgTe and the Bi2Se3 cases is that for the latter, both the up-

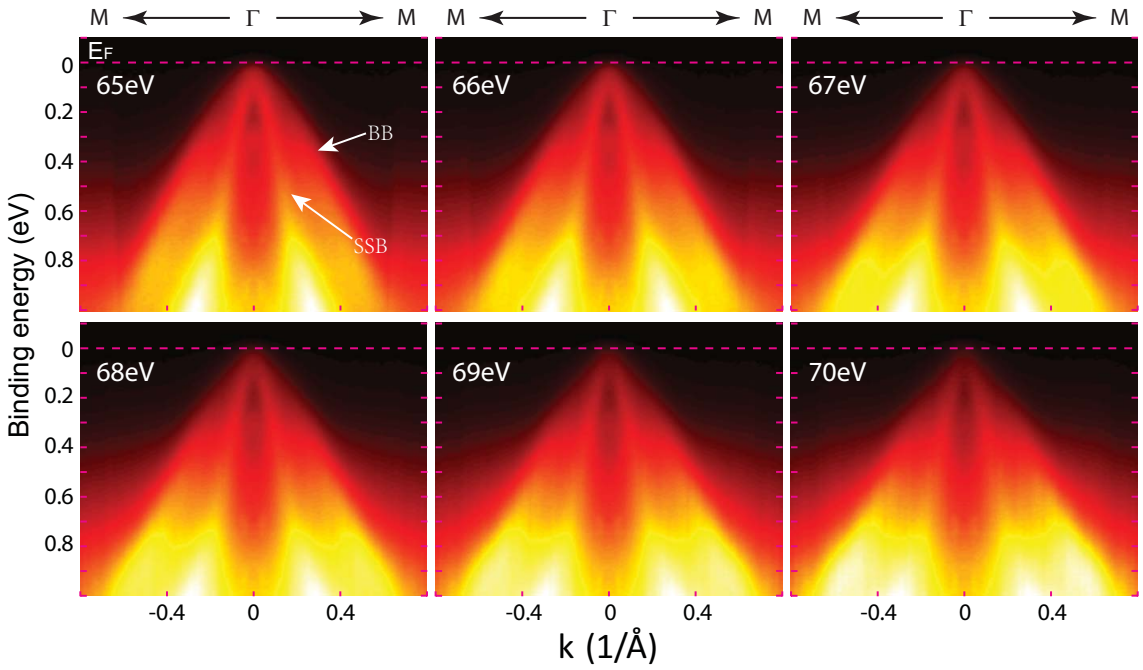

Figure 6.4: Energy dependent band structure along M-Γ-M direction from 65-70eV excitation photons, with the E_F, surface state band (SSB) and the bulk band (BB) marked.

per and lower Dirac cone can be seen, while for the former case, the Dirac point resides close to the Fermi energy and thus only the lower Dirac cone can be seen in the ARPES measurements of Fig. 6.4.

6.5.2 k·p calculation of the band structure of strained HgTe

To understand the transport properties of the 70nm sample, we first calculate the band dispersion of the structure using the $\mathbf{k} \cdot \mathbf{p}$ type approach. HgTe can be well described by the eight-band Kane model, where the electron Γ_6 band and hole Γ_7, Γ_8 bands are taken into account explicitly. The detailed form of the Kane model, as well as the related band parameters, can be found in Ref [39]. As is evident from the reciprocal lattice map of Fig. 6.1, the 70 nm thick HgTe epilayer is fully strained due to the lattice mismatch between CdTe substrate and HgTe. Although this lattice mismatch is small ($\epsilon = (a_{CdTe} - a_{HgTe})/a_{HgTe} \approx 0.003$ with a_{CdTe} and a_{HgTe} lattice constants of CdTe and HgTe, respectively), the resulting strain is sufficient to open a bandgap between the heavy- and light-hole bands. The CdTe substrate is oriented along (001), and for this orientation the strain tensor components are given by $\epsilon_{xx} = \epsilon_{yy} = \epsilon$, $\epsilon_{zz} = -2\epsilon C_{12}/C_{11}$

and $\epsilon_{i\neq j} = 0$ for $i, j = x, y, z$. Here, C_{11} and C_{12} are elastic stiffness constants. Because the off-diagonal components of the strain tensor (the shear components) are zero, there are no internal electric fields generated in the HgTe layer due to piezoelectric effects. The strain tensor components for an arbitrary growth direction can be determined using the model of De Caro *et al* [105]. The effects of the strain tensor can be incorporated in the Kane model through the Bir-Pikus Hamiltonian[106], which can be easily obtained from the Kane Hamiltonian with the substitution $k_i k_j \rightarrow \epsilon_{ij}$. For the present case, one finds that lattice strain shifts the light-hole and heavy-hole band-edges at the Γ-point and leads to the opening of a gap between them which is given by $E_g = -b(\epsilon_{xx} + \epsilon_{yy} - 2\epsilon_{zz})$, where b is the uniaxial deformation potential, which amounts to -1.5 eV for HgTe [103]. For $C_{12}/C_{11} = 0.68$ [107] we obtain $E_g \approx 22$ meV.

Using the above model, we have calculated the band structure of a 0.3 % strained 70nm thick HgTe slab, yielding the dispersion shown in Fig. 6.5. At Γ point, the conduction band edge is around 11meV while the valence band edge around -11meV, and the direct gap at Γ point amounts to 22meV. Within the bulk gap, we find two special states (shown in blue in Fig. 6.5) which touch the valence band states at the Γ point, but merge with the conduction band for large k. In the present system, the Dirac point of the surface state is buried deep within the heavy hole valence band, about 70meV below the valence band edge for the HgTe-CdTe interface and 100meV for the HgTe-Vacuum surface, as shown schematically by the red guiding lines in Fig. 6.5. Therefore, these special states (shown in blue in Fig. 6.5) consist of the surface states originating from the Dirac type dispersion between Γ_6 electron and Γ_8 light-hole bands hybridized with the Γ_8 heavy hole bands[40, 60].

In actual devices, positions of the Dirac points can vary from ones shown here. This is due to band bending from the Hartree potential, which has not been taken into account in the present calculations. Obviously, the existence of the surface states is not sensitive to the Hartree potential due to their topological nature.

6.5.3 Two Dirac cones model

In this section, we will introduce an effective model with two Dirac cones to describe the surface states of a slab of a topological insulator and investigate the Landau level structure evolving from such a system when a perpendicular magnetic field is applied (this defines the z-direction). On the surface of a strong topological insulator, the low-energy physics

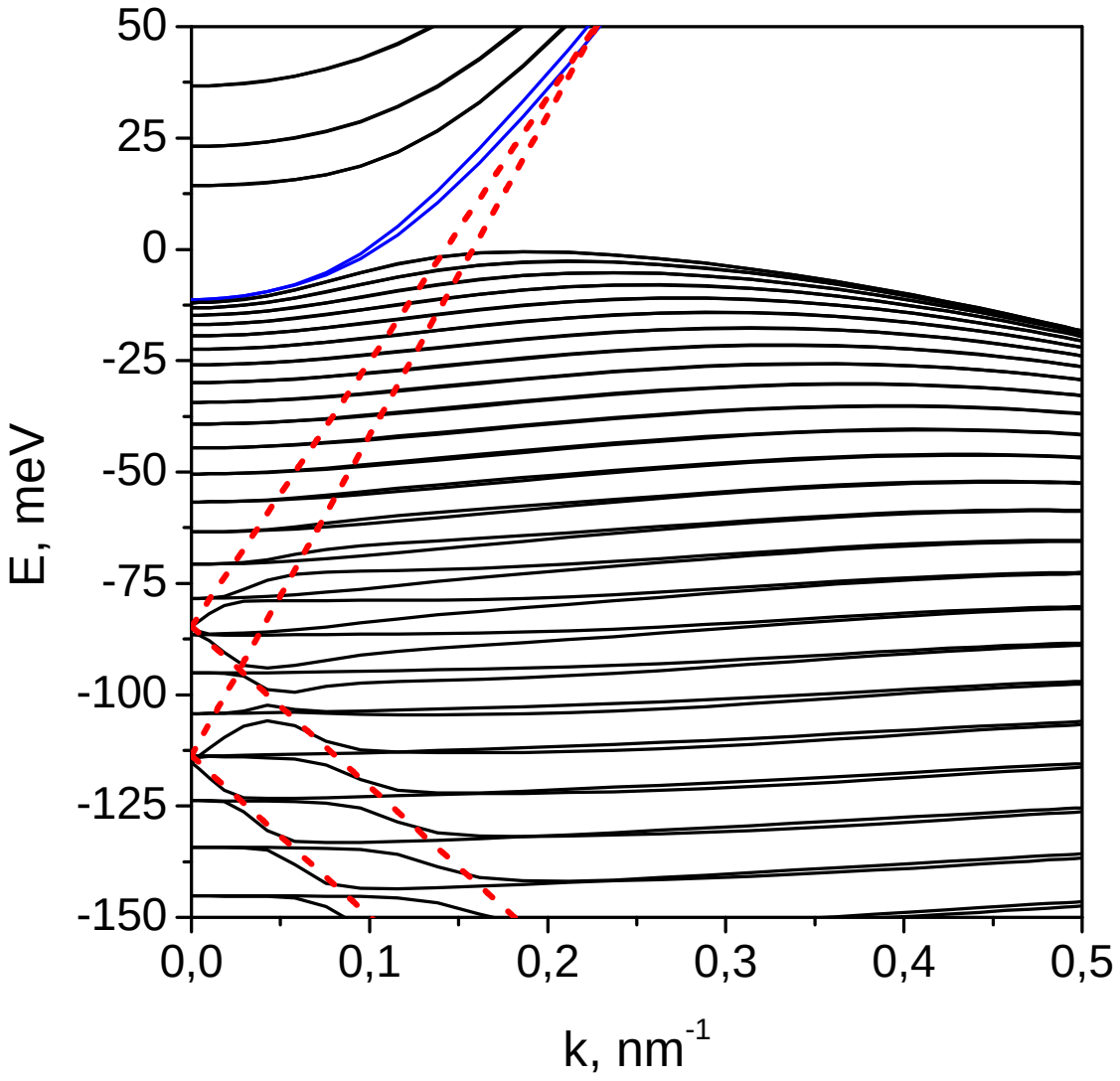

Figure 6.5: Band structure of a 70nm thick 0.3 % strained HgTe slab. The Dirac-like states in the gap are plotted in blue. The dashed red line schematically shows the dispersion of the Dirac surface states at the two opposite surfaces before their hybridization with the Γ_8 heavy hole bands.

of the surface states can be described by the Dirac Hamiltonian, with two components related to each other by time reversal, which we refer to as spin for simplicity. In our slab, we need to take two surfaces, which are perpendicular to the magnetic field and related to each other by inversion, into account, and consequently, there are in total two Dirac cones and the four basis states can be written as $|\alpha, \sigma\rangle$, where $\alpha = \pm$ denotes the upper and lower surface and $\sigma = \uparrow, \downarrow$ denotes spin. Within this four state basis, the effective Hamiltonian is written as

$$\hat{H}_{2D} = \hbar v_f \begin{pmatrix} k_x\sigma_y - k_y\sigma_x & 0 \\ 0 & -(k_x\sigma_y - k_y\sigma_x) \end{pmatrix} = \hbar v_f (k_x\sigma_y - k_y\sigma_x) \otimes \tau_z, \quad (6.1)$$

where the Pauli matrix σ describes spin and τ the opposite surfaces; the Hamiltonian is invariant under the inversion operation $P = \mathbf{1} \otimes \tau_x$ and the time reversal operation $\mathcal{T} = -i\sigma_y \otimes \mathbf{1}K$ where K indicates complex conjugation. We note that for zero gap HgTe/CdTe quantum wells [29], the effective Hamiltonian can also be described by two Dirac cones. However in that case, the two Dirac cones are related to each other by time reversal, while here the two Dirac cones are related by inversion. Besides the effective Hamiltonian $\hat{H}_{2D}$, we also take into account two more terms that may be active in the sample: an inversion breaking term[108]

$$\hat{H}_{ib} = \begin{pmatrix} \Delta_i & 0 \\ 0 & -\Delta_i \end{pmatrix} = \Delta_i \mathbf{1} \otimes \tau_z, \quad (6.2)$$

and a hybridization term between the two surface states, which should become important in very thin slabs:

$$\hat{H}_h = \begin{pmatrix} 0 & \Delta_h \\ \Delta_h & 0 \end{pmatrix} = \Delta_h \mathbf{1} \otimes \tau_x. \quad (6.3)$$

To study the effect of a magnetic field along the z-direction, we first need to make a Peierls substitution, i.e. we replace $\mathbf{k}$ in the Hamiltonian $\hat{H}_{2D}$ with $\pi = \mathbf{k} + \frac{e}{\hbar}\mathbf{A}$, where $\mathbf{A} = (0, B_0 x, 0)$ for a magnetic field $\mathbf{B} = B_0 \hat{z}$. Additionally, we need to consider a Zeeman type term, given by

$$\hat{H}_Z = \begin{pmatrix} g^* \mu_B B_0 \sigma_z & 0 \\ 0 & g^* \mu_B B_0 \sigma_z \end{pmatrix} = g^* \mu_B B_0 \sigma_z \otimes \mathbf{1} \quad (6.4)$$

where g^* is an effective g factor that takes orbital effects of nearby bands into account.

First let us have a look at the Landau levels of the Hamiltonian $\hat{H}_{2D}$, which can be solved as

$$E_{\alpha t}(n) = t\sqrt{2ne\hbar v_f^2 B_0} \qquad n = 1, 2, \cdots \tag{6.5}$$

and $E_\alpha(n = 0) = 0$ for zero modes, where $t = \pm$ denotes the electron and hole levels and $\alpha = \pm$ denotes the upper and lower surfaces. Obviously, each Landau level is doubly degenerate since the the upper and lower surfaces are identical and related by inversion. The zero modes will be half filled at charge neutrality, and, thus due to the double degeneracy, the Hall plateaus should appear only at odd number filling factors $n = 1, 3, 5, \cdots$, which, as described above, is what we observe in low magnetic fields.

In high magnetic fields, Hall plateaus at even number filling factors are also observed, which indicates a splitting of the Landau level degeneracy. In zero gap HgTe/CdTe quantum wells (QWs) case[29], we have found that the even number filling factors observed in that system are caused by Zeeman splitting. It is thus natural to first investigate the same mechanism for the present experiment. This implies solving the Landau level problem for the Hamiltonian $\hat{H}_{2D} + \hat{H}_h + \hat{H}_Z$. One easily finds that in this case the Landau levels are given by

$$E_{\beta t}(n) = t\sqrt{2ne\hbar v_f^2 B_0 + (|\mu_B g^* B_0| + \beta|\Delta_h|)^2} \tag{6.6}$$

for $n = 1, 2, 3, \cdots$ and $E_\beta(0) = -g^*\mu_B B_0 + \beta|\Delta_h|$ for $n = 0$. $\beta = \pm$ From these expressions, we conclude that the double degeneracy remains when only the Zeeman term is important but hybridization between the two surface states is negligible($\Delta_h = 0$). Therefore considerable hybridization between the two surface states (i.e. the slab has to be very thin) is required in order to make this mechanism work. In HgTe, the decay length of the surface states is estimated to be of order $2 \sim 3$nm[60], which is much smaller than the sample thickness of 70 nm. It is thus unlikely that a Zeeman mechanism is responsible for the degeneracy lifting in the present experiment.

The other possible mechanism for Landau level splitting is the breaking of the inversion symmetry - which in practice occurs by the presence of the substrate. To see this, we solve the Landau level problem of the Hamiltonian $\hat{H}_{2D} + \hat{H}_{ib}$ and obtain the eigen-energies as

$$E_{\alpha t} = t\sqrt{2ne\hbar v_f^2 B_0} + \alpha\Delta_i \tag{6.7}$$

for $n = 1, 2, 3, \cdots$ and $E_\alpha(0) = \alpha\Delta_i$ for $n = 0$. From this expression, it is obvious that the degeneracy of the Landau levels is removed for any nonzero Δ_i. This makes inversion-symmetry breaking mechanism the most likely explanation for our observation of even filling factors at high magnetic fields. Since the spacing between the Landau levels increases with magnetic field and one can assume that the disorder broadening of the Landau levels stays constant (as a first approximation), the degeneracy lifting will only be visible in strong magnetic fields.

For a comparison with the experimentally obtained Shubnikov-de Haas oscillations, we calculate the density of states for the energy dispersion (6.7) for two Dirac cones with an inversion-symmetry breaking term. Taking $\hbar v_f = 280meV \cdot nm$ and $\Delta_i = 4.2meV$, we find that the positions of the experimental Shubnikov-de Haas minima can be fitted well with the densities of $n_1 = 3.7 \times 10^{11} cm^{-2}$ and $n_2 = 4.8 \times 10^{11} cm^{-2}$ for the two Dirac cones, which are the traces shown in Fig. 6.3. Further evidence that this is the correct model for our observations comes from the odd filling factor ($\nu = 9, 7, 5$) quantum Hall plateaus we observe at low magnetic fields. A clear discrimination between the Landau level structure of a Dirac system and that of a conventional 2D electron gas can be obtained from plotting of the Landau level index as a function of 1/B[109, 110]. For a Dirac system with multiple Dirac cones, the filling factor is related to the Landau level index N by $\nu = m(N + 1/2)$, where m is the number of the Dirac cones and equals to 2 here. Taking the magnetic field values corresponding to the Hall plateaus $\nu = 9, 7, 5$ from the σ_{xy} curve in Fig. 6.2, and plotting N as a function of 1/B yields Fig. 6.6. The intercept of this plot for infinite magnetic field gives -1/2, which provides additional evidence that the main physics of our system can be well described by the two Dirac cones model.

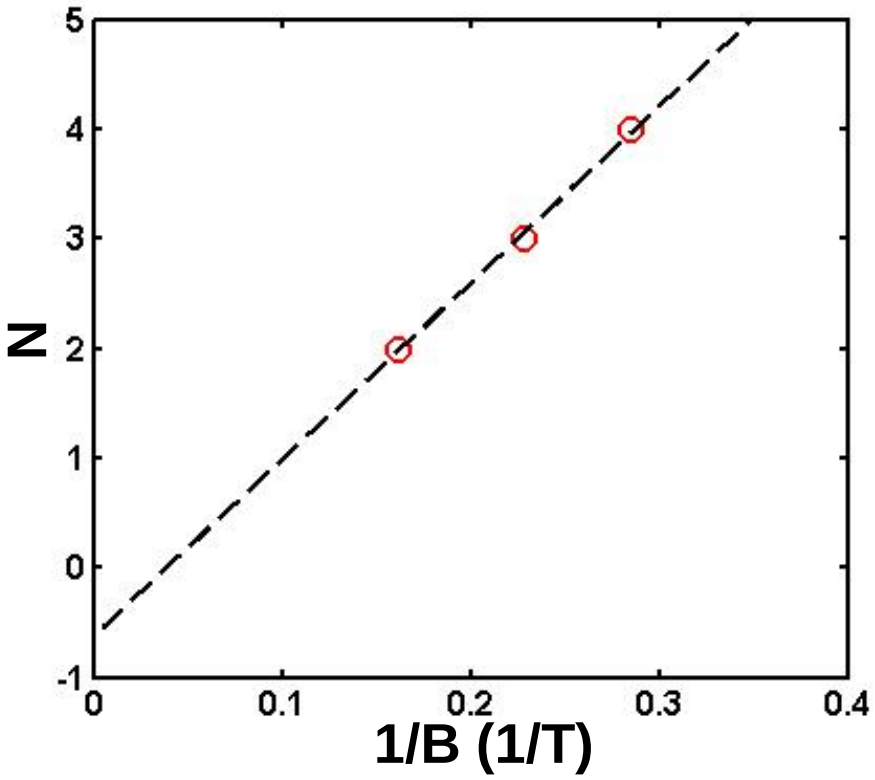

Figure 6.6: Landau level index for the data of Fig. 6.2 plotted as a function of inverse magnetic field.

Bibliography

[1] K. von Klitzing, G. Dorda, and M. Pepper. New Method for High-Accuracy Determination of the Fine-Structure Constant Based on Quantized Hall Resistance. *Phys. Rev. Lett.*, 45:494, 1980.

[2] R. B. Laughlin. Quantized Hall conductivity in two dimensions. *Phys. Rev. B*, 23:5632, 1981.

[3] D. J. Thouless, M. Kohmoto, M. P. Nightingale, and M. den Nijs. Quantized Hall Conductance in a Two-Dimensional Periodic Potential. *Phys. Rev. Lett.*, 49:405, 1982.

[4] D. C. Tsui, H. L. Stormer, and A. C. Gossard. Two-dimensional magnetotransport in the extreme quantum limit. *Phys. Rev. Lett.*, 48:1559, 1982.

[5] R. B. Laughlin. Anomalous Quantum Hall Effect: An Incompressible Quantum Fluid with Fractionally Charged Excitations. *Phys. Rev. Lett.*, 50:1395, 1983.

[6] C. L. Kane and E. J. Mele. Quantum spin Hall effect in graphene. *Phys. Rev. Lett.*, 95:226801, 2005.

[7] B. A. Bernevig, T. L. Hughes, and S. C. Zhang. Quantum spin Hall effect and topological phase transition in HgTe quantum wells. *Science*, 314:1757, 2006.

[8] Markus König and Steffen Wiedmann and Christoph Brüne and Andreas Roth and Hartmut Buhmann and Laurens W. Molenkamp and Xiao-Liang Qi and Shou-Cheng Zhang. Quantum spin Hall insulator state in HgTe quantum wells. *Science*, 318:766, 2007.

[9] L. Fu, C. L. Kane, and E. J. Mele. Topological insulators in three dimensions. *Phys. Rev. Lett.*, 98:106803, 2007.

[10] J. E. Moore and L. Balents. Topological invariants of time-reversal-invariant band structures. *Phys. Rev. B*, 75:121306, 2007.

[11] R. Roy. Topological phases and the quantum spin Hall effect in three dimensions. *Phys. Rev. B*, 79:195322, 2009.

[12] D. Hsieh, D. Qian, L. Wray, Y. Xia, Y. S. Hor, R. J. Cava, and M. Z. Hasan. A topological Dirac insulator in a quantum spin Hall phase. *Nature*, 452:970, 2008.

[13] S. C. Zhang. Topological states of quantum matter. *Physics*, 1:6, 2008.

[14] Y. Xia, L. Wray, D. Qian, D. Hsieh, A. Pal, H. Lin, A. Bansil, D. Grauer, Y.S. Hor, R.J. Cava, and M.Z. Hasan. Observation of a large-gap topological-insulator class with a single Dirac cone on the surface. *Nature Phys.*, 5:398, 2009.

[15] Y. L. Chen, J. G. Analytis, J. H. Chu, Z. K. Liu, S.-K. Mo, X. L. Qi, H. J. Zhang, D. H. Lu, X. Dai, Z. Fang, S. C. Zhang, I. R. Fisher, Z. Hussain, and Z.-X. Shen. Large Gap Topological Insulator Bi_2Te_3 with a Single Dirac Cone on the Surface. *Science*, 325:178, 2009.

[16] A. K. Geim and K. S. Novoselov. The rise of graphene. *Nat. Mat.*, 6:183–191, 2007.

[17] A. H. Castro Neto, F. Guinea, N. M. R. Peres, K. S. Novoselov, and A. K. Geim. The electronic properties of graphene. *Rev. Mod. Phys.*, 81:109, 2009.

[18] M. Z. Hasan and C. L. Kane. Colloquium: Topological insulators. *Rev. Mod. Phys.*, 82:3045–3067, 2010.

[19] C. L. Kane and E. J. Mele. Z_2 topological order and the quantum spin Hall effect. *Phys. Rev. Lett.*, 95:146802, 2005.

[20] H. Min, J. Hill, N. Sinitsyn, B. Sahu, L. Kleinman, and A. MacDonald. Intrinsic and Rashba spin-orbit interactions in graphene sheets. *Phys. Rev. B*, 74:165310, 2006.

[21] Yugui Yao, Fei Ye, Xiao-Liang Qi, Shou-Cheng Zhang, and Zhong Fang. Spin-orbit gap of graphene: First-principles calculations. *Phys. Rev. B*, 75:041401, 2007.

[22] B. A. Bernevig and S. C. Zhang. Quantum spin Hall effect. *Phys. Rev. Lett.*, 96:106802, 2006.

[23] X. L. Qi, Y. S. Wu, and S. C. Zhang. A general theorem relating the bulk topological number to edge states in two-dimensional insulators. *Phys. Rev. B*, 74:045125, 2006.

[24] A. Pfeuffer-Jeschke. *Bandstruktur und Landau-Niveaus quecksilberhaltiger II-VI-Heterostrukturen*. PhD thesis, Universität Würzburg, 2000.

[25] Andreas Roth, Christoph Brüne, Hartmut Buhmann, Laurens W. Molenkamp, Joseph Maciejko, Xiao-Liang Qi, and Shou-Cheng Zhang. Nonlocal transport in the quantum spin Hall state. *Science*, 325:294, 2009.

[26] C. Brüne, A. Roth, E. G. Novik, M. König, H. Buhmann, E. M. Hankiewicz, W. Hanke, J. Sinova, and L. W. Molenkamp. Spin polarization of the quantum spin Hall edge states. *Nature Phys.*, 8:485–490, 2012.

[27] G. W. Semenoff. Condensed-Matter Simulation of a Three-Dimensional Anomaly. *Phys. Rev. Lett.*, 53:2449, 1984.

[28] D. P. DiVincenzo and E. J. Mele. Self-consistent effective-mass theory for intralayer screening in graphite intercalation compounds. *Phys. Rev. B*, 29:1685–1694, 1984.

[29] B. Büttner, C. X. Liu, G. Tkachov, E. G. Novik, C. Brüne, H. Buhmann, E. M. Hankiewicz, P. Recher, B. Trauzettel, S. C. Zhang, and L. W. Molenkamp. Single valley Dirac fermions in zero-gap HgTe quantum wells. *Nature Phys.*, 7:418–422, 2011.

[30] M. Franz. `http://www.physics.ubc.ca/~franz/pub1.html`, 09.02.2012.

[31] K. Nomura, M. Koshino, and S. Ryu. Topological delocalization of two-dimensional massless Dirac fermions. *Phys. Rev. Lett.*, 99:146806, 2007.

[32] L. Fu and C. L. Kane. Topological insulators with inversion symmetry. *Phys. Rev. B*, 76:045302, 2007.

[33] D. Hsieh, Y. Xia, D. Qian, L. Wray, J. H. Dil, F. Meier, J. Osterwalder, L. Patthey, J. G. Checkelsky, N. P. Ong, A. V. Fedorov, H. Lin, A. Bansil, D. Grauer, Y. S. Hor, R. J. Cava, and M. Z. Hasan. A tunable topological insulator in the spin helical dirac transport regime. *Nature*, 460:1101, 2009.

[34] P. D. C. King, R. C. Hatch, M. Bianchi, R. Ovsyannikov, C. Lupulescu, G. Landolt, B. Slomski, J. H. Dil, D. Guan, J. L. Mi, E. D. L. Rienks, J. Fink, A. Lindblad, S. Svensson, S. Bao, G. Balakrishnan, B. B. Iversen, J. Osterwalder, W. Eberhardt, F. Baumberger, and Ph. Hofmann. Large Tunable Rashba Spin Splitting of a Two-Dimensional Electron Gas in Bi_2Se_3. *Phys. Rev. Lett.*, 107:096802, Aug 2011.

[35] C. Brüne, C. X. Liu, E. G. Novik, E. M. Hankiewicz, H. Buhmann, Y. L. Chen, X. L. Qi, Z. X. Shen, S. C. Zhang, and L. W. Molenkamp. Quantum Hall Effect from the Topological Surface States of Strained Bulk HgTe. *Phys. Rev. Lett.*, 106:126803, 2011.

[36] C. Brüne, H. Buhmann, and L.W. Molenkamp. *Topological Insulators*, chapter 5, pages 125–143. Contemporary Concepts Of Condensed Matter Science. Elsevier, Amsterdam, 2013.

[37] J Chu and A Sher. *Physics and Properties of Narrow Gap Semiconductors*. Springer, New York, 2008.

[38] D.J. Chadi, John P. Walter, and Marvin L. Cohen. Reflectivities and Electronic Band Structures of CdTe and HgTe. *PRB*, 5:3058–3064, 1972.

[39] E. G. Novik, A. Pfeuffer-Jeschke, T. Jungwirth, V. Latussek, C. R. Becker, G. Landwehr, H. Buhmann, and L. W. Molenkamp. Band structure of semimagnetic $\mathrm{Hg_{1-y}Mn_yTe}$ quantum wells. *Phys. Rev. B*, 72:035321, 2005.

[40] Xi Dai, Taylor L. Hughes, Xiao-Liang Qi, Zhong Fang, and Shou-Cheng Zhang. Helical edge and surface states in HgTe quantum wells and bulk insulators. *Phys. Rev. B*, 77:125319, 2008.

[41] C.R. Becker, C. Brüne, M. Schäfer, A. Roth, H. Buhmann, and L. W. Molenkamp. The influence of interfaces and the modulation doping technique on the magneto-transport properties of HgTe based quantum wells. *Phys. Stat. Sol. c)*, 4:3382Ű3389, 2007.

[42] M. König, H. Buhmann, L. W. Molenkamp, T. L. Hughes, C. X. Liu, X. L. Qi, and S. C. Zhang. The quantum spin Hall effect: theory and experiment. *J. Phys. Soc. Jpn*, 77:031007, 2008.

[43] M. Büttiker. Four-terminal phase-coherent conductance. *Phys. Rev. Lett.*, 57:1761, 1986.

[44] M. Büttiker. Absence of backscattering in the quantum Hall effect in multiprobe conductors. *Phys. Rev. B*, 38:9375, 1988.

[45] Katja C. Nowack, Eric M. Spanton, Matthias Baenninger, Markus König, John R. Kirtley, Beena Kalisky, Christopher Ames, Philipp Leubner, Christoph Brüne, Hartmut Buhmann, Laurens W. Molenkamp, David Goldhaber-Gordon, and Kathryn A. Moler. Imaging currents in HgTe quantum wells in the quantum spin Hall regime. *Nature Mater.*, 12:787–791, 2013.

[46] M. I. Dyakonov and V. I. Perel. Current-induced spin orientation of electrons in semiconductors. *Phys. Lett. A*, 35:459–460, 1971.

[47] J. E. Hirsch. Spin Hall effect. *PRL*, 83:1834–1837, 1999.

[48] Y. S. Gui, C. R. Becker, N. Dai, J. Liu, Z. J. Qiu, E. G. Novik, M. Schäfer, X. Z. Shu, J. H. Chu, H. Buhmann, and L. W. Molenkamp. Giant spin-orbit splitting in a HgTe quantum well. *Phys. Rev. B*, 70:115328, 2004.

[49] J. Sinova, D. Culcer, Q. Niu, N. A. Sinitsyn, T. Jungwirth, and A. H. MacDonald. Universal intrinsic spin Hall effect. *Phys. Rev. Lett.*, 92:126603, 2004.

[50] E. M. Hankiewicz, L. W. Molenkamp, T. Jungwirth, and Jairo Sinova. Manifestation of the spin hall effect through charge-transport in the mesoscopic regime. *Phys. Rev. B*, 70:241301, Dec 2004.

[51] B. K. Nikolić, S. Sourma, L. Zârbo, and J. Sinova. Nonequilibrium spin Hall accumulation in ballistic semiconductor nanostructures. *Phys. Rev. Lett.*, 95:046601, 2005.

[52] C. Brüne, A. Roth, E. G. Novik, M. König, H. Buhmann, E. M. Hankiewicz, W. Hanke, J. Sinova, and L.W. Molenkamp. Evidence for the ballistic intrinsic spin Hall effect in HgTe quantum wells. *Nature Phys.*, 6:448–454, 2010.

[53] B. Zhou, H.-Z. Lu, R.-L. Chu, S.-Q. Shen, and Q. Niu. Finite size effects on helical edge states in a quantum spin Hall system. *Phys. Rev. Lett.*, 101:246807, 2008.

[54] Andrew M. Essin, Joel E. Moore, and David Vanderbilt. Magnetoelectric polarizability and axion electrodynamics in crystalline insulators. *Phys. Rev. Lett.*, 102:146805, 2009.

[55] M. Büttiker. Symmetry of electrical conduction. *IBM J. Res. Dev.*, 32:317–334, 1988.

[56] T. Skauli and T. Colin. Accurate determination of the lattice constant of molecular beam epitaxial CdHgTe. *Journal of Crystal Growth*, 222(4):719 – 725, 2001.

[57] James G. Analytis, Ross D. McDonald, Scott C. Riggs, Jiun-Haw Chu, G. S. Boebinger, and Ian R. Fisher. Two-dimensional surface state in the quantum limit of a topological insulator. *Nat Phys*, 6:960–964, 2010.

[58] Dong-Xia Qu, Y. S. Hor, Jun Xiong, R. J. Cava, and N. P. Ong. Quantum oscillations and Hall anomaly of surface states in the topological Insulator $\mathrm{Bi_2Te_3}$. *Science*, 329:821–824, 2010.

[59] Xiao-Liang Qi, Taylor L. Hughes, and Shou-Cheng Zhang. Topological field theory of time-reversal invariant insulators. *Phys. Rev. B*, 78:195424, 2008.

[60] Rui-Lin Chu, Junren Shi, and Shun-Qing Shen. Surface-edge state and half quantized Hall conductance in topological insulators. *Phys. Rev. B*, 84:085312, 2011.

[61] Christoph Brüne, Cornelius Thienel, Michael Stuiber, Hartmut Buhmann, Elena G. Novik, Chao-Xing Liu, Ewelina M. Hankiewicz, and Laurens W. Molenkamp. Unperturbed Dirac spectrum from the surface states of gated strained bulk HgTe. In preparation for publication, 2014.

[62] David D. Awschalom and Michael E. Flatté. Challenges for semiconductor spintronics. *Nat. Phys.*, 3:153–159, 2007.

[63] E. M. Hankiewicz and G. Vignale. Coulomb corrections to the extrinsic spin-hall effect of a two-dimensional electron gas. *Phys. Rev. B*, 73:115339, Mar 2006.

[64] H.-A. Engel, E. I. Rashba, and B. I. Halperin. *Handbook of Magnetism and Advanced Magnetic Materials*. Contemporary Concepts Of Condensed Matter Science. John Wiley & Sons Ltd, Chichester, 2007.

[65] S. Murakami, N. Nagaosa, and S. C. Zhang. Dissipationless quantum spin current at room temperature. *Science*, 301:1348, 2003.

[66] Y. K. Kato *et al. Science*, 306:1910, 2004.

[67] J. Wunderlich *et al. Phys. Rev. Lett.*, 94:047204, 2005.

[68] Sih, V. and Myers, R. C. and Kato, Y. K. and Lau, W. H. and Gossard, A. C. and Awschalom, D. D. Spatial imaging of the spin Hall effect and current-induced polarization in two-dimensional electron gases. *Nat. Phys.*, 1:31 – 35, 2005.

[69] Valenzuela, S. O. and Tinkham, M. Direct electronic measurement of the spin Hall effect. *Nature*, 442:176–179, 2006.

[70] E. Saitoh, M. Ueda, H. Miyajima, and G. Tatara. Conversion of spin current into charge current at room temperature: Inverse spin-hall effect. *Applied Physics Letters*, 88(18):182509, 2006.

[71] T. Kimura, Y. Otani, T. Sato, S. Takahashi, and S. Maekawa. Room-temperature reversible spin hall effect. *Phys. Rev. Lett.*, 98:156601, Apr 2007.

[72] Seki, Takeshi and Hasegawa, Yu and Mitani, Seiji and Takahashi, Saburo and Imamura, Hiroshi and Maekawa, Sadamichi and Nitta, Junsaku and Takanashi, Koki. Giant spin Hall effect in perpendicularly spin-polarized FePt/Au devices. *Nat. Mat.*, 7:125–129, 2008.

[73] KoongChee Weng, N. Chandrasekhar, C. Miniatura, and Berthold-Georg Englert. Spin orbit interaction induced spin-separation in platinum nanostructure. In Janez Bona and Sergei Kruchinin, editors, *Electron Transport in Nanosystems*, NATO Science for Peace and Security Series B: Physics and Biophysics, pages 49–58. Springer Netherlands, 2008.

[74] J. Hinz, H. Buhmann, M. Schäfer, V. Hock, C R. Becker, and L. W. Molenkamp. Quantum transport in semiconductor nanostructures. *Semicond. Sci. Technol.*, (21):501, 2006.

[75] E. M. Hankiewicz, Jian Li, Tomas Jungwirth, Qian Niu, Shun-Qing Shen, and Jairo Sinova. Charge hall effect driven by spin-dependent chemical potential gradients and onsager relations in mesoscopic systems. *Phys. Rev. B*, 72:155305, Oct 2005.

[76] Wen Yang, Kai Chang, and Shou-Cheng Zhang. Intrinsic spin hall effect induced by quantum phase transition in hgcdte quantum wells. *Phys. Rev. Lett.*, 100:056602, Feb 2008.

[77] S. Datta. *Electronic Transport in Mesoscopic Systems*. Cambridge University Press, Cambridge, 2007.

[78] E. M. Hankiewicz and G. Vignale. Phase diagram of the spin hall effect. *Phys. Rev. Lett.*, 100:026602, Jan 2008.

[79] C. Wu, B. A. Bernevig, and S. C. Zhang. Helical liquid and the edge of quantum spin Hall systems. *Phys. Rev. Lett.*, 96:106401, 2006.

[80] C. Xu and J. Moore. Stability of the quantum spin Hall effect: Effects of interactions, disorder, and Z_2 topology. *Phys. Rev. B*, 73:045322, 2006.

[81] J. Maciejko, C. X. Liu, Y. Oreg, X. L. Qi, C. Wu, and S. C. Zhang. Kondo effect in the helical edge liquid of the quantum spin hall state. *Phys. Rev. Lett.*, 102:256803, 2009.

[82] M. Büttiker. Edge-state physics without magnetic fields. *Science*, 325:278, 2009.

[83] D. G. Rothe, R. W. Reinthaler, C. X. Liu, L. W. Molenkamp, S. C. Zhang, and E. M. Hankiewicz. *New J. Phys.*, 12:065012, 2010.

[84] C. W. J. Beenakker and H. van Houten. Billiard model of a ballistic multiprobe conductor. *Phys. Rev. Lett.*, 63:1857–1860, Oct 1989.

[85] Ganesh Sundaram and Qian Niu. Wave-packet dynamics in slowly perturbed crystals: Gradient corrections and berry-phase effects. *Phys. Rev. B*, 59:14915–14925, Jun 1999.

[86] C. W. J. Beenakker and H. van Houten. Quantum transport in semiconductor nanostructures. *Solid State Phys.*, 44:1, 1991.

[87] C. Jacoboni and P. Lugli. *The Monte Carlo Method for Semiconductor Device Simulation*. Springer Verlag, New York, 1989.

[88] C. W. J. Beenakker and H. van Houten. Magnetotransport and nonadditivity of point-contact resistances in series. *Phys. Rev. B*, 39:10445–10448, May 1989.

[89] L. W. Molenkamp, A. A. M. Staring, C. W. J. Beenakker, R. Eppenga, C. E. Timmering, J. G. Williamson, C. J. P. M. Harmans, and C. T. Foxon. Electron-beam collimation with a quantum point contact. *Phys. Rev. B*, 41:1274–1277, Jan 1990.

[90] A. S. D. Heindrichs, H. Buhmann, S. F. Godijn, and L. W. Molenkamp. Classical rebound trajectories in nonlocal ballistic electron transport. *Phys. Rev. B*, 57:3961–3965, Feb 1998.

[91] V. Daumer, I. Golombek, M. Gbordzoe, E. G. Novik, V. Hock, C.R. Becker, H. Buhmann, and L.W. Molenkamp. Quasiballistic transport in hgte quantum-well nanostructures. *Applied Physics Letters*, 83(7):1376–1378, Aug 2003.

[92] S. Murakami, N. Nagaosa, and S. C. Zhang. SU(2) non-Abelian holonomy and dissipationless spin current in semiconductors. *Phys. Rev. B*, 69:235206, 2004.

[93] Takehito Yokoyama, Yukio Tanaka, and Naoto Nagaosa. Giant spin rotation in the junction between a normal metal and a quantum spin hall system. *Phys. Rev. Lett.*, 102:166801, Apr 2009.

[94] N A Sinitsyn. Semiclassical theories of the anomalous hall effect. *Journal of Physics: Condensed Matter*, 20(2):023201, 2008.

[95] G. Tkachov and E. M. Hankiewicz. Ballistic quantum spin hall state and enhanced edge backscattering in strong magnetic fields. *Phys. Rev. Lett.*, 104:166803, 2010.

[96] Joseph Maciejko, Xiao-Liang Qi, H. Dennis Drew, and Shou-Cheng Zhang. e-print arXiv:1004.2514, 2010.

[97] Haijun Zhang, Chao-Xing Liu, Xiao-Liang Qi, Xi Dai, Zhong Fang, and Shou-Cheng Zhang. Topological insulators in Bi_2Se_3, Bi_2Te_3 and Sb_2Te_3 with a single Dirac cone on the surface. *Nature Phys.*, 5:438–442, 2009.

[98] Joel E. Moore. The birth of topological insulators. *Nature*, 464:194–198, 2010.

[99] L. Fu and C. L. Kane. Superconducting proximity effect and majorana fermions at the surface of a topological insulator. *Phys. Rev. Lett.*, 100:096407, 2008.

[100] Y. C. Chang, J. N. Schuman, G. Bastard, Y. Guldner, and M. Voos. Effects of quasi-interface states in HgTe-CdTe superlattices. *Phys. Rev. B*, 31:2557, 1985.

[101] O. A. Pankratov. Electronic properties of band-inverted heterojunctions: supersymmetry in narrow-gap semiconductors. *Semicond. Sci. Technol.*, 5:S204, 1990.

[102] G. Bauer and W. Richter. *Optical Characterization of Epitaxial Semiconductor Layers*, chapter 6, pages 287–391. Springer, Berlin Heidelberg, 1996.

[103] S. Adachi. *Properties of Semiconductor Alloys: Group-IV, III-V and II-VI Semiconductors*. John Wiley & Sons, 2009.

[104] Y. L. Chen, J.-H. Chu, J. G. Analytis, Z. K. Liu, K. Igarashi, H.-H. Kuo, X. L.

Qi, S. K. Mo, R. G. Moore, D. H. Lu, M. Hashimoto, T. Sasagawa, S. C. Zhang, I. R. Fisher, Z. Hussain, and Z. X. Shen. Massive dirac fermion on the surface of a magnetically doped topological insulator. *Science*, 329:659–662, 2010.

[105] Liberato De Caro and Leander Tapfer. Strain and piezoelectric fields in arbitrarily oriented semiconductor heterostructures. i. multiple quantum wells. *Phys. Rev. B*, 51:4374–4380, 1995.

[106] G.L. Bir and G.E. Pikus. *Symmetry and Strain-induced Effects in Semiconductors*. John Wiley & Sons, Chichester, 1974.

[107] R.I. Barabash, J.S. Chung, and M.F. Thorpe. Lattice and continuum theories of huang scattering. *J. Phys.: Condens. Matter*, 11:3075, 1999.

[108] Wen-Yu Shan, Hai-Zhou Lu, and Shun-Qing Shen. Effective continuous model for surface states and thin films of three-dimensional topological insulators. *New Journal of Physics*, 12:043048, 2010.

[109] K. S. Novoselov, A. K. Geim, S. V. Morozov, D. Jiang, M. I. Katsnelson, I. V. Grigorieva, S. V. Dubonos, and A. A. Firsov. Two-dimensional gas of massless Dirac fermions in graphene. *Nature*, 438:197–200, 2005.

[110] Y. Zhang, Y. W. Tan, H. L. Stormer, and P. Kim. Experimental observation of the quantum Hall effect and Berry's phase in graphene. *Nature*, 438:201–204, 2005.

Liste der eigenen Veröffentlichungen

[1] C.R. Becker, C. Brüne, M. Schäfer, A. Roth, H. Buhmann, and L. W. Molenkamp. The influence of interfaces and the modulation doping technique on the magneto-transport properties of HgTe based quantum wells. *Phys. Stat. Sol. c)*, 4:3382–3389, 2007. URL: http://dx.doi.org/10.1002/pssc.200775402, doi:10.1002/pssc.200775402.

[2] Markus König, Steffen Wiedmann, Christoph Brüne, Andreas Roth, Hartmut Buhmann, Laurens W. Molenkamp, Xiao-Liang Qi, and Shou-Cheng Zhang. Quantum spin Hall insulator state in HgTe quantum wells. *Science*, 318:766, 2007. URL: http://www.sciencemag.org/content/318/5851/766.abstract, doi:10.1126/science.1148047.

[3] Andreas Roth, Christoph Brüne, Hartmut Buhmann, Laurens W. Molenkamp, Joseph Maciejko, Xiao-Liang Qi, and Shou-Cheng Zhang. Nonlocal transport in the quantum spin Hall state. *Science*, 325:294, 2009. URL: http://www.sciencemag.org/content/325/5938/294.abstract, doi:10.1126/science.1174736.

[4] H. Diehl, V. A. Shalygin, L. E. Golub, S. A. Tarasenko, S. N. Danilov, V. V. Bel'kov, E. G. Novik, H. Buhmann, C. Brüne, L. W. Molenkamp, E. L. Ivchenko, and S. D. Ganichev. Nonlinear magnetogyrotropic photogalvanic effect. *Phys. Rev. B*, 80:075311, Aug 2009. URL: http://link.aps.org/doi/10.1103/PhysRevB.80.075311, doi:10.1103/PhysRevB.80.075311.

[5] F Gouider, M Bugár, J Könemann, Yu B Vasilyev, C Brüne, H Buhmann, and G Nachtwei. THz Photoresponse and Magnetotransport of detectors made of HgCdTe/HgTe quantum well structures. *Journal of Physics: Conference Series*, 193(1):012066, 2009. URL: http://stacks.iop.org/1742-6596/193/i=1/a=012066.

[6] F. Gouider, Y.B. Vasilyev, M. Bugár, J. Könemann, C. Brüne, H. Buhmann, and G. Nachtwei. Magnetotransport and THz-Optical Investigations at Devices with HgTe Quantum Wells. *Journal of Low Temperature Physics*, 159(1-2):184–188, 2010. URL: http://dx.doi.org/10.1007/s10909-009-0115-5, doi:10.1007/s10909-009-0115-5.

[7] C. Brüne, A. Roth, E. G. Novik, M. König, H. Buhmann, E. M. Hankiewicz, W. Hanke, J. Sinova, and L.W. Molenkamp. Evidence for the ballistic intrinsic spin Hall effect in HgTe quantum wells. *Nature Phys.*, 6:448–454. URL: http://dx.doi.org/10.1038/nphys1655.

[8] Yu. B. Vasilyev, F. Gouider, M. Bugár, G. Nachtwei, J. Könemann, C. Brüne, and H. Buhmann. Terahertz photoconductivity of a two-dimensional electron gas in HgCdTe/HgTe quantum wells. *physica status solidi (b)*, 247(6):1495–1497, 2010. URL: http://dx.doi.org/10.1002/pssb.200983180, doi:10.1002/pssb.200983180.

[9] Gouider, F. and Hein, G. and Brüne, C. and Buhmann, H. and Vasilyev, Yu. B. and Nachtwei, G. THz photoresponse of quantum Hall devices based on HgTe-Quantum wells. *AIP Conference Proceedings*, 1199(1):237–238, 2010. URL: http://scitation.aip.org/content/aip/proceeding/aipcp/10.1063/1.3295386, doi:http://dx.doi.org/10.1063/1.3295386.

[10] B Wittmann, S N Danilov, V V Bel'kov, S A Tarasenko, E G Novik, H Buhmann, C Brüne, L W Molenkamp, Z D Kvon, N N Mikhailov, S A Dvoretsky, N Q Vinh, A F G van der Meer, B Murdin, and S D Ganichev. Circular photogalvanic effect in HgTe/CdHgTe quantum well structures. *Semiconductor Science and Technology*, 25(9):095005, 2010. URL: http://stacks.iop.org/0268-1242/25/i=9/a=095005.

[11] Gouider, F. and Nachtwei, G. and Brüne, C. and Buhmann, H. and Vasilyev, Yu. B. and Salman, M. and Könemann, J. and Buckle, P. D. The detection of terahertz waves by semimetallic and by semiconducting materials. *Journal of Applied Physics*, 109(1):013106, 2011. URL: http://scitation.aip.org/content/aip/journal/jap/109/1/10.1063/1.3530727, doi:{http://dx.doi.org/10.1063/1.3530727}.

[12] G. Tkachov, C. Thienel, V. Pinneker, B. Büttner, C. Brüne, H. Buhmann,

L. W. Molenkamp, and E. M. Hankiewicz. Backscattering of Dirac Fermions in HgTe Quantum Wells with a Finite Gap. *Phys. Rev. Lett.*, 106:076802, Feb 2011. URL: http://link.aps.org/doi/10.1103/PhysRevLett.106.076802, doi:10.1103/PhysRevLett.106.076802.

[13] Orlita, M. and Masztalerz, K. and Faugeras, C. and Potemski, M. and Novik, E. G. and Brüne, C. and Buhmann, H. and Molenkamp, L. W. Fine structure of zero-mode Landau levels in HgTe/Hg_xCd_{1-x}Te quantum wells. *Phys. Rev. B*, 83:115307, Mar 2011. URL: http://link.aps.org/doi/10.1103/PhysRevB.83.115307, doi:10.1103/PhysRevB.83.115307.

[14] Shuvaev, A. M. and Astakhov, G. V. and Pimenov, A. and Brüne, C. and Buhmann, H. and Molenkamp, L. W. Giant Magneto-Optical Faraday Effect in HgTe Thin Films in the Terahertz Spectral Range. *Phys. Rev. Lett.*, 106:107404, Mar 2011. URL: http://link.aps.org/doi/10.1103/PhysRevLett.106.107404, doi:10.1103/PhysRevLett.106.107404.

[15] C. Brüne, C. X. Liu, E. G. Novik, E. M. Hankiewicz, H. Buhmann, Y. L. Chen, X. L. Qi, Z. X. Shen, S. C. Zhang, and L. W. Molenkamp. Quantum Hall Effect from the Topological Surface States of Strained Bulk HgTe. *Phys. Rev. Lett.*, 106:126803. URL: http://link.aps.org/doi/10.1103/PhysRevLett.106.126803, doi:10.1103/PhysRevLett.106.126803.

[16] B. Büttner, C. X. Liu, G. Tkachov, E. G. Novik, C. Brüne, H. Buhmann, E. M. Hankiewicz, P. Recher, B. Trauzettel, S. C. Zhang, and L. W. Molenkamp. Single valley Dirac fermions in zero-gap HgTe quantum wells. *Nature Phys.*, 7:418–422. URL: http://dx.doi.org/10.1038/nphys1914.

[17] Jason N. Hancock, J. L. M. van Mechelen, Alexey B. Kuzmenko, Dirk van der Marel, Christoph Brüne, Elena G. Novik, Georgy V. Astakhov, Hartmut Buhmann, and Laurens W. Molenkamp. Surface state charge dynamics of a high-mobility three-dimensional topological insulator. *Phys. Rev. Lett.*, 107:136803, Sep 2011. URL: http://link.aps.org/doi/10.1103/PhysRevLett.107.136803, doi:10.1103/PhysRevLett.107.136803.

[18] Gouider, F. and Vasilyev, Yu. B. and Könemann, J. and Buckle, P. D. and Brüne, C. and Buhmann, H. and Nachtwei, G. Detection of THz radiation with de-

vices made from wafers with HgTe and InSb quantum wells. *AIP Conference Proceedings*, 1399(1):1019–1020, 2011. URL: http://scitation.aip.org/content/aip/proceeding/aipcp/10.1063/1.3666725, doi:http://dx.doi.org/10.1063/1.3666725.

[19] C. Brüne, A. Roth, E. G. Novik, M. König, H. Buhmann, E. M. Hankiewicz, W. Hanke, J. Sinova, and L. W. Molenkamp. Spin polarization of the quantum spin Hall edge states. *Nature Phys.*, 8:485–490. URL: http://dx.doi.org/10.1038/nphys2322.

[20] Luis Maier, Jeroen B. Oostinga, Daniel Knott, Christoph Brüne, Pauli Virtanen, Grigory Tkachov, Ewelina M. Hankiewicz, Charles Gould, Hartmut Buhmann, and Laurens W. Molenkamp. Induced Superconductivity in the Three-Dimensional Topological Insulator HgTe. *Phys. Rev. Lett.*, 109:186806, Nov 2012. URL: http://link.aps.org/doi/10.1103/PhysRevLett.109.186806, doi:10.1103/PhysRevLett.109.186806.

[21] Baenninger, M. and König, M. and Garcia, A. G. F. and Mühlbauer, M. and Ames, C. and Leubner, P. and Brüne, C. and Buhmann, H. and Molenkamp, L. W. and Goldhaber-Gordon, D. Fabrication of samples for scanning probe experiments on quantum spin Hall effect in HgTe quantum wells. *Journal of Applied Physics*, 112(10):103713, 2012. URL: http://scitation.aip.org/content/aip/journal/jap/112/10/10.1063/1.4767362, doi:http://dx.doi.org/10.1063/1.4767362.

[22] A M Shuvaev and G V Astakhov and C Brüne and H Buhmann and L W Molenkamp and A Pimenov. Terahertz magneto-optical spectroscopy in HgTe thin films. *Semiconductor Science and Technology*, 27(12):124004, 2012. URL: http://stacks.iop.org/0268-1242/27/i=12/a=124004.

[23] Schreyeck, S. and Tarakina, N. V. and Karczewski, G. and Schumacher, C. and Borzenko, T. and Brüne, C. and Buhmann, H. and Gould, C. and Brunner, K. and Molenkamp, L. W. Molecular beam epitaxy of high structural quality Bi2Se3 on lattice matched InP(111) substrates. *Applied Physics Letters*, 102(4):041914, 2013. URL: http://scitation.aip.org/content/aip/journal/apl/102/4/10.1063/1.4789775, doi:{http://dx.doi.org/10.1063/1.4789775}.

[24] Yao, S. H. and Zhou, B. and Lu, M. H. and Liu, Z. K. and Chen, Y. B. and Analytis, J. G. and Brüne, C. and Dang, W. H. and Mo, S.-K. and Shen, Z.-X. and Fisher, I. R. and Molenkamp, L. W. and Peng, H. L. and Hussain, Z. and Chen, Y. L. Observing electronic structures on ex-situ grown topological insulator thin films. *physica status solidi (RRL) - Rapid Research Letters*, 7(1-2):130–132, 2013. URL: http://dx.doi.org/10.1002/pssr.201206400, doi:10.1002/pssr.201206400.

[25] Shuvaev, A. M. and Astakhov, G. V. and Tkachov, G. and Brüne, C. and Buhmann, H. and Molenkamp, L. W. and Pimenov, A. Terahertz quantum Hall effect of Dirac fermions in a topological insulator. *Phys. Rev. B*, 87:121104, Mar 2013. URL: http://link.aps.org/doi/10.1103/PhysRevB.87.121104, doi:10.1103/PhysRevB.87.121104.

[26] König, Markus and Baenninger, Matthias and Garcia, Andrei G. F. and Harjee, Nahid and Pruitt, Beth L. and Ames, C. and Leubner, Philipp and Brüne, Christoph and Buhmann, Hartmut and Molenkamp, Laurens W. and Goldhaber-Gordon, David. Spatially resolved study of backscattering in the quantum spin hall state. *Phys. Rev. X*, 3:021003, Apr 2013. URL: http://link.aps.org/doi/10.1103/PhysRevX.3.021003, doi:10.1103/PhysRevX.3.021003.

[27] Oostinga, Jeroen B. and Maier, Luis and Schüffelgen, Peter and Knott, Daniel and Ames, Christopher and Brüne, Christoph and Tkachov, Grigory and Buhmann, Hartmut and Molenkamp, Laurens W. Josephson Supercurrent through the Topological Surface States of Strained Bulk HgTe. *Phys. Rev. X*, 3:021007, May 2013. URL: http://link.aps.org/doi/10.1103/PhysRevX.3.021007, doi:10.1103/PhysRevX.3.021007.

[28] Shuvaev, A. and Pimenov, A. and Astakhov, G. V. and Mühlbauer, M. and Brüne, C. and Buhmann, H. and Molenkamp, L. W. Room temperature electrically tunable terahertz Faraday effect. *Applied Physics Letters*, 102(24):241902, 2013. URL: http://scitation.aip.org/content/aip/journal/apl/102/24/10.1063/1.4811496, doi:{http://dx.doi.org/10.1063/1.4811496}.

[29] Katja C. Nowack, Eric M. Spanton, Matthias Baenninger, Markus König, John R. Kirtley, Beena Kalisky, Christopher Ames, Philipp Leubner, Christoph Brüne, Hartmut Buhmann, Laurens W. Molenkamp, David Goldhaber-Gordon, and Kathryn A.

Moler. Imaging currents in HgTe quantum wells in the quantum spin Hall regime. *Nature Mater.*, 12:787–791, 2013. doi:10.1038/nmat3682.

[30] C. Brüne, H. Buhmann, and L.W. Molenkamp. *Topological Insulators*, chapter 5, pages 125–143. Contemporary Concepts Of Condensed Matter Science. Elsevier, Amsterdam, 2013.

[31] M. Mühlbauer and A. Budewitz and B. Büttner and G. Tkachov and E.M. Hankiewicz and C. Brüne and H. Buhmann and L.W. Molenkamp. One-dimensional weak antilocalization and band Berry phases in HgTe wires. *acepted for publication in Physical Review Letters;* e-print arXiv:1306.2796, 2014.

[32] Sean Hart and Hechen Ren and Timo Wagner and Philipp Leubner and Mathias Mühlbauer and Christoph Brüne and Hartmut Buhmann and Laurens W. Molenkamp and Amir Yacoby. Induced Superconductivity in the Quantum Spin Hall Edge. *under consideration Nature Phys.;* e-print arXiv:1312.2559, 2014.

[33] Christoph Brüne, Cornelius Thienel, Michael Stuiber, Hartmut Buhmann, Elena G. Novik, Chao-Xing Liu, Ewelina M. Hankiewicz, and Laurens W. Molenkamp. Unperturbed Dirac spectrum from the surface states of gated strained bulk HgTe. in preparation for publication, 2014.

Danksagung

Zuerst möchte ich meiner Freundin Felicitas Gerhard, meinen Eltern Annemarie und Eckart Brüne, sowie meinen Geschwistern Alexander, Franziska und Elisabeth für die Unterstützung danken und dafür, dass sie mich während der Zeit der Doktorarbeit ausgehalten haben. Derselbe Dank gilt auch meinen Freunden und Verwandten, die genauso dazu beigetragen haben, dass ich diese Doktorarbeit abschließen konnte.

Besonderer Dank gebührt Hartmut Buhmann für die Annahme und die ausgezeichnete Betreuung dieser Dissertation, sowie für die vielen Diskussionen, Hilfestellungen und seine Unterstützung.

Genauso möchte ich Laurens Molenkamp für die Aufnahme am Lehrstuhl der EP3 danken so wie ebenfalls für die Diskussionen, Hilfe und Unterstützung.

Vielen Dank an alle Freunde und Kollegen der EP3 für die gute Zusammenarbeit, eure Hilfe und Unterstützung und die vielen Diskussionen, im Besonderen möchte ich mich bedanken bei:
Christopher Ames, Fabian Arnold, Alena Astakhova, Utz Bass, Martin Baußenwein, Tobias Bautze, Charles R. Becker, Kalle Bendias, Angelika Berger, Frank Biermann, Erwann Bocquillon, Tanja Borzenko, Johannes Brehm, Karl Brunner, Andreas Budewitz, Bastian Büttner, Matthias Däuber, Roland Ebert, Nina Eikenberg, Linus Elsäßer, Hanno Flentje, Alexander Friedel, Petra Fries, Anita Gebhardt, Felicitas Gerhard, Jean Geurts, Ragnar Gleim, Charles Gould, Manuel Grimm, Stefan Grauer, Mohammed Hamouda, Simon Hartinger, Michael Henke, Ines Hense, Jana Hinterberger, Volkmar Hock, Grzegorz Karczweski, Maximilian Kessel, Tobias Kießling, Johannes Knorr, Daniel Knott, Bruno Krefft, Thomas Khouri, Moritz Leberecht, Christoph Leicht, Philipp Leubner, Chaoxing Liu, Florian Lochner, Stefan Mark, David Mahler, Luis Maier, Mathias Mühlbauer, Marcel Mittermüller, André Müller, Johannes Mutterer, Jeroen Oostinga, Wolfgang Ossau, Viktor Pinneker, Rebekka Pfeuffer, Christian Praetorius, Christoph Pohl, Martin Reuß,

Robert Rommel, Andreas Roth, Farough Roustaie, Edudard Rupp, Benedikt Rupprecht, Michael Rüth, Rainer Schaller, Ralf Scheibner, Raimund Schlereth, Sebastian Schneider, Joachim Schneider, Alfred Schönteich, Steffen Schreyeck, Peter Schüffelgen, Claus Schumacher, Stefan Sendelbach, Tobias Spitz, Michael Stuiber, Nadja Tarakina, Cornelius Thienel, Holger Thierschmann, Mirko Trabel, Farida Veliev, Timo Wagner, Florian Wallaschkowski, Jonas Wiedenmann, Jörn Wilhelm, Petra Wolf-Müller, Jianguo Yang, Martin Zipf.

Besonders möchte ich auch alle Mitglieder der Quantentransport Gruppe und der MBE/Reinraum Kaffeerunde hervorheben und euch ganz besonders danken.

Dank gilt den Kollaborationspartnern der

- Mesoskopische Physik, Universität Würzburg Björn Trauzettel, Ewelina Hankiewicz, Grigory Tkachov
- Goldhaber-Gordon labs, Stanford University: David Goldhaber-Gordon, Markus König, Mathias Baenninger, Reyes Calvo,
- S.C. Zhang group, Stanford University: Shoucheng Zhang, Xiao-Liang Qi Joseph Maciejko T. L. Hughes
- Shen labs, Stanford University: Zhi-Xun Shen Yulin Shen Yue Ma
- Moler labs, Stanford University: Kathrin Moler, Katja Novack, Ilya Sochnikov
- Sinova group, Texas A&M University: Jairo Sinova
- Theoretische Physik 1, Universität Würzburg: Werner Hanke
- Yacoby labs, Harvard University: Amir Yacoby, Vivek Venkatachalam Sean Hart
- Solid State Spectroscopy, Technische Universität Wien: Andrei Pimenov, Dr. Alexey Shuvaev
- Département de Physique de la Matière Condensée, Université de Genève Dirk van der Marel, Jason Hancock, Alexey Kuzmenko, J. van Mechelen
- Quantentransportgruppe, Technische Universität Braunschweig: Georg Nachtwei, Fathi Gouider
- Terahertz Science and Technology Gruppe, Universität Regensburg: Sergey Ganichev,

Sergey Danilov, Helgi Diehl, B. Wittmann

- Laboratoire National des Champs Magnétiques Intenses, Grenoble Marek Potemski, Milan Orlita, C. Faugeras, K. Masztalerz,
- High Field Magnet Laboratory, Radboud University, Nijmegen Steffen Wiedmann, Ulrich Zeitler

für die gute Zusammenarbeit, den hervorragenden wissenschaftlichen Austausch und die fruchtbaren Diskussionen.